EXPERIMENTAL INVESTIGATION ON INCLUSIONS IN MEDIUM MANGANESE STEELS AND HIGH MANGANESE STEELS

EXPERIMENTAL INVESTIGATION ON INCLUSIONS IN MEDIUM MANGANESE STEELS AND HIGH MANGANESE STEELS

By

Michelia Alba, B.Sc., M.Sc.

A Thesis

Submitted to the School of Graduate Studies

In Partial Fulfilment of the Requirements

For the Degree

Doctor of Philosophy

McMaster University

DOCTOR OF PHILOSOPHY (2021)	McMaster University
(Materials Science and Engineering)	Hamilton, Ontario

TITLE:	Experimental Investigation on Inclusions in Medium Manganese Steels and High Manganese Steels
AUTHOR:	Michelia Alba, B.Sc., M.Sc. (Pohang University of Science and Technology, South Korea)
SUPERVISOR:	Dr. Neslihan Dogan
NUMBER OF PAGES:	xviii, 137

ABSTRACT

Advanced High Strength Steel (AHSS) has become a popular steel grade among automakers to produce vehicle bodies. With improvements in strength and elongation, AHSS has evolved to its 2nd generation, including high manganese steel. Even though it has outstanding strength, the 2nd generation of AHSS faces some production problems due to its high alloying elements. With continual improvement, the 3rd generation of AHSS is currently in production. In this generation, the steel types still have a competitive strength and elongation like the 2nd generation of AHSS while having lower alloying element contents and production costs. One of the types of 3rd generation AHSS is medium manganese steel. Research related to the 2nd and 3rd generation of AHSS mainly focuses on their mechanical properties and microstructures. As there is a strong correlation between mechanical properties and inclusion characteristics, further investigation of the evolution of inclusions is still required.

In this study, high-temperature experiments were conducted to investigate the effects of metal chemistry on the inclusion evolution in liquid steel. The concentrations of manganese, aluminum, and nitrogen were varied systematically. Two and three-dimensional analysis techniques were applied to study the number, composition, and size distribution of inclusions. Electrolysis extraction was used to identify the oxide, sulfide, and nitride inclusions, whereas an automated SEM with an ASPEX feature was used to detect a larger number of inclusions for better representation of the steel matrix.

This work has established inclusion classification rules to distinguish nitride inclusions from oxide inclusions. To the best of the authors' knowledge, this is the first discussion of this type of inclusion classification in the open literature. Based on the automated SEM (ASPEX Feature) analysis, the type of detected inclusions in medium and high manganese steels were $Al_2O_{3(pure)}$, Al_2O_3-MnS, $AlN_{(pure)}$, AlN-MnS, AlON, AlON-MnS, and MnS inclusions. As the manganese content in the steel increased from 2% to 20%, the total amount of inclusions, especially AlN-contained inclusions, was raised. This phenomenon occurred due to the increase in nitrogen solubility with increased manganese content in the steel. The thermodynamic calculation also predicted that AlN inclusions would form when the steel was cooled or during the solidification. Moreover, AlN and MnS inclusions were observed to co-precipitate together.

Similar to manganese, the increase in the aluminum content (Al = 0.5-6%) increased the total amount of inclusions in the steel, and the dominant inclusion type is AlN. AlN and Al_2O_3 inclusions can be heterogenous nucleation sites for MnS inclusions. Furthermore, Al_2O_3 inclusions also became heterogeneous nucleation sites for AlN inclusions.

The experimental set-up was further modified to investigate the effect of nitrogen on the formation of inclusions in the medium manganese steels. The nitrogen was introduced by purging or injecting N_2 gas into the steel system. Similar to the effect of manganese and aluminum, the increase in the nitrogen content also increased the total amount of inclusions. Once the nitrogen content in the steel exceeded the critical limit for the formation of AlN

inclusions, AlN inclusions can be stable in the liquid steel. Moreover, regardless of the nitrogen content in the steel, AlN-MnS inclusions were formed in the slow-cooled steels. In terms of morphology, AlN inclusions can be formed of plate-like, needle, angular, agglomerate, or irregular shapes.

Furthermore, a brief investigation on the addition of calcium and nitrogen to the medium manganese steels found that calcium led to the formation of other complex inclusions, such as CAx and CAS-Other inclusions. In the medium manganese steel composition in the present study, the number of CAS-Other inclusions was dominated by (Ca,Mn)S-Oxide inclusions after the addition of Ca. However, with time and after introducing N_2 gas into the steel, the number of (Ca,Mn)S-Nitride inclusions also increased. The formation of (Ca,Mn)S-Nitride inclusions resulted from the co-precipitation of CaS, MnS, and AlN.

The current work provides a better understanding of the formation mechanism of inclusions in medium manganese steels and high manganese steels. It presents complete information on the characteristics of inclusions, such as the number density, type, and morphology of inclusions. This knowledge can help steelmakers improve the steelmaking process to control the formation of inclusions, which can be problematic for the manufacture and performance of medium manganese steels and high manganese steels.

ACKNOWLEDGEMENTS

I wish to express my deepest gratitude to my supervisor, Dr. Neslihan Dogan, who gave meaningful guidance and wisdom throughout my Ph.D. program. Without her encouragement and both material and moral support, my Ph.D. journey will be extremely tough. I would like to extend my thanks to Dr. Ken Coley, who gave invaluable insight and discussion in every meeting. I am also grateful to Dr. Stanley Sun, who provided fruitful discussion and initiate access to automated SEM-ASPEX in ArcelorMittal Dofasco. The motivation and guidance from the three of them as my committee members allow me to improve myself and be a better me.

I appreciate many faculties, staff, and researchers' support in the Department of Materials Science and Engineering. I especially wish to thank Dr. Muhammad Nabeel for helping me throughout my research process. His assistance in laboratory work and valuable suggestions helped me reach the goal of this research. I also thank Li Sun, who gave me the training and assistant for inclusion analysis on automated SEM-ASPEX in ArcelorMittal Dofasco. I want to thank Xiaogang Li, Doug Culley, and Ed McCaffery to train the various laboratory equipment. I want to thank Mary-Anne, who always helped me regarding the academic administration during my Ph.D. period. I am also thankful to John Thompson for his pleasant conversations and the opportunity to participate in the preparation of several Steel Research Center meetings.

I would like to thank my friends in the McMaster Pyro Metallurgy Group for their support and help during the five years of my Ph.D. period. Thanks to Mukesh Sharma for the good lunchtime discussion, Aliyeh Rafiei for the memorable trips to many places, Keyan Miao for being there and sharing the struggle dealing with inclusion analysis, Kezhuan Gu for initiating group hikes, Jayasree Biswas for recommending to join the mindfulness session, Ameya Kadrolkar for enjoyable conversations every time we met, Yousef Tabatabaei for being a friendly assistant to use Mosaic when I arrived in Canada, Brian Jamieson for organizing the group meetings, and Wangzhong Mu for helping me in the lab during his stay. I am also thankful to my friend outside the group, Lynn Zhao, for the delicious food and interesting chats every lunchtime. I am also grateful to Joseph Utomo, who always listened to everything I want to talk about and console me every time I have a bad day.

Finally, I would like to extend my gratitude to my family, who continually supports and understands whatever I do throughout my life. I dedicated this thesis to my mom, who is always in my memory, and my dad, who I hope to be always healthy.

Table of Contents

List of Figures

Chapter 2

Chapter 3

Chapter 4

Chapter 5

Chapter 6

List of Tables

Chapter 2

Chapter 3

Chapter 4

Chapter 5

Chapter 6

List of Abbreviations and Symbols

AA	Acetylacetone
AHSS	Advance High Strength Steel
AR	Aspect ratio
BF	Blast Furnace
BOS	Basic Oxygen Steelmaking
CAS	Composition adjestment by Sealed Argon Process
CF	Circularity Factor
CLM	Cathodoluminescence Microscopy
CVN	Charpy V-Notch
DP	Dual-Phase
DRI	Direct Reduced Iron
EAF	Electric Arc Furnace
EDS or EDX	Energy Dispersive X-ray Spectroscopy
EE	Electrolysis Extraction
EMS	Electromagnetic Stirring
FLD	Forming Limit Diagram
HIC	Hydrogen-Induced Cracking
HSS	High Strength Steel
ICP-OES	Induction-coupled plasma optical emission spectrometry
LIP	Light-Induced Plasticity
LSHR	Liquid Sampling and Hot Rolling
M	Metal or deoxidizing agent
MART	Martensitic steel
MIDAS	Mannesmann inclusion detection by analyzing surfboards
MS	Methyl Salicylate
MQM	Modified Quasichemical Model

O	Oxygen
OES	Optical Emission Spectroscopy
PC	Polycarbonate
PDA	Pulse Discrimination ANalysis
PHS	Press-Hardened Steel
PR	Precipitation Ratio
PSD	Particle Size Distribution
Q&P	Quenching and Partitioning
RA	Reduction of Area (%)
RE	Rare Earth Element
RH	Rurhstahl-Heraeus
SEM	Scanning Electron Microscope
SFE	Stacking Fault Energy (mJ/m^2)
SSC	Sulfide Stress Cracking
TEA	Triethanolamine
TRIP	Transformation Induced Plasticity
TWIP	Twin Induced Plasticity
a	Raoultian activity
α_{bcc}	BCC – Martensite
a_n	The lattice parameter of the nucleated solid inclusion
a_s	The lattice parameter of the substrate
A_{sur}	The surface area of the metal
c_j	Concentration of species
ΔG°	Gibbs free energy change (J/mol)
ΔG^*_{Het}	Critical nucleation barrier energy for heterogeneous nucleation
ΔG^*_{Hom}	Critical nucleation barrier energy for homogeneous nucleation
ΔG_V	A thermodynamic driving force for crystallization

$\delta_{(hkl)_n}^{(hkl)_s}$	Lattice disregistry between the substrate and nucleated solid
d	Interatomic spacing
D_{ave}	Average diameter of inclusion (μm)
D_{dis}	Average dissolved depth
D_{max}	Maximum diameter of inclusions (μm)
ε_{hcp}	HCP – Martensite
e^j	First order interaction parameter of species
f	Activity coefficient of species
γ_{fcc}	FCC – Austenite
γ_{LS}	Interfacial energy of the solid-liquid phase
γ_{nL}	Surface energy between the liquid and the nucleant
γ_{nS}	Surface energy between the solid and the nucleant
g_s	Solid fraction
h	Henrian activity of species
$(hkl)_n$	Low-index plane of the nucleated solid
$(hkl)_s$	Low-index plane of the substrate
i	Overlap plane between the substrate and the nucleated solid
k	Partition ratio of solute species
K	Reaction equilibrium constant
N_A	Total number of inclusions per unit area (mm^{-2})
p	Partial pressure of the gas (atm)
ρ	Density of species or inclusions ($kg \cdot m^{-3}$)
ρ_{me}	The density of the dissolved metal
r^j	Second-order interaction parameter of species
T	Temperature of the solidifying front (K)
T_{AlN}	Formation temperature of AlN (K)
T_{liq}	Liquidus temperature (K)

T_{m}	Melting point of pure iron (=1811 K)
T_{MnS}	Formation temperature of MnS (K)
T_{sol}	Solidus temperature (K)
T_{steel}	Temperature of the steel (K)
θ	Wetting angle of the nucleating solid phase on the heterogeneous nucleation
$[uvw]_n$	Low-index direction in $(hkl)_n$
$[uvw]_s$	Low-index direction in $(hkl)_s$
$[x]$	Species in metal
(x)	Species in slag
$\{x\}$	Species in gas form
$[\%x]$	The concentration of species, in mass percent
$[\%x]_0$	Initial concentration of solute species in liquid steel, in mass percent
X	Lattice distance of inclusion
ω	Angle between $[uvw]_s$ and $[uvw]_n$
W_{dis}	Weight of the dissolved metal

Chapter 1

Introduction

1.1 Research Background

Over the last couple of decades, commercial and scientific interest in the new generation of advanced high-strength steel (AHSS) has increased due to their outstanding mechanical properties. The combination of lightweight and ultra-high-strength makes the high and medium manganese steels superior, and they have become popular among the new generation of AHSS for automotive applications.

For the direct application of both medium manganese steel and high manganese steel grades, most of the research primarily studied their mechanical properties. For instance, researchers reported that cracking usually happens during the continuous casting process of high manganese steels due to poor hot ductility.[1–4] One of the reasons is the formation of inclusions (e.g., AlN) pinning the grain boundary. When combined with the segregation of the alloying elements (e.g., sulfur), inclusions will lead to the embrittlement of the steel.[1,5] Furthermore, it was also reported that AlN inclusions played a role in reducing the toughness of high manganese steel.[6,7] AlN inclusions can reduce the Charpy V-Notch breaking Energy (CVN) in high manganese steel. These inclusions become the site for void nucleation, leading to steel fracture due to microvoid coalescence.[6] Even though the non-metallic inclusions influence the mechanical properties,[8] machinability,[9] and castability[10] of the steel, there are limited laboratory studies[8–10] that focus on the characteristics of inclusions in the medium manganese steel and high manganese steel grades.

The alloying elements have relatively high concentrations in medium manganese steels and high manganese steel grades compared to those in regular carbon steel grades. Therefore, these high concentrations have an impact on the formation of inclusions. For instance, the manganese content can go up to 10% and 30% in the medium manganese steels and high manganese steels, respectively.[11–14] While manganese reacts with sulfur and forms sulfide inclusions, it also increases the solubility of nitrogen in the steel, thereby promoting the formation of nitride inclusions.[15] As the formation of oxides, sulfides, and nitrides cannot be avoided, the inclusions are expected to be more complex during the production of medium manganese steels and high manganese steels. Thus, a thorough understanding of the effects of alloying elements on the formation mechanism of inclusions in medium manganese steel and high manganese steel is needed. Since the performance of these steel grades can be improved by understanding the non-metallic inclusion formation mechanisms and further controlling these inclusions during refining processes, this study aims to fill the gap in this area of knowledge.

1.2 The Objective of This Study

This study aims to develop a fundamental understanding of the evolution of inclusions during the refining of medium manganese steels and high manganese steels. The specific objectives of this study are as follows:

1. Establish proper and systematic inclusion analysis tools to characterize the complex composition and morphology of the inclusions.
2. Assess the phase stability of inclusions through thermodynamic modeling.
3. Obtain experimental data for the composition, size distribution, and morphology of inclusions as a function of manganese, aluminum, and nitrogen contents of the steel.
4. Propose formation mechanisms for different types of inclusions observed in high and medium manganese steels.
5. Investigate the effect of calcium addition on co-precipitation of inclusions in medium manganese steels.

The questions this work will answer are crucial for controlling steel cleanliness during medium manganese steel and high manganese steel production.

1.3 Thesis Outline

Chapter 1 provides a general introduction of the research, explains the research objectives, and presents the outline of the thesis. Chapter 2 reviews the secondary steelmaking process, the development of Advanced High Strength Steels (AHSS), mainly focusing on high manganese steel and medium manganese steel grades, the correlation between the mechanical properties and the non-metallic inclusions, the type of inclusions in high and medium manganese steels, thermodynamic of inclusion formation, the modification methods of inclusions and inclusion characterization techniques.

Chapter 3 is titled "Investigation of Inclusion Formation in Light-Weight Fe–Mn–Al Steels using Automated Scanning Electron Microscope Equipped with Energy-Dispersive X-Ray Spectroscopy." This chapter provides the details of the systematic technique for characterization of inclusions in the Fe-Mn-Al steels with medium manganese content and high manganese content. It also describes the types of inclusions in Fe-Mn-Al steels and the effects of manganese contents on the formation of inclusions by incorporating thermodynamic calculations and information on the morphology of observed inclusions. This chapter is published in Steel Research International (DOI: 10.1002/srin.201900477).

Chapter 4 provides the characteristics of inclusions in the Fe–5Mn–xAl medium manganese steels. The Al content is varied from 0.5 to 6%. It explains the formation of AlN inclusions and suggests the use of a precipitation ratio to assess the preference of MnS and Al_2O_3 inclusions to co-precipitate together with AlN inclusions. This chapter is published in Ironmaking and Steelmaking (DOI: 10.1080/03019233.2020.1791549).

Chapter 5 reports the effect of nitrogen content on the formation of inclusions in Fe–5Mn–3Al steels. In the investigated steels, the N content is varied between 2 and 54 ppm. To reach the targeted N content, two different methods are applied. This chapter explains that N content can influence the total amount of inclusions and the dominant type of inclusions in the steels. Moreover, the morphology of AlN inclusions is classified into several classes to study the effect of N content on the shape of AlN inclusions. This chapter is published in Crystals (DOI: 10.3390/cryst10090836).

Chapter 6 aims at the effect of the addition of calcium on the formation of inclusions in the Fe–5Mn–3Al steel. It mainly focuses on the co-precipitation of inclusions, especially the AlN-containing inclusions with respect to calcium and nitrogen contents of the steel. The variation in the size and the type of inclusions are described.

Chapter 7 summarizes the key findings of each chapter. The conclusions provide a general understanding of the contribution of each work and propose future work.

Chapter 2

Literature Review

2.1 Secondary Steelmaking

Steel can be produced via two routes, namely, the Blast Furnace (BF)-Basic Oxygen Steelmaking (BOS) converter and the Electric Arc Furnace (EAF) routes, as schematically shown in Figure 2.1.[16] In the blast furnace, the iron ore is reduced to pig iron, with approximately 4.2% carbon content. The pig iron's carbon content is decreased by injecting oxygen into the metal bath in Basic Oxygen Steelmaking (BOS) converter. This process is called the integrated steelmaking process. Alternatively, in the EAF route, scrap metal is the charging material. Some operations can use 100% scrap metal or mix it with direct reduced iron (DRI). In the EAF, the electrodes are used to provide energy for heating and melting the scrap. The primary refining process of the hot metal is also performed by injecting oxygen, charging additional carbon, and charging lime or dolomite.[17] In both routes, when the target composition of the hot metal is achieved, the hot metal is tapped and transferred into a ladle furnace for further refining. The refining of steel in a ladle metallurgy station is called Secondary Steelmaking or Secondary Steel Refining. In the ladle furnace, some treatments are conducted on the hot metal, such as temperature control, alloy trimming, deoxidation, desulfurization, inclusion modification, and vacuum treatment, which will be explained in the next sections.

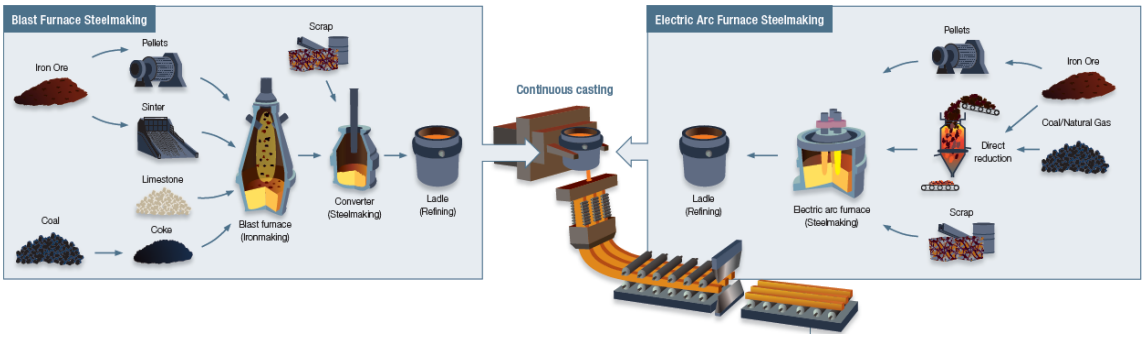

Figure 2. 1 Typical routes of liquid steel processing.[18] – (Reprinted with permission)

2.1.1 Deoxidation

After removing impurities such as carbon, silicon, and manganese in the BOF by injecting oxygen into the metal bath, the oxygen content in the molten steel can range between 200 and 800 ppm.[19] The oxygen content of the steel should be lowered to cast the steel successfully. Typical oxygen content is less than 30 ppm, depending on the steel products and grades.[20] This oxygen-reducing process is known as deoxidation.[21] The most common deoxidizing agents are aluminum, silicon, and manganese, which are strong oxide-forming elements.[20] The deoxidizing agent (M) reacts with oxygen and forms M_xO_y

as the deoxidation product. This reaction and its equilibrium constant (K_M) are shown below in Equation (2.1) and (2.2).[22]

$$x[M] + y[O] = M_xO_y \quad (2.1)$$

$$K_M = \frac{\left(a_{M_xO_y}\right)}{(h_M)^x(h_O)^y} \quad (2.2)$$

where h_M and h_O are the Henrian activity of the deoxidizing agent (M) and O, respectively. $a_{M_xO_y}$ is the activity of the deoxidation product. This deoxidation product is a stable phase at steelmaking temperatures and remains as a solid phase in the steel melt. The solid product is named "inclusion." The presence of oxide inclusions can be detrimental to the steelmaking processes as well as steel products. Thus, it needs to be removed from the steel or modified. The removal of inclusions can be done by absorption to the slag layer. In terms of inclusion modification, it will be further discussed in Section 2.8.

2.1.2 Desulfurization

Another crucial impurity to be controlled in the steel is sulfur. While some steel types require sulfur content, such as free-cutting steels or tool steels, sulfur can cause hot brittleness or hot shortness in many steel types, particularly in pipeline steel or armor steel.[19,21,22] Usually, for line pipe and hydrogen-induced cracking (HIC), the sulfur content needs to be as low as 10 ppm.[22] Before the desulfurization process in secondary steelmaking, the sulfur content in the hot metal is around 300 to 500 ppm.[19] This sulfur content is reduced in the ladle furnace during secondary steelmaking. After the steel is killed, the desulfurization is performed using a basic slag composition containing CaO. In this process, the metal-slag reaction can be promoted by stirring. Sulfur reacts with Ca in the slag and forms CaS.[19] The desulfurization reaction can be written as below in Equations (2.3) through (2.6).[19]

The dissolved $[S]$ turns to sulfide ion (S^{2-}), $[S] + 2e^- = (S^{2-})$ (2.3)

Oxygen ion in slag gives electrons to sulfur, $(O^{2-}) = [O] + 2e^-$ (2.4)

Equations 2.3 and 2.4 can be combined to represent the total reaction, i.e., elemental S reduces to S^{2-}, which then goes to the slag. In the slag, $O^{2-}$is replaced by S^{2-},

$$[S] + (O^{2-}) = [O] + (S^{2-}) \quad (2.5)$$

The net reaction of desulfurization is given as: $CaO + [S] = CaS + [O]$ (2.6)

2.1.3 Temperature Control

One of the purposes of the ladle furnace is conditioning the steel before it goes to the casting process.[23] In this case, the graphite electrode is used to control the steel's temperature in the ladle furnace.[23] The electrode is positioned in the slag layer, just above the molten

steel surface. Apart from the electrode, the molten steel is stirred to achieve a homogeneous temperature in the ladle.[24] There are several types of stirring mechanisms in the ladle furnace, such as gas bubble injection (argon gas injection through a submerged lance[25] and a porous plug from the bottom of the ladle[26]) and electromagnetic stirring (EMS).[24] These types of stirring have their advantages and disadvantages. The steelmaker chooses the stirring type based on their capital or operational cost and its efficiency. Stirring with the injection of argon gas provides excellent slag-metal contact compared to EMS. However, stirring with the injection of argon gas sometimes provides extra turbulence on the steel surface, which can cause a ladle eye in the slag layer and oxidize the steel.[27] The other problem for stirring with the injection of argon gas is the localized wear of lining which leads to a shorter refractory life.[28]

2.1.4 Alloy Trimming

The addition of various elements is required to achieve the desired microstructure and improve the properties of the steel.[29] The common alloying elements and their influences on the properties of steel are listed in Table 2.1.[29] For instance, as mentioned before, the addition of Mn can increase the ultimate tensile strength of steel compared to dual-phase (DP) steel, which has Mn content < 0.5% and has ultimate tensile strength around 680-930 MPa.[30] On the other hand, the medium manganese steel with an Mn content of 6.15% has an ultimate tensile strength of around 1131 MPa.[31] Furthermore, in Hadfield steel, the addition of Mn can take part as an austenite stabilizer to delay the transformation from austenite to martensite. Mn also can form carbide of Mn_3C and $(Fe,Mn)_3C$ in Hadfield steel.[32] Generally, the alloying elements are added in the form of ferroalloys (e.g., ferrosilicon).[25] The techniques for alloy addition are throwing bags filled with alloys, throwing alloys with a shovel, using mechanized chutes, bullet shooting, wire feeding, powder injection, or dipping alloy ingots in the agitated bath.

Table 2. 1. The typical alloying elements and their influences on steel[29]

Alloying Element	Influence on properties	Influence on microstructures
Si	Ferrite hardening	Ferrite forming and substitutional atom
Mn	Increases hardenability, strength, toughness, hot workability	Austenite forming, substitutional atom, carbide stabilizer
Ni	Increases strength, toughness, impact, and corrosion resistance	Austenite forming and substitutional atom
Cr	Increases hardenability, strength, corrosion resistivity	Ferrite forming, substitutional atom, forms carbides
Mo, W, Ti, Nb, V, Cr	Increase hardness, strength, wear resistance	Carbide forming
Ti, V, Al, Nb, Ta, B	Increase ductility and strength	Grain refinement and nitride forming

2.1.5 Inclusion Modification

Oxide and sulfide inclusions are formed during the secondary steelmaking process, and they are mostly detrimental to steel performance and the casting process.[33,34] Consequently, these inclusions should be controlled. The first method is removing the inclusions from the steel to the slag.[35] The inclusions attach to the surface of the gas bubbles and float to the steel-slag interface. Then, they are absorbed and dissolved in the slag.[36] In addition, inclusions can agglomerate and float to the steel surface since their density is less than the density of steel ($\rho_{Al_2O_3} = 3.97 \times 10^3\ kg \cdot m^{-3}; \rho_{Fe} = 7.86 \times 10^3\ kg \cdot m^{-3}$).[37] The second method is modifying the composition and morphology of inclusions to become less harmful.[22] One of the modification techniques is the addition of calcium into molten steel. For instance, alumina inclusion can be transformed to a range of calcium aluminates depending on Ca, O, and Al contents in the steel. Equation (2.7) shows the range of calcium aluminate inclusions when transforming from Al_2O_3 to $3CaO{\cdot}Al_2O_3$ (C_3A).[25] The CaO-Al_2O_3 phase diagram in Figure 2.2 shows the phase stability of the different calcium aluminate phases. At steelmaking temperature, $CaO{\cdot}Al_2O_3$ (CA), $12CaO{\cdot}7Al_2O_3$ ($C_{12}A_7$) and $3CaO{\cdot}Al_2O_3$ (C_3A) are formed as liquid inclusions since their formation temperatures are lower than 1873 K.

$$Al_2O_3 \rightarrow CaO{\cdot}6Al_2O_3\ (CA_6) \rightarrow CaO{\cdot}2Al_2O_3\ (CA_2) \rightarrow CaO{\cdot}Al_2O_3\ (CA) \rightarrow 12CaO{\cdot}7Al_2O_3\ (C_{12}A_7) \rightarrow 3CaO{\cdot}Al_2O_3\ (C_3A) \quad (2.7)$$

Steelmakers tend to produce these liquid calcium aluminate inclusions, as they are easier to remove from steel and minimize nozzle clogging problems.[25] Besides the modification of oxide inclusions, Ca treatment is also used to modify the morphology of sulfide inclusions, such as MnS. MnS inclusions usually deform to elongated shapes during the rolling process. By the addition of Ca, S in steel forms circular CaS inclusions or CaS-MnS inclusions.

Calcium can evaporate at steelmaking temperature due to its low boiling temperature (~1500°C).[21] Therefore, Ca is typically added in the form of cored-wire. Usually, the Ca-Si-contained cored-wire is injected into the steel bath (~2 m below the steel surface).[21] This way of addition improves the yield of Ca and efficiency of inclusion modification and reduces the production cost.[21] The modification of inclusions in the steel is not limited to calcium treatment; other elements can be used, such as rare earth (RE), Te, Se, or Mg. A detailed discussion of the modification of inclusions is given in Section 2.8.

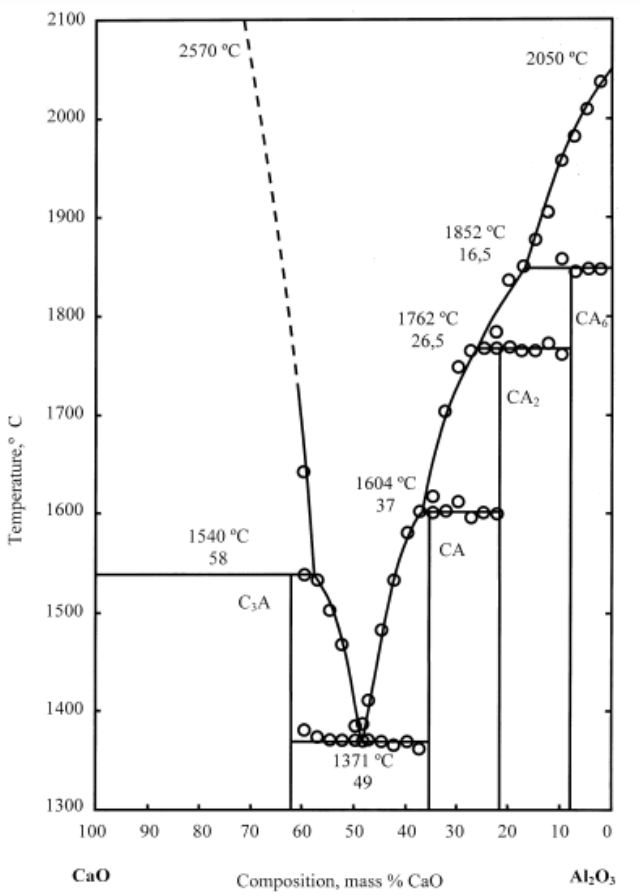

Figure 2. 2 $CaO\text{-}Al_2O_3$ phase diagram.[38] – (Reprinted with permission)

2.1.6 Vacuum Treatment

Vacuum treatment is used to achieve low concentrations of C, O, N, S, or H. Vacuum treatment can be done in the Rurhstahl-Heraeus (RH), which uses a recirculating system, or vacuum tank degasser, which use the non-recirculating system.[21,39] The schematic of both degassers is shown in Figure 2.3.[39,40] The removal of those harmful elements is achieved by using argon gas, which is circulated in RH or purged in a vacuum tank degasser when the system's pressure is reduced to approximately 0.001 atm.[39] In the recirculating system, the argon gas is used as lifting gas to lower the apparent density of the liquid steel, which can then be lifted up from the ladle to the vacuum vessel.[39] However, in the non-recirculating system, argon gas is used as stirring gas to homogenize the liquid steel and remove H and N.[39] In an RH degasser, the dissolved oxygen content in the steel is reduced by a carbon deoxidation reaction. The dissolved oxygen bonds with the dissolved carbon to form CO gas. This reaction is also called a self-decarburization process.[39] After the treatment in the RH degasser, the oxygen content can be controlled to less than 12 ppm.[41] In the case of carbon content, it can be reduced to around 10 ppm.[39] Besides lowering the

O and C content, the RH degasser can also reduce H (to be less than 2 ppm which is applied for H-controlled steels)[39] and N (to be less than 40 ppm).[42] In the case of a vacuum tank degasser, there are several types of tank, with arc reheating (Vacuum Arc Degasser) or without arc reheating (Vacuum Tank Degasser with induction coil stirring (Figure 2.3 (b) or with porous plug argon bubbling (Figure 2.3 (c)).[39] Both an RH and a vacuum tank degasser have similar removal achievements. Nowadays, RH and vacuum tank degassers are capable of removing C content < 20 ppm in 15 minutes of decarburization time.[43] In addition, a vacuum tank degasser can reduce sulfur (to be less than 10 ppm) by reacting with the top slag.[42,44]

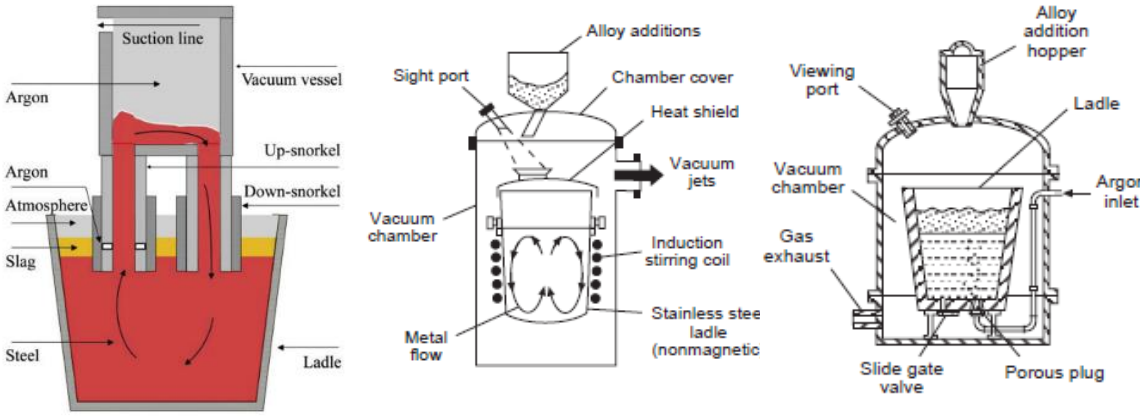

(a) (b) (c)

Figure 2. 3 The schematic of (a) RH degasser,[40] (b) vacuum tank degasser with induction coil stirring, and (c) vacuum tank degasser with porous plug for argon bubbling.[21] – (Reprinted with permission from Ref. 21 and Ref. 40)

2.2 Development of Advanced High Strength Steels (AHSS)

Advanced High Strength Steels (AHSS) are popular among automakers. The particular composition of these steel grades promotes a unique microstructure and improves the metallurgical properties.[45] The development of these grades started with the mild steels, which have a tensile strength below 280 MPa, and Conventional High Strength Steels (HSS), which have a tensile strength between 300 and 800 MPa (shown in Figure 2.4)[46]. The increased demands of lightweight and high strength steel grades resulted in the 1st Generation AHSS. This generation includes Dual-Phase (DP), Transformation Induced Plasticity (TRIP), martensitic (MART) steel, and Press-Hardened Steel (PHS). DP steel is used for outer body panels in automobiles, the body-in-white parts use TRIP steel, and martensitic steel is applied for some critical parts that need very high strength for safety.[47,48]

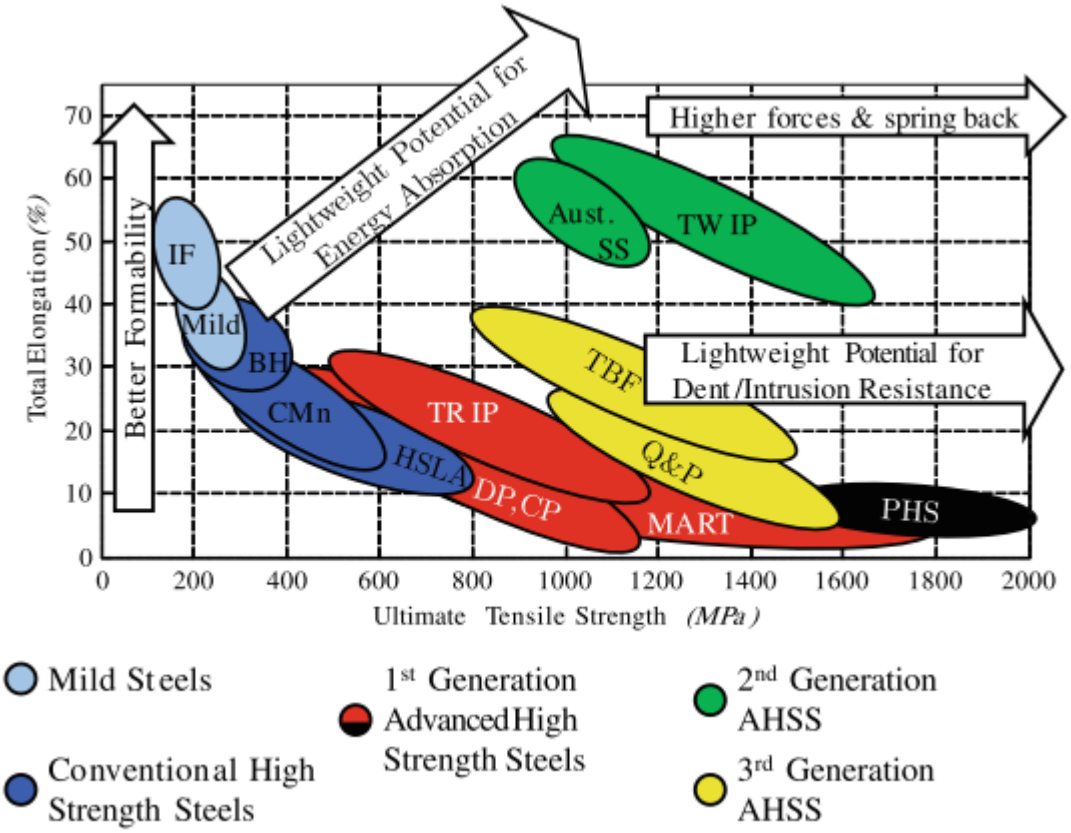

Figure 2. 4 Generation of Advanced High Strength Steels (AHSS).[46] – (Reprinted with permission)

With improvements, the 2nd Generation AHSS is expected to be lighter in weight than the 1st Generation AHSS, while having higher strength up to 1300-1500 MPa. This weight savings can lead to a 30-40% weight reduction in an automobile.[49] This improvement increased the usage of AHSS in manufacturing complex automobile parts while decreasing the weld joints. The 2nd generation of AHSS includes Twin Induced Plasticity (TWIP), Light-Induced Plasticity (LIP), austenitic stainless steels,[50] and austenitic high manganese steels.[51] The elongation and tensile strength of high manganese steel and carbon steel are compared in Figure 2.5.[52] The shaded area highlights the composition of high manganese steels, which have been studied for mechanical properties.[52,53] The high manganese steels (Mn 10 to 30%) have higher tensile strength and elongation than carbon steel. The high manganese steels usually contain a high content of other alloying elements such as Al and Si. All the alloying elements in the austenitic high manganese steel can control the properties of steel.[54] Si and Al take part in the solution strengthening, C stabilizes austenite to make higher uniform elongation, and Mn provides the austenite structure.[54] The high manganese steels are still being developed and studied.[54,55]

There are some difficulties in producing and welding the 2nd Generation AHSS, such as delayed fracture, poor hot ductility, and casting issues. These difficulties are particularly true for high manganese steels, which contain a generous amount of alloying elements, making the product costly.[11,56] So, the 3rd Generation AHSS has been developed to overcome these problems and fill in the gap between 1st and 2nd Generation AHSS (yellow area in Figure 2.4). The candidates of this generation are Quenching and Partitioning (Q&P) steel, Ferro-Austenitic steels, TRIP assisted DP steel, higher carbon TRIP steel,[48] and medium manganese steels.[51] Q&P steel grade has a higher ductility and similar strength compared to DP grade, whereas it has similar ductility and higher strength compared to TRIP grade. In the case of medium manganese steel, Mn content varies from 3 to 10% wt. This grade still has relatively high tensile strength and excellent mechanical properties with lower manganese content. Therefore, this steel grade is economical.[11]

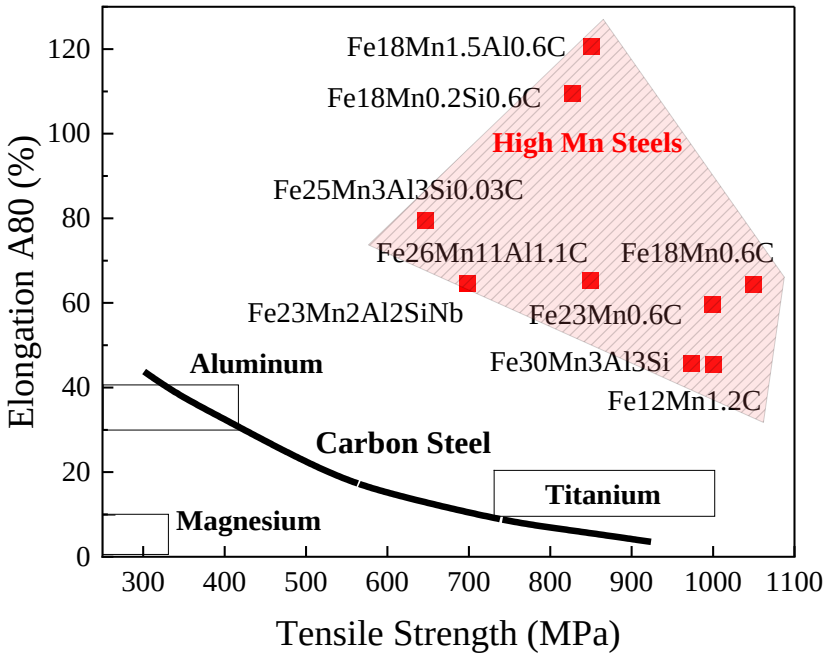

Figure 2. 5 Types of materials used in producing car bodies.[52,53] – (Reprinted with permission)

2.3 Mechanical Properties of High Mn Steels and Medium Mn Steels

Most of the research on the high manganese steel and medium manganese steel grades focused on their mechanical properties.[50,55,57–64] Grässel et al.[55] reported that the tensile strength of TWIP steels decreased from 930 (± 160) to 630 (±100) MPa and the total elongation increased from 43 (± 4) to 80 (± 10)% as manganese content increased from 15 to 30%. It is important to note that its strength is still higher than that of the regular carbon

steel grades. Therefore, TWIP steel is a better choice for the body parts of vehicles. Grässel et al.[55] also claimed that steels containing 3% Al, 3% Si, and 15-30% Mn achieved the highest total elongation. Meanwhile, Busch et al.[60] compared the formability of the sheet metal formed with DP 800 and DP 1000 (both of them have Mn content around 2%) and TWIP steel (Mn content around 15%). The results from the forming limit diagram (FLD) of the hemispherical dome test of those steels suggested that TWIP steel has the highest formability in comparison to DP 800 and DP 1000 steel grades. The major strain, φ, (when the minor strain vanishes) of TWIP steel is around 0.38, while DP 800 and DP 1000 are at 0.25 and 0.2, respectively. The high tensile strength and elongation of high manganese steels are mostly due to the formation of twins under mechanical load, i.e., TWIP effect, or multiple martensitic transformations from γ_{fcc}(austenite) → ε_{hcp}(hcp-martensite) → α_{bcc}(bcc-martensite), i.e., TRIP effect.[64] The phase transformation is related to stacking fault energy (SFE) in the austenitic matrix. When the SFE is low (≤ 20 mJ/m^2), the transformation is $\gamma_{fcc} \rightarrow \varepsilon_{hcp,}$ and when the SFE is high (> 20 mJ/m^2), the transformation of $\gamma_{fcc} \rightarrow \varepsilon_{hcp}$ is suppressed. The TWIP effect is promoted when the SFE is high. The addition of Si can suppress SFE, while Al can increase SFE.[64] Huang et al.[64] investigated the effect of adding Nb on the SFE of the high manganese steel (23% Mn). It was found that the addition of Nb will increase the SFE of steel. The increase of SFE promotes the TWIP effect, which can correlate to the increase of elongation of the steel.

Although their mechanical properties are excellent, steelmakers face some problems in producing high manganese steels. The formation of surface crack can happen during continuous casting, which is a severe hot ductility problem of the steel. This crack formation can be predicted by measuring the reduction of area (RA) in the tensile test.[65] In the continuous casting process, the RA value of steel should be more than 40% to avoid cracking.[2] However, some reports[2–4] claimed that high manganese steel could not reach this critical RA value. He et al.[3] reported that Fe18Mn0.75Al and Fe18Mn1.5Al steel grades have RA values lower than 23% at the temperature range between 700–1200°C. Moreover, Steenken et al.[2] reported that the RA value of the Fe17Mn3Al steel is approximately 20-40% at a temperature of 700–1100°C and above 1300°C. This problem is likely related to the high content of impurities (e.g., S or N content) and the inclusions (e.g., AlN or MnS), which will be discussed later in Section 2.4.

There are several studies on the mechanical properties of medium manganese steels.[12,31,66–68] Lee et al.[31] reported that the medium manganese steel (Fe–6.15Mn–1.4Si–0.04Al–0.05C) could achieve the tensile strength of 1131 MPa and total elongation of 58% when the austenite fraction is 50 vol%. Dong et al.[66] also reported that the ultimate tensile strength of medium manganese steel with 0.2% C and 5% Mn varied between 800 and 1500 MPa, and the total elongation was up to 45%. These ultimate tensile strengths in medium manganese steels are as high as the high manganese steels, although the content of alloying elements is lower compared to high manganese steels. Aydin et al.[12] found that the medium manganese steels with Mn content of 4-10% have a high value of SFE, which is around 26-31 mJ/m^2. This value leads to the formation of deformation twins, which improves the mechanical properties of the steel. The aforementioned results suggest that

medium manganese steel can compete with high manganese steel in terms of strength and elongation with fewer amounts of alloying elements.

2.4 Relationship between Inclusions and Mechanical Properties

Previous studies[1,4,69–76] showed that mechanical properties could be influenced by the size, morphology, and composition of inclusions in the steel. However, limited studies[1,4,77] investigated the relationship between mechanical properties and inclusions in the medium manganese steels and high manganese steels.

An inclusion can act as a stress raiser since the tensile strength is not maintained adequately within the inclusion.[78] It is reported that MnS stringers can decrease the transverse ductility (or reduction in area) of the steel.[70] However, they do not affect longitudinal ductility. Ånmark et al.[71] suggested that MnS inclusions could decrease the toughness and weldability of the steel. When they elongate during deformation, they give high anisotropy to the mechanical properties of the steel. However, MnS inclusions are known to improve the machinability of the steels. Tomita[72] observed the effect of morphology of MnS inclusions on the mechanical properties of 0.4C-Cr-Mo-Ni steels when heat-treated differently. It is reported that the stringy MnS inclusions can make brittle lamellar fractures along with the interface between the steel matrix and inclusions.[72] Moreover, the fine elliptical MnS in desulfurized steel influences the true strain at fracture, which depends on the tempering temperature of the steel grades. Ray et al.[79] stated that MnS stringers decrease the total elongation and impact energy of the transverse specimen.

Al_2O_3 inclusions do not improve the machinability of the steels due to their hard nature.[71,73] However, these inclusions give no anisotropy to the mechanical properties of the steels.[71] It is also found that Al_2O_3-CaO inclusions and the clusters of Al_2O_3 and Al_2O_3-MgO spinel are detrimental to the fatigue life of the steel because of their high hardness and low deformability.[74]

Funnell and Davies[75] reported that the carbon steels would possess poor hot ductility when they contain fine AlN inclusions with a size of less than 1 μm, as the reduction of the area is only around 32-35%. Funnell and Davies[75] also suggested that the increased number of AlN inclusions caused poor ductility of the austenitic steels when the Al content increased from 0.001% to 0.1%. Moreover, Kang et al.[1] suggested that the ductility of TWIP steels is weak when the sulfur content is between 0.01 and 0.023%. They detected long, coarse dendritic AlN rods at the dendrite and austenite grain boundaries, and these inclusions can lead to intergranular failure. The same types of inclusions were also observed by Wang et al.[4], who reported the effect of inclusions on the hot ductility of high manganese TWIP steels (16-17 wt% Mn and 0.002–2.10 wt% Al). They also observed that small AlN inclusions (with the average size < 1 μm) precipitated in austenite grain boundaries and lead to poor hot ductility of investigated high manganese TWIP steel. It was suggested that the fine and dispersed AlN particles can precipitate along austenite grain boundaries inhibiting the dynamic recrystallization; hence, resulting in intergranular failure and leading to poor hot ductility.

Besides the single-phase inclusions, a combination of inclusions can also occur in the steel due to the presence of different alloying elements. Lückl et al.[76] found that MnS and AlN can co-precipitate together in the low carbon steel due to the similarity in the crystal lattice between both inclusions. The poor hot ductility in the austenite region was reported due to the high number density of co-precipitation between MnS and AlN disrupting the rate of dislocation movement by dislocation pinning. Steenken et al.[2] also found that lowering the content of N from 75 to 48 ppm in high manganese steel can improve the ductility of the steel by increasing the RA value to 84%, which is far above the criteria of steel casting to prevent cracking and poor ductility, RA < 40%.

If the characteristics (such as composition, size, and morphology) of inclusions present in high and medium manganese steels are known, the way to control these inclusions can be identified in the secondary steelmaking process.

2.5 Type of Inclusions in High Mn Steels and Medium Mn Steels

In high manganese steels and medium manganese steels, the composition of inclusions can be more complex than a regular carbon steel grade due to the high amount of alloying elements, especially manganese and aluminum. Zhuang et al.[80] compared the types of inclusions present in laboratory-produced and industrial samples of Fe-25Mn-3Si-3Al TWIP steel, with nitrogen content around 20-26 ppm. The steel processing route of the manganese TWIP steel was by Argon Oxygen Decarburization (AOD) and Electro-Slag Remelting (ESR) processes.[80–82] They concluded that there were eight types of inclusions in TWIP steel, namely: single AlN, single Al_2O_3, single MnS(Se), AlN·MnS(Se), Al_2O_3·MnS(Se), MnO·Al_2O_3·SiO_2, Al_2O_3·CaO, and AlN·Al_2O_3·MnS(O,Se) inclusions. They found that AlN inclusions are the dominant type of inclusions as their number reaches around 50% in both the laboratory and industrial TWIP steels.

Gigacher et al.[83] studied the effect of manganese content on the composition and size distribution of inclusions under various solidification conditions. The metal chemistry was 15-25 wt% Mn, 0.05 wt% C, 3 wt% Al, 3 wt% Si, 75 ppm S, 75 ppm N, and 5 ppm O. A steel cylinder with zirconium-oxide coating was submerged in the liquid steel to accommodate heat transfer between the steel cylinder and the solidifying steel shell. This set-up allowed them to simulate the solidification conditions similar to the continuous casting. The reported inclusions were Al_2O_3·MnO with AlN and/or MnS, single AlN, single MnS, AlN and MnS, and Al_2O_3·MnO. Further, ThermoCalc was used to predict the inclusion precipitation in studied compositions, and a good agreement between predicted and detected inclusion phases was obtained.

Park et al.[84] studied the effects of Al content (1, 3, 6 wt%) and Mn content (10 and 20 wt%) on the inclusion formation in high Mn steel. The results showed that inclusions were classified into seven types, namely Al_2O_3, AlN or AlON, $MnAl_2O_4$, Mn(S,Se), agglomerate Al_2O_3-Al(O)N, oxide core with Mn(S,Se) wrap, and Mn(S,Se) core with the agglomeration of Al_2O_3-Al(O)N. AlN-contained complex inclusions were the most common type of inclusions. Mn(S,Se) compounds were formed due to the contamination of electrolytic manganese by Se. The morphologies of these inclusions are illustrated in Figure 2.6.[84] The

inclusions had mainly irregular shapes, and their size ranged between 0.5 and 10 μm. The inclusions observed by Park et al.[84] are similar to the type of inclusions observed by Zhuang et al.[80]

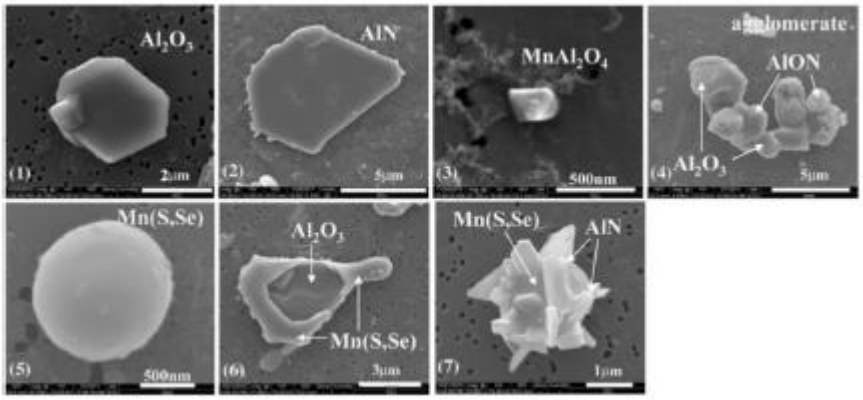

Figure 2. 6 Morphologies of inclusions in high Mn-Al alloyed steels.[84] – (Reprinted with permission)

Xin et al.[8] also investigated the effect of Al content on the evolution of non-metallic inclusions in high manganese TWIP steel. The aluminum and manganese contents were similar to Wang et al. [4], 0.002-2.1 wt% Al and 16-17 wt% Mn, with the nitrogen content around 43-76 ppm. With an increase in Al content, the dominant stable inclusions evolved from MnO → Al_2O_3/MnS → MnS → AlN, while the change of prominent oxide inclusion was MnO → Al_2O_3 → $MgAl_2O_4$ → MgO. On the other hand, the main sulfide inclusion evolution was from MnS to MgS.

There are limited studies on inclusions in medium manganese steels.[9,85] Kong et al.[85] investigated the inclusion evolution on medium manganese steel during the refining process and focused on the formation of spinel inclusion. The suggested route for the transformation of spinel inclusion was Al_2O_3 → $MgO·Al_2O_3$ → $(Mn,Mg)O·Al_2O_3$ → CaO–MgO–MnO–Al_2O_3. Yu and Liu[9] investigated the evolution of inclusions by using Mg treatment in medium manganese steels. In situ observation was conducted by using a confocal laser scanning microscope (CLSM). It was found that the inclusions evolved from $MnO·Al_2O_3$ to Al_2O_3 due to the higher deoxidation ability of Al as compared to that of Mn. After the Mg treatment, the inclusions were further transformed to $MgO·Al_2O_3$.

In summary, the previous studies reported not only oxide inclusions but also sulfide and nitride inclusions in medium manganese steels and high manganese steels. The formation of these inclusions in medium manganese steels and high manganese steels needs to be understood to properly control these inclusions. Thus, the explanation of the formation of each type of inclusion will be further described in the next section.

2.6 Thermodynamic of the Formation of Inclusions

Inclusions in the steel can be formed due to several reactions occurring in the steelmaking process. Inclusions can be classified as indigenous and exogenous inclusions; the indigenous inclusions are formed due to chemical reactions within the steel melt.[86] On the other hand, the exogenous inclusions are usually formed from external sources, such as erosion of lining refractory or slag entrainment.[20,86,87] As the infrastructure and monitoring of the steelmaking process have been improved over the years, the occurrence of the exogenous inclusions has decreased.[87] Alternatively, indigenous inclusions result from reactions during the steelmaking and casting process, and they are the subjects of this study and for discussion in the following sections.

2.6.1 Oxide Inclusion

Oxide inclusions are commonly found in steel due to reactions between alloying elements and dissolved oxygen in the liquid steel. The source of oxygen can be the oxygen injected in the primary steelmaking process or the oxygen from ferrous alloys and air. The dissolution of oxygen in the liquid steel follows the reaction in Equation (2.8) below.[22]

$$\frac{1}{2}\{O_2\} = [O] \tag{2.8}$$

The equilibrium constant (K_O) of the reaction above is listed in Equation (2.9) and (2.10).[22]

$$\log K_O = \frac{6120}{T_{steel}} + 0.15 \tag{2.9}$$

$$K_O = \frac{h_O}{{p_{O_2}}^{\frac{1}{2}}} \tag{2.10}$$

where T_{steel} is the temperature of the steel (K), h_O is the Henrian activity of the dissolved oxygen in the liquid steel and p_{O_2} is the partial pressure of oxygen (atm). Its relation to the activity coefficient, f_O, is given in Equation (2.11) and (2.12) below.[22]

$$h_O = f_O \times [\%O] \tag{2.11}$$

$$\log f_O = \sum_j e_O^j \cdot c_j + r_O^j \cdot c_j^2 \tag{2.12}$$

Since the dissolved oxygen in the steel can cause blowhole defects, becoming a problem in the casting process,[88,89] its content should be controlled. The deoxidation process is crucial in the secondary steelmaking process, as briefly explained in Section 2.1.1. There are some elements used as a deoxidizing agent, such as Mn, Si, and Al. Figure 2.7 compares the deoxidizing power of various alloying elements at 1873 K.[90] As seen in Figure 2.7, Al has the highest deoxidizing power compared to the other elements, such as Ti, V, Si, C, Mn, and Cr. Due to its highest affinity of oxygen, aluminum is commonly used as the primary

deoxidizer agent to produce Al-killed steel. The product of this deoxidation reaction is Al_2O_3 inclusions. Al_2O_3 inclusions are stable at steel processing temperatures. The formation of Al_2O_3 inclusion from the deoxidation process, its Gibbs free energy change,[91] and its equilibrium constant follow the reactions in Equation (2.13) to (2.15) below.[92]

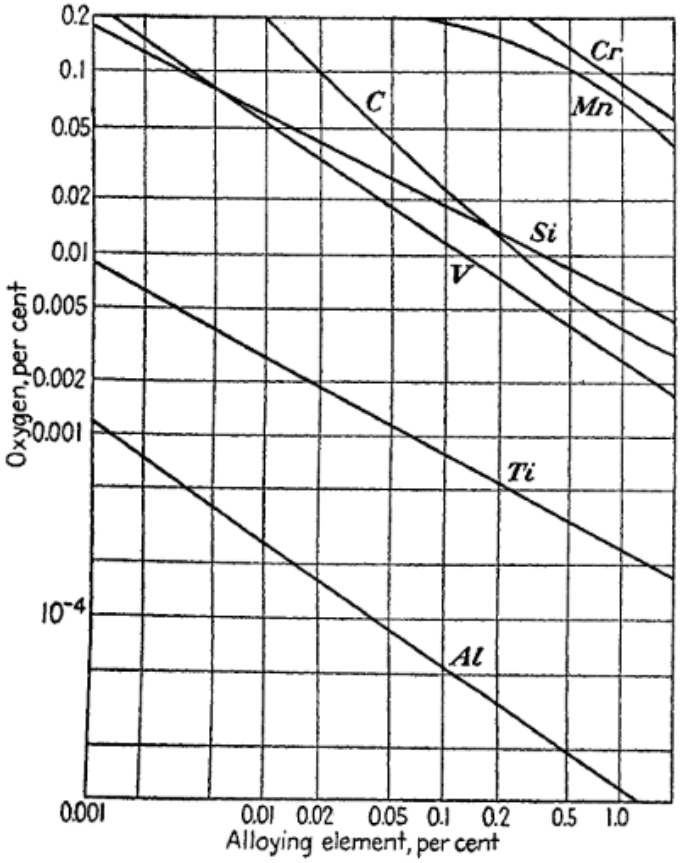

Figure 2. 7 Comparison of the deoxidizing power of alloying elements at 1873 K.[90] – (Reprinted with permission)

$$2[Al] + 3[O] = Al_2O_3 \quad (2.13)$$

$$\Delta G^{\circ}_{Al_2O_3} = -1225000 + 393.8T_{steel}\ J/mol^{[91]} \quad (2.14)$$

$$K_{Al_2O_3} = \frac{a_{Al_2O_3}}{h_{Al}^2 \cdot h_O^3} = \frac{a_{Al_2O_3}}{(f_{Al} \times [\%\mathrm{Al}])^2 \cdot (f_O \times [\%\mathrm{O}])^3} \quad (2.15)$$

where h_{Al} and h_O are the Henrian activity of Al and O, respectively. $a_{Al_2O_3}$ is the activity of Al_2O_3. f_{Al} and f_O are the activity coefficients of Al and O, respectively. To study the stability of Al_2O_3 inclusion in the liquid steel, Deng and Zhu[93] calculated the equilibrium lines for deoxidation of Al-killed pipeline steels (Fe-1.83Mn-0.037Al-0.14Si-0.04C) with basic slag. These equilibrium lines were then compared with the measured data from Yang

et al.[94] (Ref. 16 in the figure) as shown in Figure 2.8. The equilibrium lines (at $a_{Al_2O_3}$ = 1, Eq. (3)-(6) in Figure 2.8) are calculated using different equilibrium constants from several literatures.[91,93,95,96] It is shown that the activity of oxygen decreases with an increase of dissolved Al content. Moreover, the measured data agreed with the calculated equilibrium lines, although they have deviation due to the variance in the thermodynamic data. It implies that the assumption for the activity of Al_2O_3 being close to unity is valid. So, the equilibrium of Al-O in steel is affected by the activity of Al_2O_3 in the steel rather than in the slag. The area above the equilibrium lines is the area of deoxidation product saturated with Al_2O_3, and the area below the equilibrium lines is for Al dissolved in the steel melt.

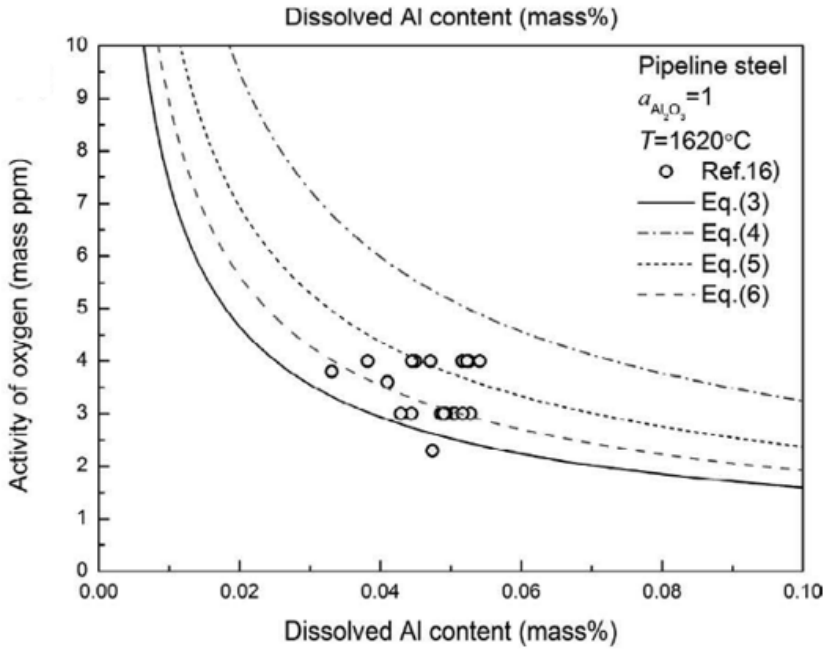

Figure 2. 8 The calculated deoxidation equilibrium lines of Al-killed pipeline steel at T=1620°C compared with the measured data.[93] – (Reprinted with permission)

Paek et al.[97] also constructed the inclusion stability diagram for the Fe-Mn-Al-O system, as seen in Figure 2.9. The Al deoxidation equilibria have been predicted by using the Modified Quasichemical Model (MQM) and validated against experimental data[84] on high Mn and high Al-alloyed steels. In Figure 2.9, Al_2O_3 covers most of the stability region (red lines area). It is suggested that the primary inclusion type would be Al_2O_3 as a deoxidation product in high Mn and high Al-alloyed steels except those with very high Mn content (Mn > 10%, blue and green lines area) and negligible Al content (Al < 0.0001%).

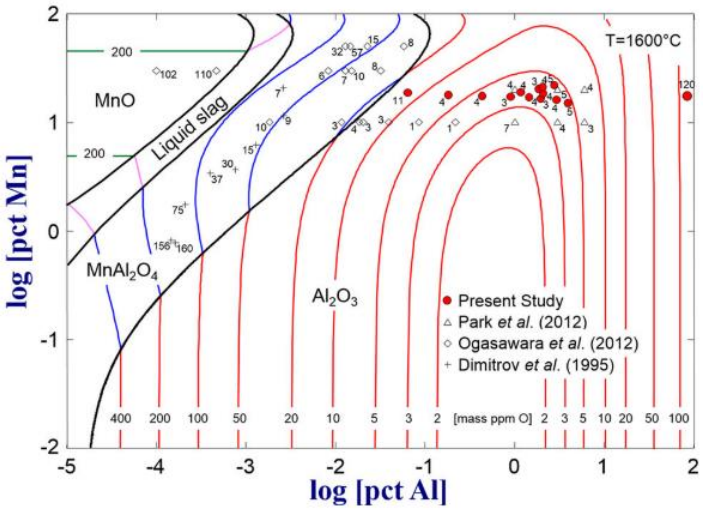

Figure 2. 9 Inclusion stability diagram of the Fe-Mn-Al-O system.[97] – (Reprinted with permission)

2.6.2 Nitride Inclusion

Besides oxide inclusions, nitride and sulfide inclusions are also formed in the secondary steelmaking process. The formation of nitride inclusions depends on the content of N in the steels. Nitrogen can have different roles in the steelmaking process, such as stabilizing the austenitic phase, causing shrinkage holes and pores during solidification, and forming nitride inclusions when reacting with other elements.[98] Since nitrogen can have both advantageous and disadvantageous impacts on steel performance, its content needs to be controlled. The dissolution of nitrogen in liquid metal is shown in Equation (2.16) below.[21,98]

$$\frac{1}{2}\{N_2\} \rightarrow [N] \tag{2.16}$$

The isothermal equilibrium constant (K_N)[25] and the Gibbs energy change[99] for this reaction are listed below in Equations (2.17) to (2.19).[21,98]

$$\log K_N = -\frac{255.6}{T_{steel}} - 1.26 \tag{2.17}$$

$$K_N = \frac{h_N}{P_{N_2}^{\frac{1}{2}}} \tag{2.18}$$

$$\Delta G_N^{\circ} = 3598 + 23.89 T_{steel}\, J/mol \tag{2.19}$$

where T_{steel} is the temperature (K), h_N is the Henrian activity of nitrogen, and P_{N_2} is nitrogen partial pressure (mbar). The activity of nitrogen, a_N, is proportional to the concentration of

nitrogen, [N] in wt% and its relation with the activity coefficient, f_N, is in Equation (2.20) and (2.21).[98]

$$h_N = f_N \times [\%\mathrm{N}] \tag{2.20}$$

$$\log f_N = \sum_{N}^{j} e_N^j \cdot c_j + r_N^j \cdot c_j^2 \tag{2.21}$$

where e_N^j and r_N^j are the first and second orders of Wagner's interaction parameter, respectively, and c_j is the concentration of another element in the steel. When the steel contains nitrogen, there is a possibility of forming nitride inclusions, such as AlN inclusion, commonly found in steel with high Mn and Al contents.[80,81,84] The reaction of the formation of AlN inclusion, its standard Gibbs free energy change,[100,101] and its equilibrium constant, K_{AlN},[102] are listed in Equations (2.22) to (2.24).

$$[Al] + [N] = AlN \tag{2.22}$$

$$\Delta G_{AlN}^{\circ} = -303500 + 134.6T_{steel}\, J/mol \tag{2.23}$$

$$\log K_{AlN} = \log \frac{a_{AlN}}{h_{Al} \cdot h_N} = \log \frac{1}{f_{Al} f_N [\%\mathrm{Al}][\%\mathrm{N}]} \tag{2.24}$$

where a_{AlN} is the activity of AlN and equals one. h_{Al} is Henrian activity of Al and f_{Al} is the activity coefficient of aluminum. Moreover, nitrogen solubility in the steel is influenced by alloying elements contained in the steel. The effect of different elements on the nitrogen solubility in the binary alloys (at 1600°C, P_{N_2} = 1 bar) is illustrated in Figure 2.10.[98] Some elements such as Mn, Ta, Mo, Cr, Nb, and V increase nitrogen solubility while S, O, Sn, Cu, Co, Ni, Si, and C decrease nitrogen solubility. The change in nitrogen content can be affected by the type and content of the alloying elements. However, the effect of Al is not clear in Figure 2.10.

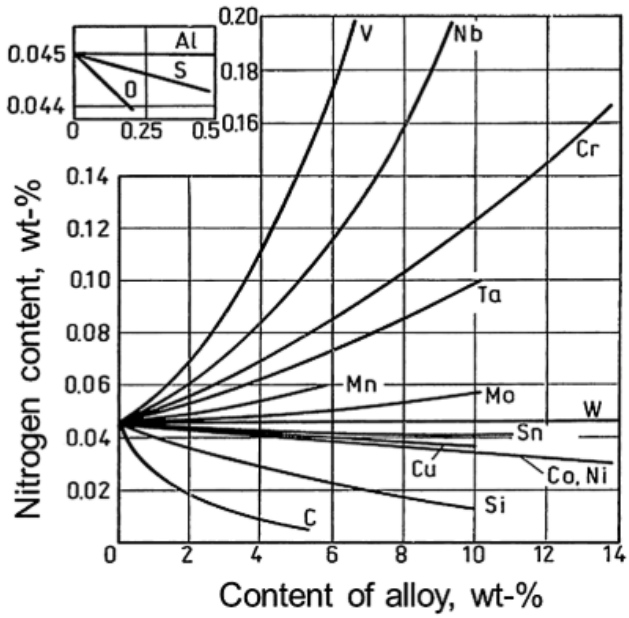

Figure 2. 10 Effect of different elements in the binary alloys on the solubility of nitrogen.[98] – (Reprinted with permission)

Paek et al.[102] investigated the relationship between aluminum content and nitrogen solubility in the formation of AlN in the Fe-Al-N melt with a partial pressure of nitrogen at 0.5 and 0.8 atm in 1873 K. The AlN stability diagram is illustrated in Figure 2.11.[102] As the dissolved aluminum content is increased, there is a negligible decrease in the dissolved nitrogen content in the Fe-Al-N melt (open symbols in Figure 2.11). Once the aluminum content reaches the critical value, the nitrogen content decreases and follows the AlN stability line due to the formation of AlN in Fe-Al-N melt (solid symbols in Figure 2.11).

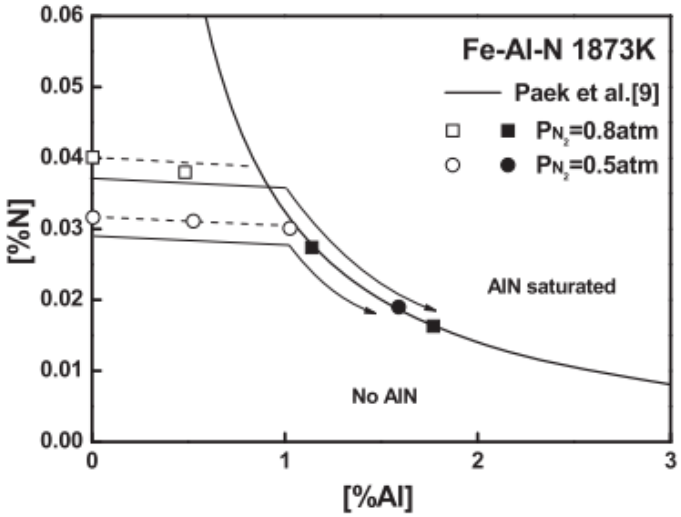

Figure 2. 11 AlN stability diagram in Fe-Al-N melts at 1873 K.[102] – (Reprinted with permission)

Besides the effect of aluminum, Paek et al.[102] also studied the impact of the Mn addition on the AlN formation in the Fe-Mn-Al-N melt at three different temperatures (1823, 1848, and 1873 K), as seen in Figure 2.12. It is shown that the solubility product of AlN, log[%Al][%N], increased linearly with an increase in the manganese content regardless of the temperature.

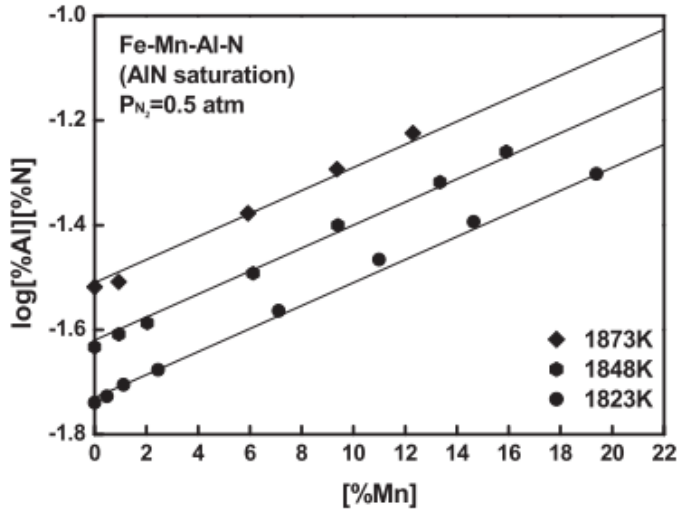

Figure 2. 12 Effect of Mn on the solubility product of AlN in Fe-Mn-Al-N melts.[102] – (Reprinted with permission)

Liu et al.[81] explained that AlN could form when the solidifying front is rich with solute Al and N during the solidification process. There is microsegregation in the steel when it is cooled. The solute atoms are rejected to the interdendritic region (non-equilibrium

solidification condition). As a consequence, there is an enrichment of Al and N in the final solidified area.[81] Then, AlN is thermodynamically precipitated when the product of [%Al]×[%N] in the liquid phase at the solidifying front exceeds the equilibrium value. The Al and N contents in the liquid phase during solidification can be calculated by the Scheil equation, and it is assumed that there is no diffusion in the solid phase. The content of Al[103] and N[102] at the solidifying front are calculated as in Equation (2.25) and (2.26).

$$[\%\mathrm{Al}] = [\%\mathrm{Al}]_0(1-\mathrm{g})^{(k_{Al}-1)} \quad (2.25)$$

$$[\%\mathrm{N}] = [\%\mathrm{N}]_0/[k_N + (1-k_N)(1-\mathrm{g})] \quad (2.26)$$

where $[\%\mathrm{Al}]_0$ and $[\%\mathrm{N}]_0$ are the initial concentrations of solute Al and N in liquid steel, respectively. [%Al] and [%N] are the concentrations of the solute Al and N in the liquid phase at the solidifying front, respectively. k_{Al} and k_N are the partition ratio of solute Al (= 0.6) and N (= 0.27) at equilibrium, respectively.[102] g_s is the solid fraction. The other way to calculate [%Al]×[%N] is by using Equation (2.27).[81]

$$K_{AlN} = [\%\mathrm{Al}] \times [\%\mathrm{N}] = 10^{\frac{-15850.92}{T_{steel}}+7.187} \quad (2.27)$$

Furthermore, the relationship between temperature and solid fraction can be calculated using Equation (2.28).[81]

$$T = T_\mathrm{m} - \frac{T_\mathrm{m} - T_\mathrm{liq}}{1 - \mathrm{g}_s \frac{T_\mathrm{liq} - T_\mathrm{sol}}{T_\mathrm{m} - T_\mathrm{sol}}} \quad (2.28)$$

where T is the temperature of the solidifying front, T_m is the melting point of pure iron (1811 K), T_liq is the liquidus temperature of the steel, and T_sol is the solidus temperature of the steel.

2.6.3 Sulfide Inclusion

The sulfur content in steel plays an important role. As sulfur is mostly not desirable in steel, its content is always kept as low as possible (except in the free-machining steels, high sulfur content, 0.08-0.35% S, is desired).[104] Sulfur is known to form sulfide inclusions, causing an anisotropy on the mechanical properties of the steel, pitting corrosion, and sulfide stress cracking (SSC), and embrittlement.[105,106] Generally, the addition of Mn to the steel reduces the formation of FeS inclusions, which have a low melting point and lead to hot-shortness in the steel.[70,107] As a consequence, MnS inclusions are formed in the steel. The higher melting point of the MnS inclusion increases its plasticity, and it is deformed in an elongated shape during the hot working.[70] This phenomenon leads to the cracking of the steel.[70] Moreover, similar to AlN inclusions, MnS inclusions can form during the solidification process. The standard Gibbs free energy change for the formation of MnS,[100,101] and its equilibrium constant[108] are listed in Equations (2.29) - (2.31).

$$[Mn] + [S] = MnS \quad (2.29)$$

$$\Delta G^{\circ}_{MnS} = -168822 + 98.87T_{steel}\, J/mol \quad (2.30)$$

$$\log K_{MnS} = \log \frac{a_{MnS}}{h_{Mn} \cdot h_S} = \log \frac{1}{f_{Mn} f_S [\%\mathrm{Mn}][\%\mathrm{S}]} \quad (2.31)$$

where a_{MnS} is the activity of MnS and it is unity with respect to 1 wt% standard state, h_{Mn} is the Henrian activity of Mn and f_{Mn} is the activity coefficient of Mn. From the equations above, the condition for the formation of pure MnS is provided in Equation (2.32), as seen below.[108]

$$f_{Mn} f_S [\%\mathrm{Mn}][\%\mathrm{S}] \geq K_{MnS} \quad (2.32)$$

Qi et al.[108] investigated the formation of MnS inclusions in austenitic hot-work die steel (Fe-15Mn-3Cr-Mo-V-0.002S) during the ESR and continuous unidirectional solidification (ESR-CDS) processes. The stability diagram of precipitation of MnS inclusions is provided in Figure 2.13.[108] It is shown that MnS inclusions do not precipitate in the liquid steel because the steel compositions (points A and B) are lower than their equilibrium value. Qi et al.[108] explained that these results do not consider the microsegregation in the solidification period. In the actual practice, the distribution of solute atoms is different in the non-equilibrium solidification condition.[108] The solute atoms are rejected to the interdendritic region when the solidification happens. It leads to the enrichment of Mn and S in the final solidified area in interdendritic arm spacing. So, when the product of [%Mn]×[%S] in the final solidified region exceeds the equilibrium solubility product for MnS inclusion precipitation, then MnS inclusion forms during solidification.[108]

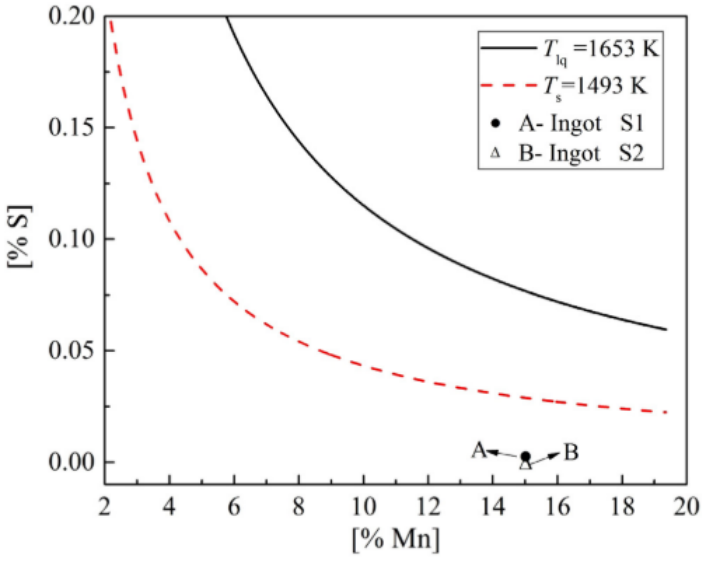

Figure 2. 13 Stability diagram of MnS inclusions precipitation in austenitic hot-work die steel.[108] – (Reprinted with permission)

2.7 The Co-precipitation of Inclusions

As the steel composition becomes more complex, sulfide, nitride, and oxide inclusions can co-precipitate together. The co-precipitation mechanism of complex inclusions usually depends on several factors: the formation temperature of inclusions and the lattice misfit (or sometimes called lattice disregistry) between inclusions. The formation of complex inclusions follows the thermodynamic stability of each inclusion, which is related to the formation temperature of the inclusions. If the steel system is under an equilibrium condition, the inclusions that are more stable in liquid steel will form first. Later, during the cooling process, these inclusions become the heterogeneous nucleation sites for other inclusions, which have a lower formation temperature.

Liu et al.[81,82] analyzed the formation, growth, and dissolution of AlN and MnS inclusions by incorporating kinetic and thermodynamic calculations in high manganese TWIP steel from AOD and ESR. In order to describe the formation of AlN and MnS inclusions, the stability diagram of AlN and MnS precipitation in the AOD and ESR process is shown in Figure 2.14. Points A and B represent the analyzed dissolved Al and Mn contents in the AOD samples, respectively. On the other hand, A' and B' represent the dissolved Al and Mn in ESR samples, respectively. They stated that AlN or Al(O)N inclusions were formed before MnS precipitation in the AOD process, as its formation temperature (Point A) is higher than T_{liq} of AOD ingot and MnS formation temperature (Point B) as seen in Figure 2.14. AlN acted as heterogeneous nuclei of MnS inclusion then formed more complex inclusions, such as MnS(Se)·Al(O)N clusters. In the ESR process, the content of nitrogen in the steel is low (6 ppm); thereby, the precipitation temperatures of AlN and MnS inclusions were also decreased. AlN inclusions could not be formed in liquid TWIP steel, as its formation temperature (Point A') is lower than the T_{liq} of ESR ingot, so the heterogeneous nuclei for MnS inclusions decreased. As a result, MnS(Se)·Al(O)N inclusions were rarely seen in steel after the ESR process.

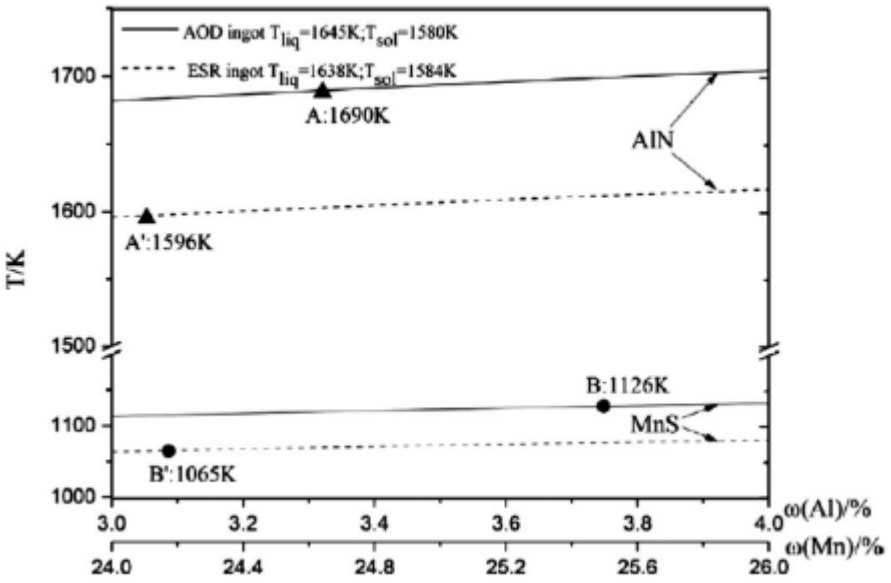

Figure 2. 14 Stability diagram of AlN and MnS precipitation in the AOD and ESR process.[82] – (Reprinted with permission)

The classical nucleation theory can explain one type of inclusion's ability to serve as the nucleation site for other inclusions. Penna et al.[109] stated that the classical nucleation theory predicts that low interfacial energy and a low lattice disregistry between the heterogeneous nucleus and the nucleating solids are supported by decreasing the activation barrier or the critical nucleation barrier. The critical nucleation barrier for heterogeneous nucleation, ΔG^*_{Het} can be formulated in Equation (2.33).[109]

$$\Delta G^*_{Het} = \frac{(2 + cos\theta)(1 - cos\theta)^2}{4} \cdot \Delta G^*_{Hom} \tag{2.33}$$

where θ is the wetting angle of the nucleating solid phase on the heterogeneous nucleation and ΔG^*_{Hom} is the critical nucleation barrier for homogeneous nucleation. Furthermore, ΔG^*_{Hom} can be calculated by Equation (2.34).[109]

$$\Delta G^*_{Hom} = \frac{16\pi\gamma^3_{LS}}{3\Delta G^2_V} \tag{2.34}$$

where γ_{LS} is the interfacial energy of the solid-liquid phase and ΔG_V is the thermodynamic driving force for crystallization. The interfacial energy balance for the heterogeneous nucleation is provided in Equation (2.35) and schematically illustrated in Figure 2.15.

$$\gamma_{nL} = \gamma_{nS} + \gamma_{LS} cos\theta \tag{2.35}$$

where γ_{nL} is the surface energy between the liquid and the nucleant and γ_{nS} is the surface energy between the solid and the nucleant.

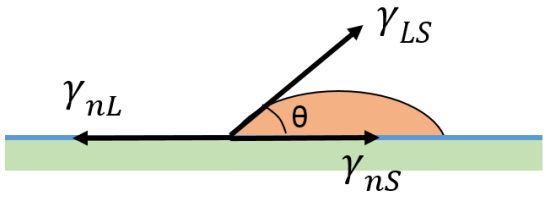

Figure 2. 15 The schematic of the wetting angle for the heterogeneous nucleation.[109] – (Reprinted with permission)

Figure 2.15 shows that the wetting angle, θ, is defined by the balance of the interfacial energy between nucleating solid, liquid phase, and substrate. The interfacial energy in a system depends on the following factors: the chemical nature of the substrate, topographic features of the substrate surface, the electrostatic potential between substrate and nucleated solid, and the lattice disregistry between two phases at the interface.[110] The latter factor is often used to explain the heterogeneous nucleation behavior since interfacial energy measurement is difficult in practice. According to Turnbull and Vonnegut,[111] a smaller disregistry between low-index planes of inclusion and metal phases indicates lower interfacial energy required for the transformation, making the nucleation of inclusion phases easier. The lattice disregistry between inclusions can be calculated by Bramfitt's planar disregistry model, as shown in Equation (2.36).[110]

$$\delta_{(hkl)_n}^{(hkl)_s} = \sum_{i=1}^{3} \frac{1}{3} \left[\frac{\left| \left(d_{[uvw]_s^i} cos\omega \right) - d_{[uvw]_n^i} \right|}{d_{[uvw]_n^i}} \right] \times 100\% \qquad (2.36)$$

where $(hkl)_s$ and $(hkl)_n$ are the low-index plane of the substrate and nucleated solid, respectively. $[uvw]_s$ and $[uvw]_n$ are the low-index direction in $(hkl)_s$ and $(hkl)_n$, respectively. d is the interatomic spacing, ω is the angle between $[uvw]_s$ and $[uvw]_n$, and i is the overlap plane between the substrate and the nucleated solid. When the disregistry between a particular inclusion and the precipitated phase is below 6%, the particular inclusion is effectively the heterogeneous nucleation site of the precipitated phase. If the disregistry is between 6% to 12%, the inclusion is moderately effective to be the nucleation site. Moreover, if the disregistry is more than 12%, the inclusion has no effect on the nucleation of the precipitated phase.[110,112]

Apart from the lattice disregistry formulated by Bramfitt, Ohta and Suito[113] studied the lattice misfit between MnS and oxide inclusions and calculated the lattice misfit parameters by using the Equation (2.37).

$$Misfit = 2 \frac{|X_{MnS} - X_{oxide}|}{(X_{MnS} + X_{oxide})} \qquad (2.37)$$

where X_{MnS} and X_{oxide} are the lattice distance of MnS and oxide inclusions, respectively. The misfit corresponds to the minimum value among the various combinations of X_{MnS} and

X_{oxide} in Equation (2.36).[113] The lower the value of the misfit, the easier it is for the oxide inclusions to precipitate together with MnS inclusions. Ohta and Suito[113] showed the misfit parameter for the precipitation of MnS on the Al_2O_3 particle is above 0.1 but less than the misfit of MnS in ferrite α_{Fe}, which is greater than 0.25 (the misfit value also can be presented in percentage). So, the co-precipitation of Al_2O_3 and MnS is possible. Al_2O_3 will form first in liquid steel temperature due to its thermodynamic stability, and MnS will precipitate on it when the formation temperature of MnS is reached in the solidification process.

Ohta and Suito[113] applied Equation (2.37) to evaluate the misfit parameter for the precipitation of MnS on the AlN particle. It is reported that the misfit is less than 0.1. In other words, MnS is easier to precipitate on AlN inclusions (heterogeneous nucleation) rather than nucleate by itself. Another precipitation mechanism of AlN and MnS inclusions was explained by Lückl et al.[76] for low carbon steel grade. They mentioned that AlN could also precipitate on MnS inclusions because of the lattice parameter's similarity in their crystal structure. This mechanism is also supported by Tuling and Mintz[114], who investigated the precipitation of AlN in high Al TRIP steels. It is stated that MnS inclusion is a nucleation site for AlN because MnS has a similar lattice parameter with hcp AlN, and this precipitation mechanism happens when AlN is sluggish at high casting temperature near the solidification. Kang et al.[1] also agreed that under an equilibrium condition, AlN inclusion would appear first before MnS inclusion. However, under non-equilibrium conditions, MnS forms first before AlN forms.

Another formula that can be used to calculate the lattice misfit is displayed in Equation 2.38. Wang and Fan[115] use this formula to calculate the lattice misfit between inclusion particles in the Al melt. In this way, the feasibility of inclusion particles to be the nucleation substrate for α-Al grain can be evaluated. It was found that AlN is the least feasible among other particles (α-Al_2O_3, γ-Al_2O_3, $MgAl_2O_4$, and TiB_2) to become the nucleation substrate for α-Al grain, as its misfit value is the highest, 6.66%. Equation 2.38 can also be used to calculate the misfit between inclusion particles.

$$Misfit = \frac{|a_n - a_s|}{a_s} \times 100\% \tag{2.38}$$

where a_n and a_s are the lattice parameters of the nucleated inclusion and substrate, respectively.

2.8 Modification of Inclusions

Since it is difficult to make the steel completely free from inclusions, modification of inclusions is needed to make the inclusions less detrimental to the steel performance. A few methodologies to modify the inclusions are summarized below.

2.8.1 Modification of Inclusions by Calcium Addition

Calcium addition by powder injection or wire feeding is a common technique used in steel refining to modify oxide and sulfide inclusions.[22,25,116,117] A well-known example is modifying solid alumina inclusions into liquid or partially liquid calcium aluminates. Alumina is detrimental to the steel process because it can attach to the nozzle wall and cause a blockage of steel passing through the nozzle. The modification with calcium starts with Ca diffused into the steel. Ca reacts first with dissolved O and S in the steel, forming CaO and CaS.[25,117] Then, the remaining dissolved Ca reacts with alumina to form liquid calcium aluminate inclusions, and the nozzle blockage can be reduced.

The preferential order of reactions involved during modification of oxide inclusions by calcium is still not clear from previous works. The effect of dissolved sulfur on the modification of alumina inclusions by calcium has been qualitatively studied by Holappa and Ylonen.[118] Later, Larsen and Fruehan[119] conducted experiments to predict at what levels Al and S can form calcium aluminate and calcium sulfide inclusions. They stated that the sulfur level should be below 0.013% for 0.015% Al in liquid steel at 1550 ˚C. Verma et al.[120,121] also quantified the dissolved sulfur content for better modification of the alumina inclusions. They claimed that the sulfur content should be below 40 ppm to prevent CaS formation. These studies attempted to optimize the calcium addition for inclusion modification.

There are also a few studies[122–125] focusing on the changes in the composition of inclusions with time to determine the possible reaction kinetics. Higuchi et al.[122] investigated the effects of the addition rate and amount of Ca on the composition and shape of calcium aluminate inclusions. They also included the kinetics of the vaporization of calcium from the melt. Lu and Irons[126] investigated the kinetics and mechanisms of calcium dissolution and modification of calcium oxide and sulfide inclusions in the steel. They focused on the dissolution rate of calcium and ignored the reactions between inclusions and melt. Ito et al.[124] measured the soluble calcium, calcium oxide, and calcium sulfide content with respect to the time after Ca addition. They developed a relationship to express the conversion from alumina to calcium aluminate with time using a ratio of CaO content in inclusions to the calculated CaO content of calcium aluminates in equilibrium with liquid steel. They concluded that the rate-determining step for modifying alumina inclusion is calcium diffusion in the calcium aluminates product layer. However, the parameters, such as interdiffusivity in calcium aluminates, are not given. Alternatively, Han et al.[125] claimed that the chemical reactions between alumina and liquid calcium aluminate inclusions are the rate-controlling step.

Previous researchers[119,127] suggested that the ratio of $[Ca]_{total}/[O]_{total}$ should be greater than 0.6 for the good castability of the steel. In this ratio, the inclusions are mostly in the form of solid CA and liquid $(CaO)_{0.57}(Al_2O_3)_{0.43}$ at 1823 K. However, it is crucial to incorporate the effect of S. S in the steel reacts with Ca to form CaS inclusions, which are also detrimental to the casting process. Choudary and Ghosh[128] performed thermodynamic calculations to investigate the critical contents of Al and S in Al-killed steel to prevent solid

CA formation at 1823 K. It is predicted that $[mass\%Al]^2 \times [mass\%S]^3 = 2.05 \times 10^{-9} (a_{CaS})$ by considering the equilibrium reactions of Al_2O_3, CaO, liquid $C_{12}A_7$, solid CA and CaS inclusions. Fig. 2.16 plots the relationship between Al and S contents in the steel to avoid the formation of solid CaS by assuming $a_{CaS} = 0.75$. The steel composition should be below the line to prevent the formation of CaS inclusions before a liquid CA inclusion form. If the steel composition is above the line or S content is high, S tends to react first with Ca to form CaS until the S content becomes lower than the line. Then liquid oxide inclusions appear (Al_2O_3 inclusion transforms to CA).

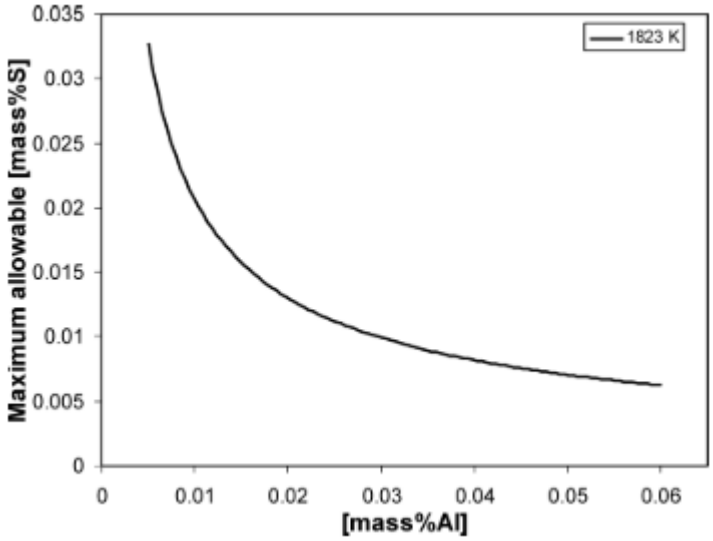

Figure 2. 16 The critical value of Al and S contents in the steel to avoid the formation of CaS inclusion at 1823 K and $a_{CaS}=0.75$.[128] – (Reprinted with permission)

Tabatabaei et al.[117] developed a model to predict the evolution of inclusions (e.g., Al_2O_3 inclusions) during calcium injection in the ladle furnace. The model includes the steel–slag reactions, steel–inclusion reactions, all possible rate-controlling steps, and the competition between alumina and sulfide inclusions for the consumption of Ca. The steps which the model took for the modification of alumina inclusions are 1) the dissolution of Ca into the steel bulk from the interface of gas bubble-steel, 2) transfer of the dissolved solutes including Ca in the boundary layer, 3) diffusion of Ca to the core of alumina, and 4) the chemical reaction between Ca and alumina. Before the injection of Ca, Al addition to the steel leads to the decrease of dissolved oxygen with alumina formation. As the dissolved oxygen content in the steel becomes low, the CaO in the slag is reduced and provides dissolved Ca in the steel. This dissolved Ca reacts with alumina rapidly and transforms it into calcium aluminate. The model also included the formation of a calcium aluminate layer on the surface of alumina inclusions. The growth of the calcium aluminate layer is predicted as the alumina becomes smaller. When the Ca is injected into the steel, it supplies more Ca and transforms faster. It makes the mole fraction of CaO in calcium aluminates increase until it reaches saturation and forms a CaO layer outside of the calcium aluminate layer. At this point, the modification of alumina stops, and the CaO layer becomes thicker. It was

found that the rate of calcium supply to the steel controlled the modification of alumina inclusions. The mass transfer of calcium through the inclusion boundary layer is extremely fast (only a few seconds). So, calcium is rapidly consumed by the inclusions.

Zhao et al.[129] conducted thermodynamic calculations to study the evolution of Al_2O_3 inclusions with calcium addition and performed industrial trials on Al-killed pipeline steels (with 0.04% Al, 12-16 ppm S, and ~20 ppm Ca in the slab). Initially, the types of inclusions are mostly Al_2O_3, MgO, and CaO. Then, after the RH refining process with Ca addition, the distribution of MgO–Al_2O_3–CaO in the phase diagram moves to the low melting region. The modified calcium aluminates become liquid. More Al_2O_3-CaS-contained inclusions formed in the slab due to the lower temperature in the process and segregation in the casting process. Zhao et al.[129] also studied the morphology of the inclusions after deformation in the hot rolling process. The small-sized (D < 20 μm) calcium aluminate inclusions with the CaS layer deformed well along the rolling direction while the MgO-Al_2O_3-CaO multi-component inclusions separated from its CaS layer and formed tails along the rolling direction. In the case of large-sized inclusions (D > 50 μm), C_3A+$C_{12}A_7$ inclusions are easy to deform with a smooth shape. On the other hand, C_3A+$C_{12}A_7$ and $C_{12}A_7$+CA with CaS layer separated with an irregular shape for the oxides and string shape for the CaS layer during deformation.

Besides the calcium modification by powder injection and wire feeding, Ca can be introduced from the slag. Jiang et al.[130,131] investigated the change in the shape of non-metallic inclusions with respect to time in the high-strength steels. The slag contained CaO, SiO_2, and Al_2O_3, while the steel consisted of C, Si, Mn, Cr, and Al. The steel and slag melted together in the magnesia crucible at 1600°C under argon gas. The shape of inclusions changed from rectangular to spherical due to the slag-steel reaction in the process. The change in the composition of inclusions was observed. First, the inclusions appeared to be MgO-Al_2O_3 type or MgO-based inclusions. Later, the inclusions were fully modified to spherical CaO-MgO-Al_2O_3 type complex inclusions. They studied the transformation mechanism of inclusion based on SEM-mapping. They suggested that there are two transformation mechanisms. (1) Al_2O_3 transforms into MgO-Al_2O_3 inclusion and then becomes CaO-MgO-Al_2O_3 inclusion. (2) MgO changes to MgO-Al_2O_3 and finally becomes CaO-MgO-Al_2O_3 inclusion.

2.8.2 Modification of Inclusions by Rare Earth Treatment

Rare earth (RE) elements or sometimes called mischmetal, consist of 15 elements in the lanthanide series such as Ce, La, Pr, and Nd that have identical chemical properties.[132] The composition of mischmetal is usually contained of 50% Ce, 25% La, and less Pr and Nd. RE elements are powerful deoxidizers and desulfurizers.[133–136] The advantage of using RE elements to modify inclusions is that they have good solubility in liquid steel, and they do not quickly vaporize. However, when they react with sulfur and oxygen in the steel, they form non-deformable and fine RE oxysulfide inclusions.[137–139] The density of RE

inclusions is around 5000-6000 kg/$m^{3,}$ near to liquid steel density [135,140]. Therefore, they do not easily float out and remain in liquid steel.[135,138]

Opiela and Grajcar[135] studied modification of non-metallic inclusions in the steel, containing sulfur and oxygen with RE in the form of mischmetal (~50% Ce, ~20% La, ~20% Nd). Their results showed that sulfur and oxygen reacted with mischmetal and formed dispersive, complex oxysulfide inclusions instead of forming MnS and Al_2O_3 inclusions.[135] This modification technique creates stable inclusions and a low value of elongation factor, making low susceptibility of inclusions to elongate in plastic working. It can decrease the austenite grain growth in hot plastic working, which is beneficial for producing high strength and ductility forging steel.

Grajcar et al.[138] identified type, fraction, and chemical composition of non-metallic inclusions modified by RE in high manganese austenitic C-Mn-Si-Al-type steels (Mn content was approximately 25-27%) with micro addition of Ti and Nb. The steel also contained sulfur. RE was added in the form of mischmetal at the very last stage of alloy additions. The susceptibility of inclusions to elongate in the rolling direction was reduced by increasing the mischmetal addition. The typical inclusions contained (Mn,Ti)S in the center and a phase with Ce, La, and Nb in the outer part of inclusions. Sulfide and oxysulfide inclusions contain RE elements formed, and they became hard to remove from liquid steel, so sulfur in high manganese steel should be reduced first.[138]

2.8.3 Modification of Inclusions by Other Elements

The addition of Te and Se can improve the machinability of martensitic or austenitic steel.[22,141,142] The shape of inclusions becomes globular with Te and Se additions so that the inclusions can deform well during the hot working process.[22] Se can modify the morphology of MnS inclusions in the steel. MnS becomes long and narrow stringers during the rolling process. The addition of Se can change the shape of MnS to globular.[22] The stringer inclusions become shorter units, which improves the machining properties.[22,143] Te and Se additions decrease the absorption rate of nitrogen in liquid steel and take part in grain refining structure. Thereby, they can reduce the hardenability and susceptibility for quench cracking in steel.[144]

Inclusion modification methods are not limited only to the approaches explained above. The influence of other elements, such as Ti and Mg, to modify inclusions in the steel is also studied.[145,146] Thapliyal et al.[145] used Ti to modify solid $MnO\text{-}SiO_2$ based inclusions present in low alloy Si-Mn deoxidized steel. The addition of Ti transforms the inclusions to a lower melting point in $TiO_2\text{-}MnO\text{-}SiO_2$ liquid inclusions. These liquid inclusions will avoid clogging in the thin-strip casting of the steel. Zhang et al.[146] used Mg to modify solid $CaO\text{-}Al_2O_3$ type inclusions in Al-Ca deoxidized melt. The addition of Mg reduces the size of inclusions from larger than 5 μm to around 2 μm.

2.9 Characterization of Inclusions

There are several tools and techniques for analyzing the characteristics of inclusions in steel, both directly or indirectly.[147–152] A scanning electron microscope (SEM), remelt buttons, pulse discrimination analysis (PDA), and ultrasonic testing are few direct methods[147,148]. In contrast, indirect methods include total oxygen content measurement, nitrogen pickup, steel/slag composition measurement, and final product test.[149,151] It is important to note that no single technique can provide all the information about the characteristics of inclusions.

Moreover, the appropriate methods should be chosen depending on the specific information needed. The inclusion analysis methods explained in the next sections are commonly used both in academia and the steel industry. These methods were considered because they give comprehensive information needed for inclusion analysis, are relatively time-efficient, and represent two and three-dimensional observations of inclusions.

2.9.1 Electrolysis Extraction (EE)

Understanding the complete morphologies of the inclusions can help to study the mechanism of the formation or growth of the inclusions. The three-dimension (3D) inclusion analysis technique, such as the electrolysis extraction (EE) technique, can be used to reveal the complete information about the size and morphology of inclusions. The extraction method's basic principle is dissolving only the steel matrix with a liquid solvent and leaving the inclusion particle as the remaining residue—the apparatus for the extraction process by Inoue et al.[153] is shown in Figure 2.17(a). A potentiostat is connected to the steel sample as an anode. The steel sample is held by the Pt tweezer and dipped into the electrolyte bath in the beaker. A Pt ring is also placed in the electrolyte bath in the beaker and acts as a cathode. A calomel electrode is set as a reference pole and connected by the electrolyte in the KCl-saturated solution and KCl-agar bridge. Then the solvent is filtered by polycarbonate (PC) films as the filter with a particular pore size in the vacuum filtration apparatus[154] as seen in Figure 2.17(b). The inclusion particles collected on the PC films are studied under SEM. There are several types of extraction methods, such as using acids, halogen-alcohol mixtures, and electrolysis.[153]

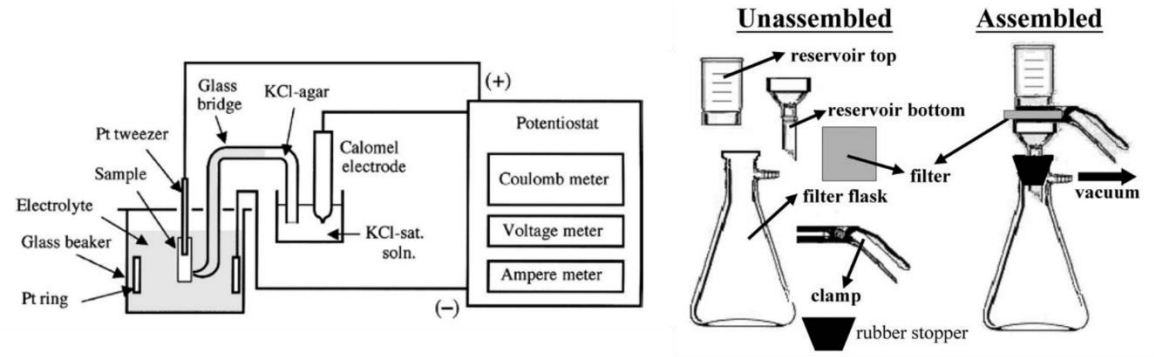

Figure 2. 17 The apparatus used for the potentiostat extraction method, (a) the schematic of the extraction process, and (b) the filtering container.[153,154] – (Reprinted with permission from Ref. 153 and Ref. 154)

Inoue et al.[153] reviewed the extraction technique using acids, which can accelerate the extraction of inclusions and have high chemical stability, such as SiO_2, Al_2O_3, Cr_2O_3, TiO_2, and $CaO{\cdot}6Al_2O_3$. On the other hand, the acids would dissolve Al_2O_3 and TiO_x inclusions. While the use of halogen-alcohol mixtures could overcome this problem, these mixtures tend to dissolve sulfides and alkaline earth metal oxides. The solution to these dissolution problems would be the use of electrolysis. It can extract different kinds of particles and selectively dissolve the metal matrix by adjusting the dissolution voltage. When the low current densities are applied, a passive layer is formed on the surface of the metal. So, the electrolyte, voltage, and current need to be carefully selected for the extraction process. It should be noted that this technique cannot be applied to extract the chemically unstable inclusions when using acid and neutral aqueous electrolytes.

Janis et al.[155] investigated the effect of electrolytes on inclusion analysis. The electrolytes that they studied were 5 v/v% bromine-methanol and 14 w/v% iodine-methanol for the halogen-alcohols, and 10% AA ((10 v/v% acetylacetone - 1 w/v% tetramethylammonium chloride - methanol), 4% MS (4 v/v% methyl salicylate - 1 w/v% tetramethylammonium chloride - methanol), or 2% TEA (2 v/v% triethanolamine - 1 w/v% tetramethylammonium chloride - methanol)) for the nonaqueous electrolytes. Furthermore, the current was 45–60mA, the voltage was 150mV, and the charge was 800 or 1200 coulombs. In order to make a quantitative analysis of the extraction methods, the dimension and the weight of the dissolved metals should be noted. The dissolved metals can be calculated using the following Equation (2.39).[155]

$$D_{dis} = \frac{W_{dis}}{\rho_{me} \cdot A_{sur}} \tag{2.39}$$

where D_{dis} is average dissolved depth, W_{dis} is the weight of the dissolved metal, A_{sur} is the surface area of the metal, and ρ_{me} is the density of the dissolved metal. Janis et al.[155] presented the relationship between the size range of the inclusion and the weight of

dissolved metals, as shown in Figure 2.18.[155] The size range of the inclusions was increased with the increasing mass of the dissolved metal. The EE method was suggested to be better and more precise for extracting various inclusion types, including clusters and particles in clusters. However, it needs more time than other methods.

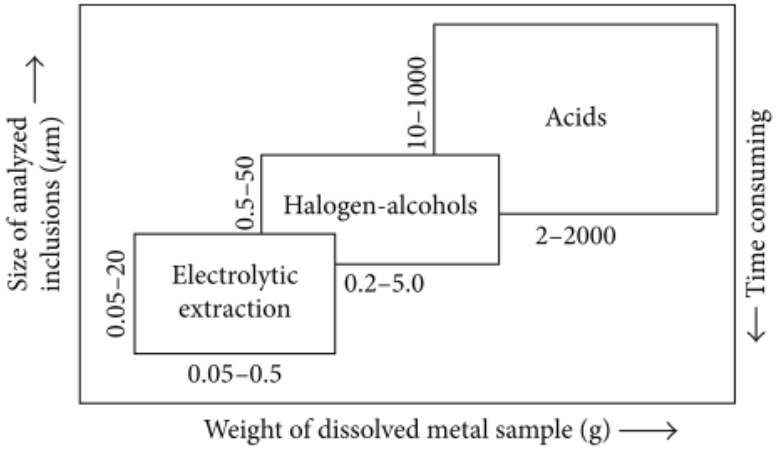

Figure 2. 18 The size of analyzed inclusions with respect to the weight of dissolved metal samples for different extraction methods.[155] – (Reprinted with permission)

2.9.2 Pulse Distribution Analysis with Optical Emission Spectroscopy (PDA/OES)

Pulse distribution analysis combined with optical emission spectroscopy (PDA/OES) is one of the direct methods for analyzing inclusions in the metal. This method can be classified as a fast analyzer since it only takes about 3-5 minutes to analyze inclusions.[156] The number and size of inclusions are characterized by the PDA index (size of the non-metallic inclusions is usually considered as the number of outliers on the intensity chart) or the B-factor (the total summed weight of elements in inclusions).[156] PDA/OES can also provide information on the concentration of soluble and insoluble elements in the metal.[157]

The principle of the PDA/OES method is shown schematically in Figure 2.19. Janis et al.[156] explained that the sample surface is ablated by the high-energetic discharge of electric sparks (around 3000-4000 sparks) with a frequency of 100-800 Hz. This excites atoms and ions in the plasma to elevate electronic energy levels. Moreover, the light of different wavelengths correlated to each element is emitted. In the spectrometer, the diffraction grating separates all those wavelengths. Then, the photomultipliers measure their light intensity. This way, the total mass fraction of each element from the sample is determined based on a particular calibration function. The ablated weight on 4000 sparks is around 2×10^{-4} g/measurement (per each spot), related to 2.56×10^{-2} mm^3/measurement.

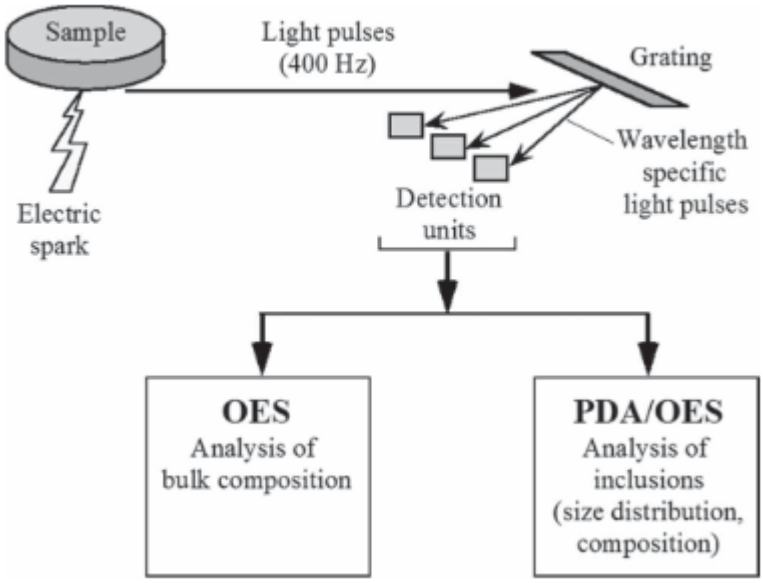

Figure 2. 19 Schematic illustration of a PDA/OES measurement.[156] – (Reprinted with permission)

The example of the single spark intensity (pulsograms) for Al in PDA/OES analysis is shown in Figure 2.20.[156,157] In Figure 2.20 (a)[156] and (b),[157] the outliers (high light intensity peaks) are related to the elements present in the inclusions. The outliers are the intensities that exceed the median intensity of the metal background (or the matrix of bulk intensity), Figure 2.20(a). These outliers are identified as a specified number of standard deviations (σ). An iterative calculation is used to determine this standard deviation (σ) value, including removing the large outliers. The inclusion type is identified by considering the detected outliers in a single spark. If two elements happen to be in the same spark, it is regarded as a complex inclusion that contains those two elements. All this information is processed in the PDA/OES software. All the number of outliers from the inclusions are collected and recalculated into the number of inclusions per unit volume of the sample. The size of inclusions is calculated from the intensity of every single outlier. The weight of ablated inclusions is estimated using the calibration function for the respective element.

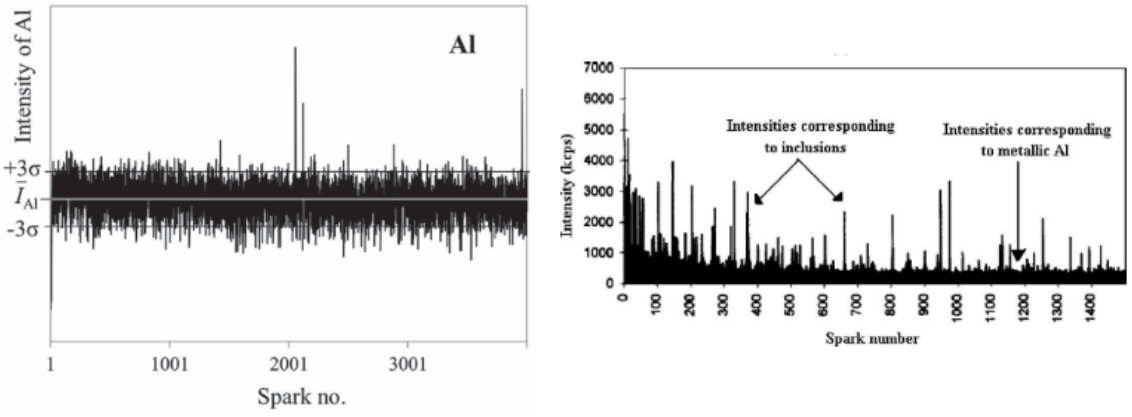

(a) (b)

Figure 2. 20 Typical intensity distributions obtained using PDA/OES.[156,158] – (Reprinted with permission fron Ref. 156 and Ref. 158)

The advantage of PDA/OES is its ability to distinguish the concentration of soluble and insoluble Al.[157] A single spark height distribution can be represented by the Gaussian function, as seen in Figure 2.21,[159] which shows the intensity distribution diagram for Al. The intensity of soluble Al follows the standard Gaussian distribution, and the insoluble Al shows an asymmetric shape of the graph. The ratio of the sum intensity of soluble Al and the total Al will be converted to determine the concentration of soluble Al and insoluble Al using the calibration curve.

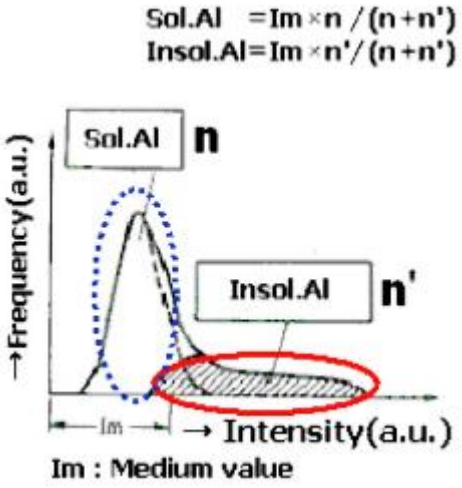

Figure 2. 21 Gaussian distribution for soluble and insoluble Al predicted by the PDA/OES measurement.[159] – (Reprinted with permission)

Along with the aforementioned capabilities of PDA/OES, steelmakers mostly rely on this technique to check the cleanliness and oxygen content of the steel during the steelmaking process. Its ability to provide the inclusion information in a short time allows the steelmakers to control the process in real-time.[156]

2.9.3 Ultrasonic Testing

Ultrasonic testing is another direct method for inclusion analysis. There are several types of ultrasonic testing equipment. The standard technique used in steel plants is Mannesmann inclusion detection by analyzing surfboards (MIDAS). This technique was used for detecting the macroscopic inclusion particles or clusters, which are rarely seen in the large volume of steel (slab, billet, or bloom of the steel).[160] The steel from the continuous casting will be flat cross-rolled perpendicular to the casting direction. The inclusions then will be deformed, and the shape changed mostly from globular to 'pancake,' which is helpful for ultrasonic beam detection. Then the surface of the steel will be analyzed by the ultrasonic probe to detect the inclusions. Nowadays, Liquid Sampling and Hot Rolling (LSHR) are used.[147] In this method, the liquid steel from the ladle or tundish is collected using a steel mould sampler (15 mm in thickness, 360 g in weight). The inlet pin of steel in the mould is used for total oxygen analysis, and the remaining sample will be rolled and heat-treated, and ready for ultrasonic testing. This method is also conducted for detecting macroscopic inclusions.

2.9.4 Total Oxygen

Total oxygen is the summation of the soluble oxygen in the liquid steel and the oxygen in the oxide inclusions (insoluble oxygen). The total oxygen measurement is one of the indirect methods for estimating the steel cleanliness level. This is a fast and easy method applied in the steel industry.[161] However, this method is only used for evaluating oxide inclusions, and it cannot provide information on the size distribution, chemical composition, and morphology of the inclusions. It is usually used in conjunction with other inclusion analysis techniques, such as SEM or Cathodoluminescence Microscopy (CLM), to collect more detailed information.

The total oxygen measurement is conducted by the oxygen analyzer, which uses an inert gas fusion method (e.g., LECO O/N analyzer or HORIBA O/N analyzer). In total oxygen analysis, the steel sample is placed in the graphite crucible. Then, it is fused at a temperature that allows oxygen to be released from the steel. During this process, the inert gas (Ar or He) is passed through the instrument system. The carbon from the crucible reacts with oxygen from the steel to form CO and CO_2 gases, which are then detected by an infrared or a thermal conductivity detector. Based upon the mass balance, the measured oxygen content associated with CO and CO_2 accounts for total oxygen in the steel sample.

Dekkers et al.[162] correlated the size of alumina inclusions with the total oxygen to investigate the cleanliness of low carbon Al-killed steel, Fe-(0.025-0.045%)C-(0.15-0.23%)Mn-(0.03-0.065%)Al, at Sidmar, as shown in Figure 2.22. The size represents the largest diameter of a particle measured by SEM (Figure 2.22(a)). The high total oxygen values and large scattering in Figure 2.22(b) represent the cluster of inclusions in medium carbon aluminum killed (MCAK), low carbon aluminum killed (LCAK), and low carbon silicon-aluminum killed (LCSAK) steels. Figure 2.22 shows that as the total oxygen decreased after Al addition, the size of inclusions was also reduced. The clusters of inclusions floated to the steel-slag interface and were removed by the slag after 15 minutes

addition of Al. As a result, the total oxygen decreased. The steel is left with aggregates and polyhedral types of inclusions.

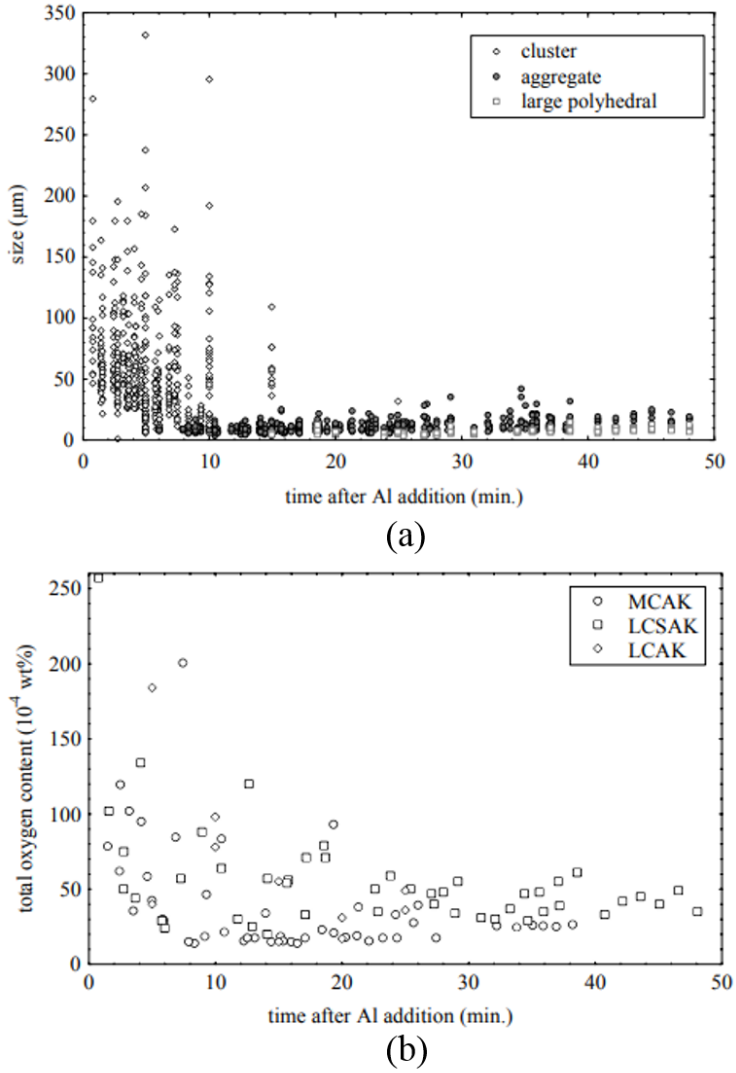

Figure 2. 22 (a) The size of inclusions and (b) the total oxygen in the medium carbon aluminum killed (MCAK), low carbon silicon-aluminum killed (LCSAK), and low carbon aluminum killed (LCAK) steels, Fe-(0.025-0.045%)C-(0.15-0.23%)Mn-(0.03-0.065%)Al, after Al addition at Sidmar.[162] – (Reprinted with permission)

2.9.5 Steel, Slag Composition Measurement and Final Product Test

The information on the elemental chemistry of steel and slag composition can also indirectly analyze the inclusions.[149] For example, when the dissolved Al content in the steel is reduced, it can imply that reoxidation likely occurs in the steelmaking process. Not

only does Al content act as an indicator for reoxidation, but manganese and silicon pick-up can also be an indicator. Monitoring the slag composition before and after an operation can indicate inclusion absorption in the slag or a possibility of reoxidation from the carryover slag. In addition, the slag entrainment can be investigated by comparing the slag and inclusion compositions.

Another indirect method is the destructive mechanical testing of the final product.[149] This testing informs about the deep-drawing properties, formability, bending properties, or fatigue life of the steel. This measurement can be related to the steel cleanliness because the inclusions can be the source of the problem if one of those properties in the steel is unacceptable.

2.9.6 Automated Scanning Electron Microscopy (SEM) Inclusion Analyzer

In the steel industry, automated scanning electron microscopy (SEM) inclusion analyzer has become a crucial tool because it provides information on inclusion characteristics relatively fast and comprehensively compared to the regular SEM analysis. The automated SEM inclusion analyzer has the same principle as regular SEM. However, it has an added program to detect particles automatically, faster than manual detection by a human. The high-resolution scan is used to define the inclusion parameters. Afterward, Energy Dispersive X-ray Spectroscopy (EDS) data is used to determine the composition of inclusions.

Furthermore, inclusions are classified based on their composition by using predetermined rules developed by the operator. ASPEX,[163] ASCAT,[164] and INCA[165] are commonly used programs for automated SEM inclusion analyzers. All the programs have the same basic principle; however, each has its specific method and settings to identify inclusions.

The information obtained from the automated SEM inclusion analyzer is particle size distribution, composition, 2D morphology, and the location of inclusions on the surface of the steel sample. Figure 2.23 compares the inclusion analyzers with respect to inclusion frequency and size.[166] As seen in Figure 2.23,[166] image analysis and ultrasonic analysis are used for analyzing the macro size of inclusions (>20 μm). On the other hand, both automated SEM/EDX and light optical counting almost cover all the size range of inclusion. However, they are usually used to analyze the micro-sized of inclusion (1-20 μm).

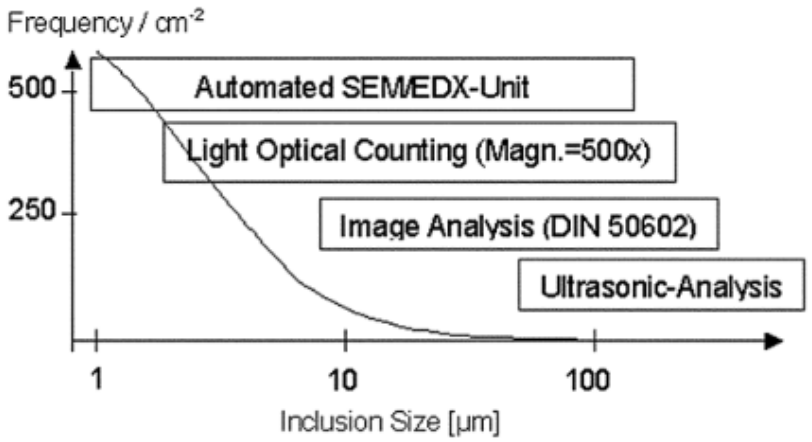

Figure 2. 23 The frequency of inclusions with respect to the inclusion size measured by different inclusion analyzers.[166] – (Reprinted with permission)

In this study, the ASPEX feature is used in the automated SEM inclusion analyzer, and the details of this program are further described. Schamber[163] explained that the particle is investigated in the frame-based analysis in the ASPEX feature, and the SEM is used as a camera. First, it starts with positioning the stage. Then the camera captures the field of view of the steel surface, as seen in Figure 2.24(a). This field of view is then transferred to the computer (Figure 2.24(b)). Furthermore, the software algorithm processes the frame and goes through each feature or particle and makes a tracing around the particle, then measures it (Figure 2.24(c)). After that, the computer places the microscope optics to align the beam at particular coordinates to calculate the x-ray spectrum. These steps are conducted on all the features or particles in this field of view. When all the particles have been analyzed, the same steps are performed in the next field of view.

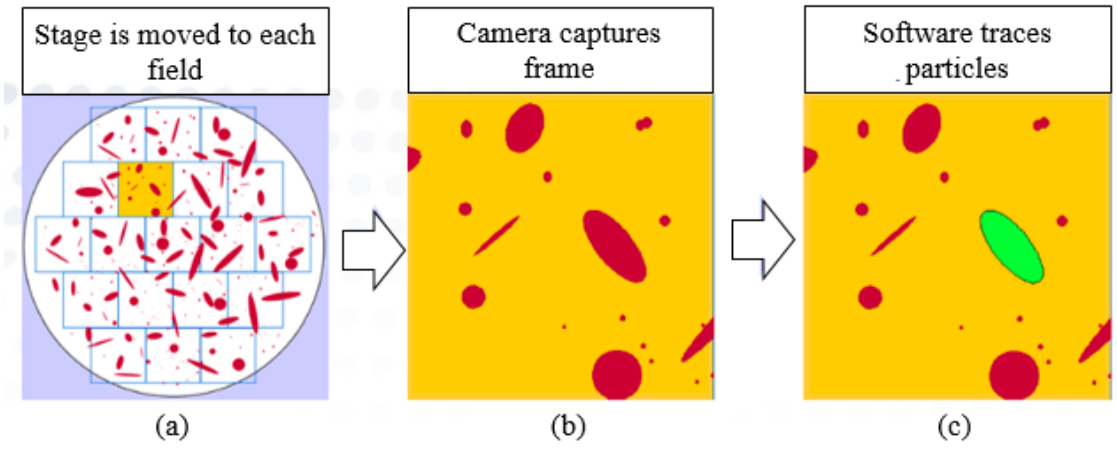

Figure 2. 24 Frame-based analysis of particles.[163] – (Reprinted with permission)

Schamber[163] described the additional step that ASPEX does to detect a particle. When the stage is positioned in one field, as seen in Figure 2.24(a), it is subdivided again into 16 small fields, which are called magnified fields, as shown in Figure 2.25(a). This additional step is conducted to analyze the inclusions in the field accurately. The beam moves across the field. In each step, the brightness of the back-scattered electron signal is noted. Furthermore, in every 16 small fields, it is divided into the coarse grid of sampling points (Figure 2.25(b)). The spacing between the points is not larger than the smallest particle of interest. So, if there is a particle smaller than the spacing grid, it will not be detected. This selection step is conducted to save time for analysis.

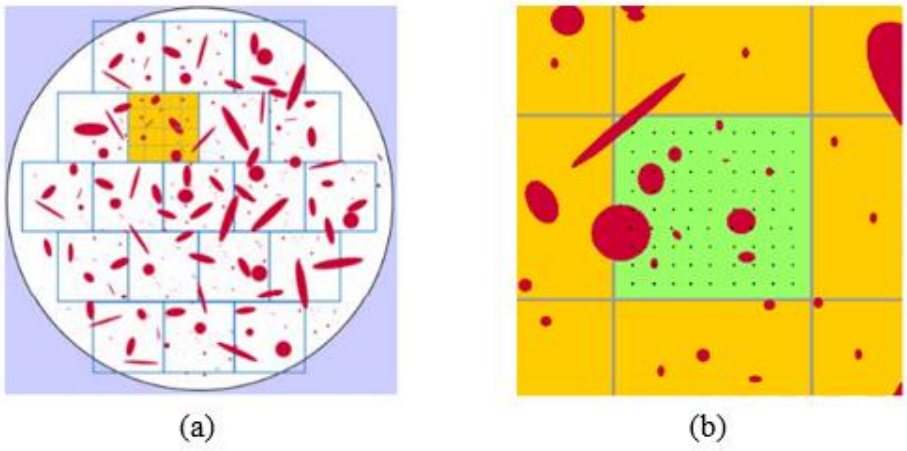

Figure 2. 25 Additional steps in the ASPEX system.[163] – (Reprinted with permission)

Particle sizing starts by identifying the center of the particle. It follows the bisected chord method. The beam moves horizontally (first horizontal chord) in small steps until the signal detect is lower than the threshold (Figure 2.26(a)). Then the beam moves downward until it reaches the bottom edge of the particle. When it is finished, this vertical chord is bisected in the center, and a new horizontal chord is established in the center of the vertical chord (Figure 2.26(b)). These steps are then repeated until the geometric center of the particle is found (Figure 2.26(c)). A series of rotating chords are then made through the center, as seen in Figure 2.26(d). The average length of the chords is used for calculating the average diameter of the particle. The longest and shortest chords are used to calculate the aspect ratio.[163] When all the information regarding the size, shape, and composition is gathered, the inclusion is classified using predetermined classification rules developed by the user. All the steps mentioned are conducted in each particle. This process could have a rate of 500 particles/minute when the x-ray spectra are not collected, and it adds a few seconds for each particle to collect the x-ray spectra.[163]

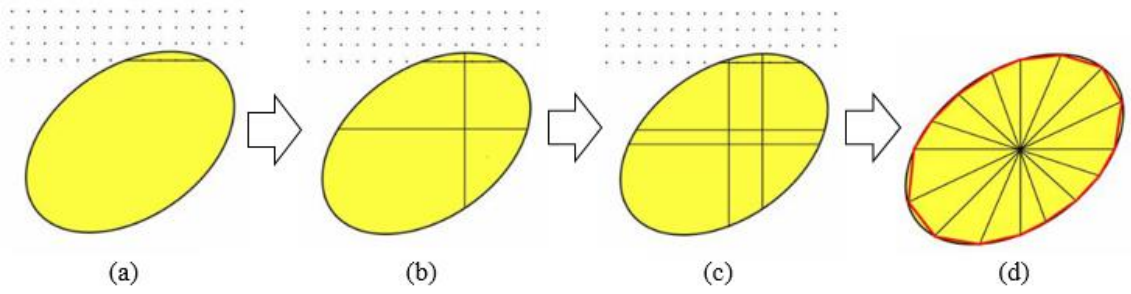

Figure 2. 26 Particle sizing steps in ASPEX.[163] – (Reprinted with permission)

Among all the inclusion analysis methods described in this section, the automated SEM (ASPEX) is used intensively in the present study. This method has been used rarely to analyze inclusion characteristics in the latest generation of AHSS,[80,84] and it has a potency to be applied for studying the inclusion characteristics comprehensively in medium and high manganese steels and will be discussed in the present study.

2.10 Gap of Knowledge

Currently, classical metallography and SEM analysis techniques for inclusions in steel have been widely used to analyze the morphology and composition of inclusions in liquid steel. Even though these techniques have provided important information, it is qualitative and time-consuming. In addition to being time-consuming, an analysis of a small area of the sample raises questions on how representative is the result of the analysis.[167–169] The SEM technique has become automated, so it can detect large numbers of inclusions (>5000) and assess the size and composition of inclusions in the steel. The ASPEX, ASCAT, and INCA Feature, automated SEM inclusion analysis techniques, reduced inclusion analysis times to a few hours on something that would have previously taken weeks.[167–169] The application of these techniques in inclusion studies reduces the uncertainty in inclusion analysis. Moreover, an automated SEM technique is commonly designed and used for analyzing oxide and sulfide inclusions. Few studies[81,82] applied an automated SEM technique in high manganese steels. Even though they reported the detection of nitride inclusions, they did not discuss the systematic method for differentiating nitride inclusions from oxide and sulfide inclusions. The present study is intended to fill this gap for medium manganese steels and high manganese steels.

Even though the previous studies on steel cleanliness provided some insight into the evolution of the inclusions, there are still limited studies on the characteristics of the inclusions in the latest generation of AHSS, especially in the high manganese steels and medium manganese steels. Several studies[78–82] focused on the effect of steel chemistry on the inclusion formation in high manganese (Mn = 10-30%) steel. The types of inclusions observed are mostly single AlN, single Al_2O_3, single MnS(Se), AlN·MnS(Se), AlN core with MnS(Se) wrap, Al_2O_3·MnS(Se), Al_2O_3 core with MnS(Se) skin, MnO·Al_2O_3·SiO_2, Al_2O_3·CaO, and AlN·Al_2O_3·MnS(O,Se) inclusions. It is suggested that AlN inclusions can be formed in the liquid steel and during the solidification of the steels. The previous study[170] in medium manganese steel focused on the formation of MnO-Al_2O_3 spinel

inclusions. Another study[9] only looked into the effect of Mg addition in different Al content of medium manganese steel (Mn = 9%). However, several questions still need to be addressed regarding the effect of individual solute elements on the formation, size distribution, and morphology of inclusions. In addition, complex inclusions are found in the medium manganese steels and high manganese steels. However, the formation mechanism of those complex inclusions is not explained well.

A further problem in laboratory studies in steel cleanness is that there is a tendency for the crucible material (usually Al_2O_3 or MgO) to react with the inclusions, thereby "cleaning" the steel. The principal problem when this happens is finding any inclusions in the steel. This problem can be overcome by applying cold crucible levitation melting techniques or performing thermodynamic calculations to confirm that no inclusions react with the crucible before conducting any experiment. Finally, since the inclusions in the steel cannot be removed completely, the modification of detrimental inclusions is required. There is still no study on the modification of inclusions in medium and high manganese steels.

The research on inclusion characteristics in medium manganese steel and high manganese steel is addressed in the present study by giving a systematic investigation of the inclusion formation in the medium manganese steel and high manganese steel with different contents of main alloying elements such as Mn, Al, and N. The experimental technique has been developed to assess inclusion changes with time during processing and explained in detail in the present study. The method involves the production of synthetic steel melts in a controlled system. It is believed that this approach will overcome the inherent reproducibility and uncertainty problems associated with the use of industrial steel melts. Furthermore, different amounts of alloying elements offer the possible to understand changes in the formation mechanism of inclusions in the steels investigated in the present study. The inclusion analysis for medium manganese steels and high manganese steels has been conducted using an automated SEM (ASPEX Feature).

Chapter 3

Investigation of Inclusion Formation in Light-Weight Fe–Mn–Al Steels using Automated Scanning Electron Microscope Equipped with Energy-Dispersive X-Ray Spectroscopy

Chapter 3 is a pre-publication version of the article published in Steel Research International 2020, Volume 91, Issue 3, DOI: 10.1002/srin.201900477. The following chapter describes the systematic technique for the characterization of inclusions in the Fe-Mn-Al steels with medium manganese content and high manganese content. Even though previous studies suggested that oxide, sulfide, and nitride inclusions are present, there is no discussion available on the inclusion classification rules for such systems in the open literature. One of the aims of this chapter is to establish inclusion classification rules for inclusions in medium manganese steels and high manganese steels. For this purpose, two-dimensional and three-dimensional inclusion observation methods were employed. For two-dimensional observations, the detection and analysis of inclusions were performed by an automated scanning electron microscope (SEM) equipped with the ASPEX feature. The three-dimensional analysis was conducted by the electrolytic extraction (EE) technique to reveal the complete morphology and composition of inclusions. The proposed approach enabled us to classify the oxide, sulfide as well as nitride inclusions. The provided methodology can help other researchers and steelmakers apply more explicit use of classification rules in their analysis.

This chapter also investigated the effects of manganese content (2, 5, and 20%) on the characterization of inclusions in laboratory-produced Fe-Mn-Al steels. It was found that the increase of manganese content increased the total number of inclusions, especially AlN-containing inclusions. Moreover, the formation of AlN-containing inclusions was explained by considering their thermodynamic parameters and morphologies. It is concluded that AlN inclusions formed during the cooling and solidification of steel due to its low nitrogen content. Moreover, Al_2O_3 and AlN inclusions can be the heterogeneous nucleation site for MnS inclusions. Furthermore, MnS inclusions can act as a nucleation site for AlN inclusions.

All the experiments, data collection, and analysis were completed by the primary author. Li Sun (ArcelorMittal Dofasco) provided training for using automated SEM (ASPEX). Dr. Muhammad Nabeel assisted with the mapping of the inclusions and the electrolysis extraction analysis. The manuscript was drafted by the primary author. Dr. Muhammad Nabeel and Dr. Neslihan Dogan contributed to the discussions and proofread the manuscript.

Investigation of Inclusion Formation in Light-Weight Fe–Mn–Al Steels using Automated Scanning Electron Microscope Equipped with Energy-Dispersive X-Ray

Michelia Alba,* Muhammad Nabeel, and Neslihan Dogan

Michelia Alba, Ph.D. Student, albam@mcmaster.ca
Department of Material Science and Engineering, McMaster University, 1280 Main Street West, Hamilton, ON L8S 4L7, Canada

Muhammad Nabeel, Postdoctoral Fellow,
Department of Material Science and Engineering, McMaster University, 1280 Main Street West, Hamilton, ON L8S 4L7, Canada

Neslihan Dogan, Assistant Professor,
Department of Material Science and Engineering, McMaster University, 1280 Main Street West, Hamilton, ON L8S 4L7, Canada

Abstract

Herein, the effect of Mn content on the characteristics and the formation of inclusions in light-weight Fe–Mn–Al steels are investigated. Three laboratory-produced steels, containing different manganese contents (2%, 5%, and 20%) are investigated. 2D and 3D inclusion characterization methods are used to establish inclusion classification rules for oxide, sulfide, and nitride inclusions using an automated scanning electron microscope (SEM) equipped with energy-dispersive X-ray spectroscopy (EDS) (ASPEX system). The observed inclusions are classified into $Al_2O_{3(pure)}$, Al_2O_3–MnS, $AlN_{(pure)}$, AlN–MnS, AlON–MnS, AlON, and MnS. The results show that an increased Mn content of steel increases the number of inclusions, especially Al_2O_3–MnS and AlN–MnS inclusions. In the case of Al_2O_3–MnS inclusions, Al_2O_3 inclusions serve as the site for the precipitation of MnS. Thermodynamic calculations suggest that the AlN-containing inclusions formed during cooling and solidification of steels. Moreover, the formation of AlN–MnS inclusions can take place by the nucleation of MnS on AlN inclusions and vice versa.

3.1 Introduction

In the past decade, light-weight Fe–Mn–Al steels, also known as advanced high strength steels (AHSSs)[1] have increased commercial and scientific interests due to their notable mechanical properties. The combination of light-weight and ultrahigh strength makes these steels more attractive than the conventional steel grades, especially for automotive applications.[2,3] Their outstanding performance is directly related to their main alloying

elements, which are 2–25% Mn (provides the austenite structure), ≤ 3% Si (controls the solution strengthening), and ≤ 9% Al (reduces the weight and increases the stacking fault energy).[3,4]

The high alloying elements in AHSSs lead to the formation of complex nonmetallic inclusions. Park et al.[5] found that Al_2O_3, AlN, $MnAl_2O_4$, Al_2O_3(-Al(O)N), Mn(S,Se), oxide core with MnS, and MnS with Al_2O_3(-Al(O)N) were the main inclusions present in Fe–Mn–3Al-alloyed steels. They reported that the number of Al_2O_3, $MnAl_2O_4$, and MnS with AlN inclusions increased by increasing the Mn content from 10% to 20%. Zhuang et al.[6] investigated the inclusions present in the Fe–25Mn–3Si–3Al steels produced in a laboratory, an argon–oxygen decarburization (AOD) process, and an electroslag remelting (ESR) process. It was observed that Al_2O_3, AlN, and MnS were the dominant inclusions in samples produced in the laboratory and the AOD process, whereas $MnO{\cdot}Al_2O_3{\cdot}SiO_2$-type inclusions were the dominant inclusions in the ESR process. Gigacher et al.[7] also reported the presence of Al_2O_3–MnO with AlN and/or MnS, single AlN, and single MnS inclusions in (15–25) Mn–3Al–3Si steels. Several other studies have reported similar types of inclusions present in AHSSs.[5,6,8]

The presence of AlN-containing and a higher number of MnS-containing inclusions is peculiar to AHSSs. The formation of AlN inclusion is dictated by increased nitrogen solubility in liquid steel due to its high Mn content.[9] Further, the presence of AlN inclusions can lead to a higher number of MnS-containing inclusions.[8] AlN and MnS inclusions can coprecipitate, due to their similar lattice parameters.[10] Both AlN and MnS inclusions can be harmful to the properties of steels. MnS inclusions decrease the toughness of the steel due to deformation during hot rolling[11] whereas AlN inclusions are known to contribute to the poor hot ductility of steel.[12,13] Therefore, it is crucial to investigate the characteristics of these inclusions, especially coprecipitation behavior and the resulted morphology.

The most common method of inclusion analysis is to observe inclusions on a polished cross-section of steel samples using a scanning electron microscope (SEM) equipped with energy-dispersive X-ray spectroscopy (EDS). Moreover, the use of automated SEM analysis, such as ASPEX and INCA Feature, has become a common practice in the steel industry for quality inspection and research purposes. However, automated SEM systems are generally designed to mainly detect oxide and sulfide inclusions and have limitations for quantification of nitride inclusions.[14] Several researchers used automated SEM systems to analyze inclusions in Fe–Mn–Al steels and reported the detection of AlN-containing inclusions.[4,7,8] Gigacher et al.,[7] based upon thermodynamic calculations, modified the inclusion classification guidelines in their analysis system to adopt for the investigated steels. However, the details of classification rules/guidelines for inclusions in Fe–Mn–Al steels are not given in any of the studies mentioned earlier.

Therefore, this study presents a systematic work conducted to develop inclusion classification rules for an automated SEM analysis (ASPEX) of inclusions in Fe–Mn–Al steels. For this purpose, different inclusion characterization techniques are used. Further,

the effect of manganese content on the characteristic of inclusions in laboratory-produced Fe–Mn–Al steels are investigated. The formation of the detected inclusions is discussed by considering their thermodynamics and coprecipitation behavior.

3.2 Experimental Section

3.2.1 Methodology and Materials

The experimental work focused on the effect of manganese content in molten steel on the evolution of inclusions relevant to steelmaking conditions. In experimental steels, the manganese content was varied between 2% and 20%, whereas the aluminum, silicon, and carbon contents were kept constant at 3%, 3%, and 0.1%, respectively. In this study, the synthetic steel melt was produced from reagent grade materials. Electrolytic iron (99.97%) and silicon lump (99.95%) were purchased from North American Höganäs and Goodfellow, respectively. Electrolytic manganese (99.9%), iron nitride (≈7% N), and aluminum shot (99.99%) were supplied by Alfa Aesar. The graphite rod was purchased from McMaster Carr. The experimental set-up is schematically shown in Figure 3.1.[14,15] A resistance-heated vertical tube furnace was used. A 500 g synthetic steel was placed in an alumina crucible from the bottom of the furnace. To achieve low oxygen potentials, argon gas (5 N purity, flow rate 0.5 L min^{-1}) was passed through the titanium turnings at 973 K (700 °C) to remove oxygen. An oxygen sensor was connected to the gas outlet to measure the partial pressure of oxygen during the experiments. The partial pressure of oxygen was ≈10^{-20} atm throughout the experiment.

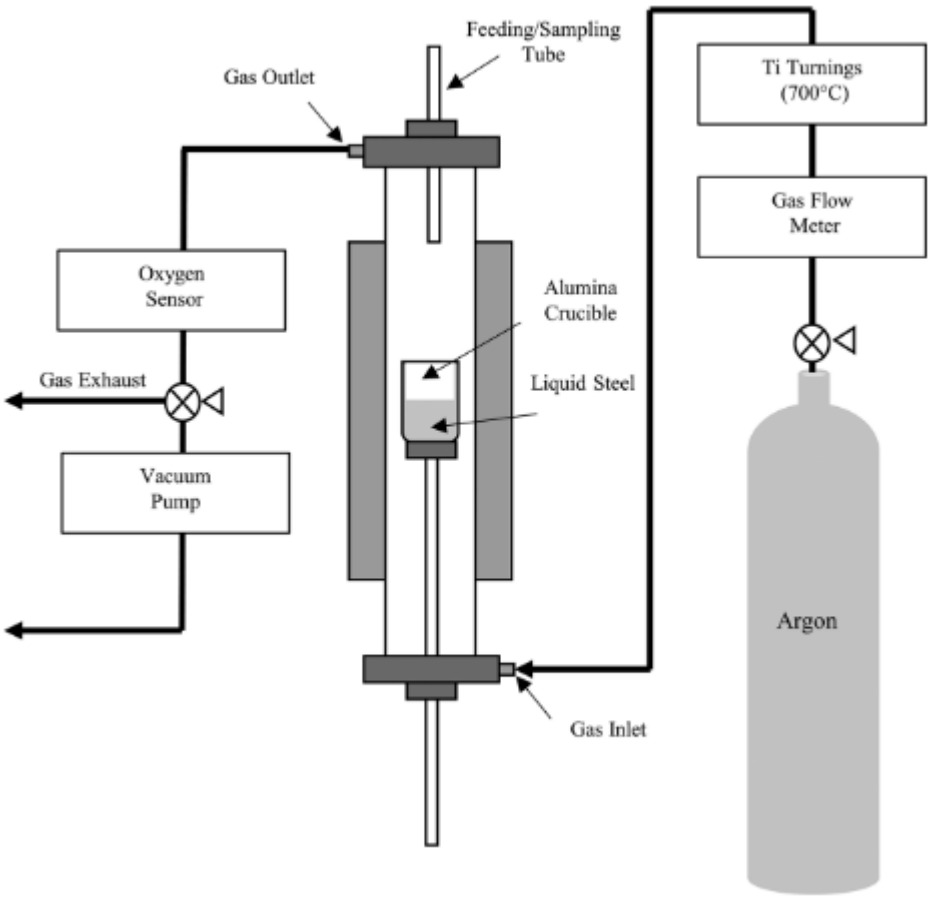

Figure 3. 1 Schematic diagram of the experimental set-up used. Reproduced with permission.[14] Copyright 2018, Association for Iron and Steel Technology (AISTech). Reproduced with permission.[15] Copyright 2019, Springer Nature.

The furnace was heated to the experimental temperature of 1873 K (1600 °C) under controlled atmosphere conditions. After 30 min of homogenization, the system was evacuated and backfilled with argon gas. Thereafter, the first sample (S1) was taken. It was followed by the addition of the Al_2O_3 particles (≈0.6 g), containing ≈40% of particles in the size range 2–3 μm. The synthetic inclusions were added by the technique developed by Dogan et al.[16,17] in which inclusions are compacted between steel sheets to make a steel-inclusion "sandwich." The composition of the industrial steel sheet used in this study for making the steel-inclusion "sandwich" was 0.16% Mn, 0.02% C, 0.04% Al, 0.004% Si, 30 ppm N, and 60 ppm S. This type of industrial steel was chosen because it is low-alloyed steel and only contains a small amount of Al_2O_3 inclusions (2–4 μm size), which will not complicate the inclusion analysis. Time zero was defined as the time when the inclusion addition was made. Several pin samples at different holding times were obtained from the top of the furnace using a quartz tube (5 mm ID) and they were air-cooled. The details of the sampling sequence are shown in Figure 3.2. The remaining bulk steel was cooled along with the furnace, at a cooling rate of 10 °C min^{-1}. All of the pin and bulk samples were

prepared for the chemical analysis. The carbon and sulfur contents were measured by a LECO C/S analyzer (HF-400), and the oxygen and nitrogen contents were determined by a LECO O/N analyzer (ON736). Manganese, aluminum, and silicon contents were analyzed by induction-coupled plasma optical emission spectrometry (Vista-PRO CCD simultaneous ICP-OES).

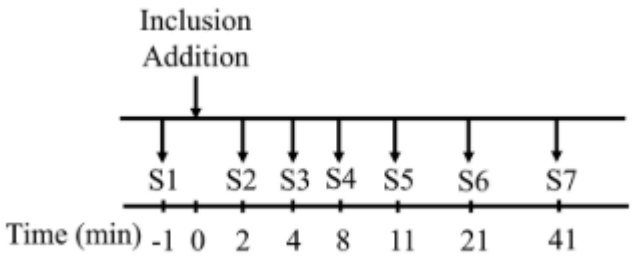

Figure 3. 2 The sampling sequence of an inclusion evolution experiment.

3.2.2 Characterization of Inclusions

The characteristics of inclusions were studied by 2D and 3D analysis techniques. For 2D observations, inclusions on a polished cross-section were analyzed using the ASPEX inclusion analysis system. ASPEX is an automated SEM equipped with EDS and the automated feature analysis (AFA) software for inclusion characterization, including size, number, distribution, and composition of inclusions. The investigation was conducted using a step size of 0.88 μm, 20 kV accelerating voltage, 43.4 μA emission current, and 35% spot size. A magnification of 356× was used. The analyzed area for each sample varied between 15 and 50 mm^2. The detected number of inclusions was around 200–3800. In this analysis, inclusions with the maximum diameter (D_{max}) > 2 μm were detected. In addition to automated inclusion analysis (ASPEX analysis), SEM-EDS was used to attain details such as phase distribution in inclusions through elemental mappings at higher magnifications. Hereafter, this analysis is referred to as manual SEM analysis.

For 3D observations, an electrolytic extraction method was used. For electrolytic extraction of inclusions, a metal sample (0.1–0.2 g) was dissolved in 10% AA (10 v/v% acetylacetone—1 w/v% tetramethylammonium chloride—methanol) electrolyte by applying the following electrical parameters: 50–60 mA (current) and 2.7–3.5 V (voltage). After extraction, the electrolyte containing the extracted inclusions was vacuum filtered through a polycarbonate (PC) film filter with a pore size of 0.4 μm. The extracted nonmetallic inclusions were observed in 3D using an SEM-EDS.

3.2.3 Classification Rules for ASPEX Analysis

The used ASPEX analysis system was originally designed to detect and classify nonmetallic inclusions into oxide and sulfide inclusions. This was done in accordance with user-defined classification rules. Due to the presence of nitride inclusions in AHSS,[5,6,8,12,14,18] it was necessary to establish appropriate inclusion classification rules for high-manganese steels. This was done by conducting a five-stage inclusion analysis. For

this purpose, the bulk sample with 5% manganese content (533) was used for the analysis. The following steps were involved in establishing the classification rules.

Step 1: Determine typical inclusion types in experimental steel via manual SEM and 3D observations

Step 2: Conduct ASPEX inclusion analysis using default classification rules

Step 3: Conduct post-ASPEX analysis

Step 4: Create and update the classification rules

Step 5: Redo ASPEX inclusion analysis using the updated classification rules

In Step 1, the chemistry of inclusions was analyzed, using manual SEM and 3D observation methods, to determine typical types of inclusions present in the steel. For this purpose, EDS elemental mappings and point analyses were conducted on 28 inclusions. It was found that the major kinds of inclusions consisted of Al_2O_3, AlN, and MnS. In addition, multiphase inclusions containing different combinations of Al_2O_3, AlN, and MnS were also observed. Both analysis methods, manual SEM and 3D observation showed consistent results which were in agreement with the previous studies.[5,8,14] Figure 3.3 shows elemental mappings (Kα1 peaks) of typical multiphase inclusions observed in the steel sample using the manual SEM method. A combination of MnS with Al_2O_3 is shown in Figure 3.3(a), where Al_2O_3 is present in the core, and MnS is surrounding it. Similarly, an example of MnS combined with AlN is shown in Figure 3.3(b). Moreover, complex multiphase inclusions containing Al_2O_3, AlN, and MnS were also observed (see Figure 3.3(c)). The 3D morphology of these multiphase inclusions is shown in Figure 3.4.

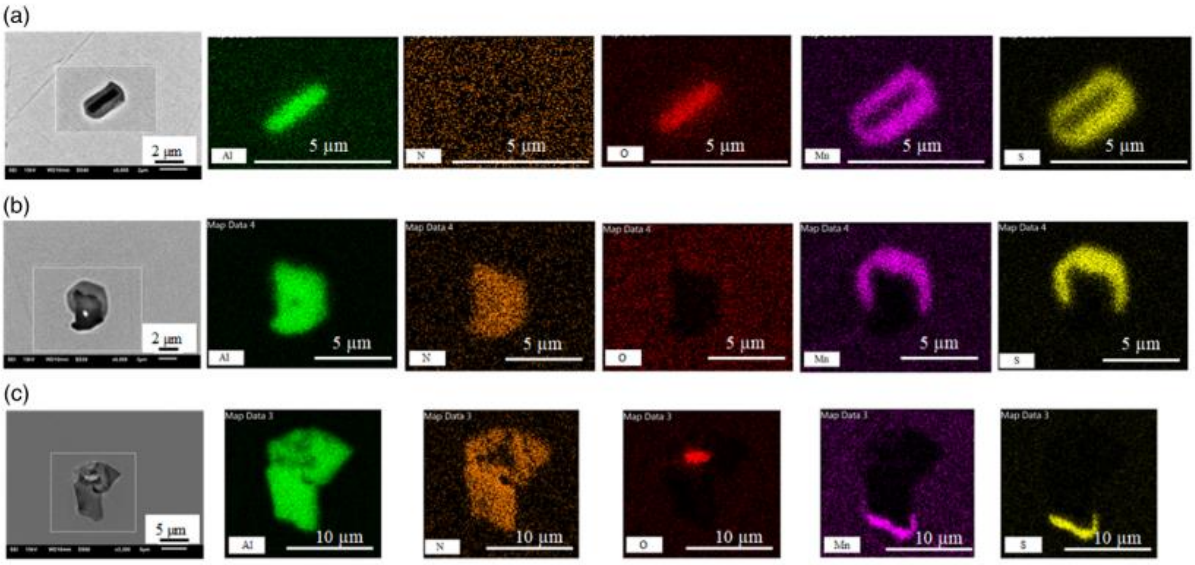

Figure 3. 3 Elemental mappings of (a) Al_2O_3-MnS, (b) AlN-MnS, and (c) AlON-MnS multiphase inclusions observed in steel using manual SEM.

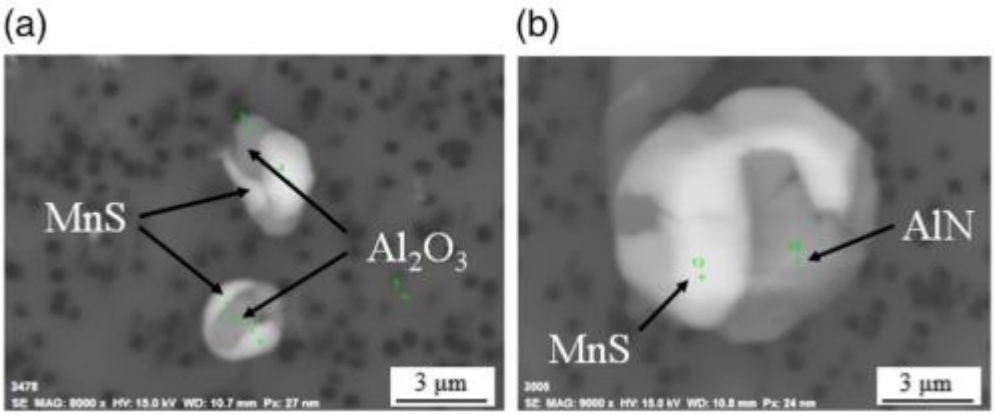

Figure 3. 4 3D morphology of multiphase inclusions observed in the steel sample, (a) Al_2O_3-MnS and (b) AlN-MnS inclusions.

In the second step, inclusions on a polished cross-section were detected by the ASPEX analysis system. Here, a small sample area (4.85 mm^2) was analyzed and the default classification rules were used to categorize the detected inclusions in different classes. The average inclusion composition was obtained by automated EDS analysis, where chord raster mode was deployed. A total of 39 inclusions, having a maximum diameter (D_{max}) > 2 µm, were detected. In the post-ASPEX analysis (Step 3), the chemistry of all 39 detected features was analyzed by doing EDS point analyses on them. The spectra of oxygen and nitrogen elements were added for these EDS analyses. In the case of multiphase inclusions, an EDS point analysis was conducted for each phase. Moreover, their average

compositions were also obtained by EDS area analysis. The chemistry of detected inclusions was in accordance with that observed in Step 1 analysis.

Based upon Step 1–3 results, the inclusions detected in the steel samples were classified into four major classes, i.e., Al_2O_3, AlN, MnS, and other, where the "other" class contains inclusions that do not fall in the aforementioned types. In Step 4, Al_2O_3- and AlN-type inclusions were further classified into subclasses according to the presence of other phases. The details of these subclasses and their classification rules are shown in Table 3.1. The detected inclusions were classified into subclasses according to the sequence, as shown in Table 3.1 to properly place the inclusions into the right class. The composition of single-phase inclusions such as $Al_2O_{3(pure)}$, $AlN_{(pure)}$, and MnS was set to exclude any element other than their base elements (i.e., Al—O, Al—N, and Mn—S, respectively). However, for the complex inclusions, the constraints for Al, O, N, Mn, and S were adjusted as shown in Table 3.1. After determining the major and subclasses of the inclusions and defining the classification rules, a new algorithm containing the definition of AlN-containing inclusion classes was introduced in the ASPEX system. In updated classification, AlN-containing inclusions were ranked after Al_2O_3-containing inclusions considering higher stability of Al_2O_3 as compared with AlN inclusions.

Table 3. 1 Inclusion classification rules for Fe-Mn-Al steels

Classes	Sub-classes	Major composition (%)
Al_2O_3	$Al_2O_{3(pure)}$	Al > 10, O > 50
	Al_2O_3-MnS	Al ≤ 40, O > 1, Mn ≤ 80, S ≤ 40
AlN	$AlN_{(pure)}$	Al ≥ 15, N > 40
	AlN-MnS	Al ≤ 60, N ≤ 65, Mn ≤ 80, S ≤ 50
	AlON-MnS	Al ≤ 40, O ≤ 70, N ≤ 55, Mn ≤ 80, S ≤ 50
	AlON	Al > 0, O ≥ 4, N > 0
MnS	MnS	Mn ≥ 25, S ≥ 10
Other	Complex oxide	Else

In Step 5, the same area, which was analyzed by the ASPEX system in Step 2, was reanalyzed using the updated classification rules introduced in the ASPEX system. It is important to note that the detection of oxygen and nitrogen during EDS area analysis was enabled for this step. Again, the same 39 inclusions were detected but this time they were classified in different inclusion types as compared with what was observed after Step 2 analysis. A comparison of the results obtained by Step 2 and Step 5 for the number of

inclusions is shown in Figure 3.5. With the default classification rules, the detected inclusions were mainly classified into MnS (23%), Al_2O_3 (59%), Al_2O_3–MnS (15%), and minor amounts of spinel inclusions (see Figure 3.5a), whereas, after updating the classification rules, the number of Al_2O_3, Al_2O_3–MnS, and MnS inclusions significantly changed, as they were distributed into new inclusions classes (see Figure 3.5(b)) depending on their chemical composition in accordance with the classification rules shown in Table 3.1. According to Step 2 ASPEX analysis, which could not detect O and N, any feature containing Al above a specific value would be classified as Al_2O_3. However, with the updated classification rules and analysis method, it was possible to differentiate between Al_2O_3 and AlN. That is why a lower number of $Al_2O_{3(pure)}$ is shown in Figure 3.5(b).

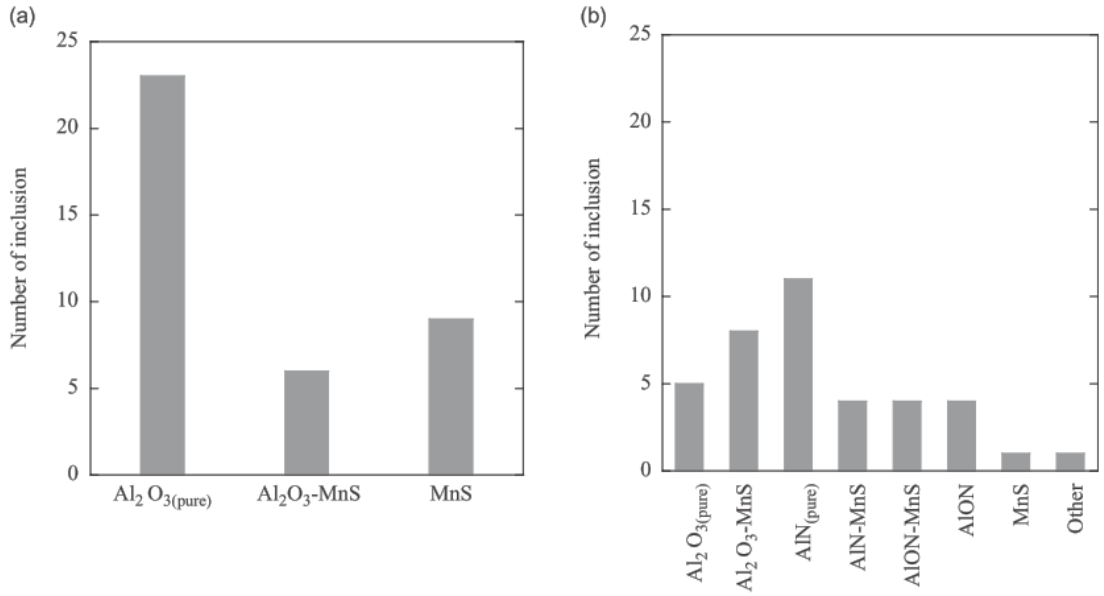

Figure 3. 5 The number of inclusions detected in 5% Mn steel sample using (a) the default classification rules (Step 2) and (b) the new classification rules (Step 5).

3.3 Results

3.3.1 Chemical Composition of Steel

It was observed that the chemical composition of steel did not vary during an experiment; therefore, an average composition of quartz tube samples taken at different holding times of a respective experiment is presented in this study. Table 3.2 shows the average composition values for all three experiments. It should be noted that the sulfur concentration increased with an increase in manganese concentration. The source of sulfur is the electrolytic manganese used in this study, which contains ≈300 ppm of sulfur content. Moreover, 2033 steel has a relatively higher nitrogen content (11 ppm) as compared with the other two steels.

Table 3. 2 Chemical composition of steel samples from all experiments (in %)

Steel Type	Mn	Al	Si	C	S	N	O
233	2.03	3.00	3.06	0.12	0.0018	0.0004	0.0019
533	5.10	2.88	3.02	0.12	0.0026	0.0006	0.0027
2033	20.66	2.82	3.50	0.12	0.0068	0.0011	0.0007

3.3.2 Morphology of Inclusions

The typical morphology of each type of inclusion is shown in Figure 3.6. $Al_2O_{3(pure)}$ inclusion is mostly observed in a globular or irregular shape with a smooth edge (Figure 3.6(a)). Al_2O_3–MnS inclusion has an irregular shape, and MnS is present mainly along the boundary of Al_2O_3 (Figure 3.6(b)), whereas, $AlN_{(pure)}$ inclusions have polygonal morphologies, such as hexagonal shape (Figure 3.6(c)) or rectangular shape. In the case of AlN–MnS inclusions, the morphology is irregular with MnS mostly covering along the perimeter of AlN particle (Figure 3.6(d)), or sometimes AlN is on the edge of MnS. AlON and AlON–MnS inclusions exhibit irregular morphologies (Figure 3.6(e),(f)). In these types of inclusions, the AlN part is polygonal, the Al_2O_3 part is globular or has a smoother edge, and MnS is surrounding AlN and Al_2O_3. Furthermore, MnS inclusions form different morphologies such as faceted (Figure 3.6(g)), globular, or elongated shape.

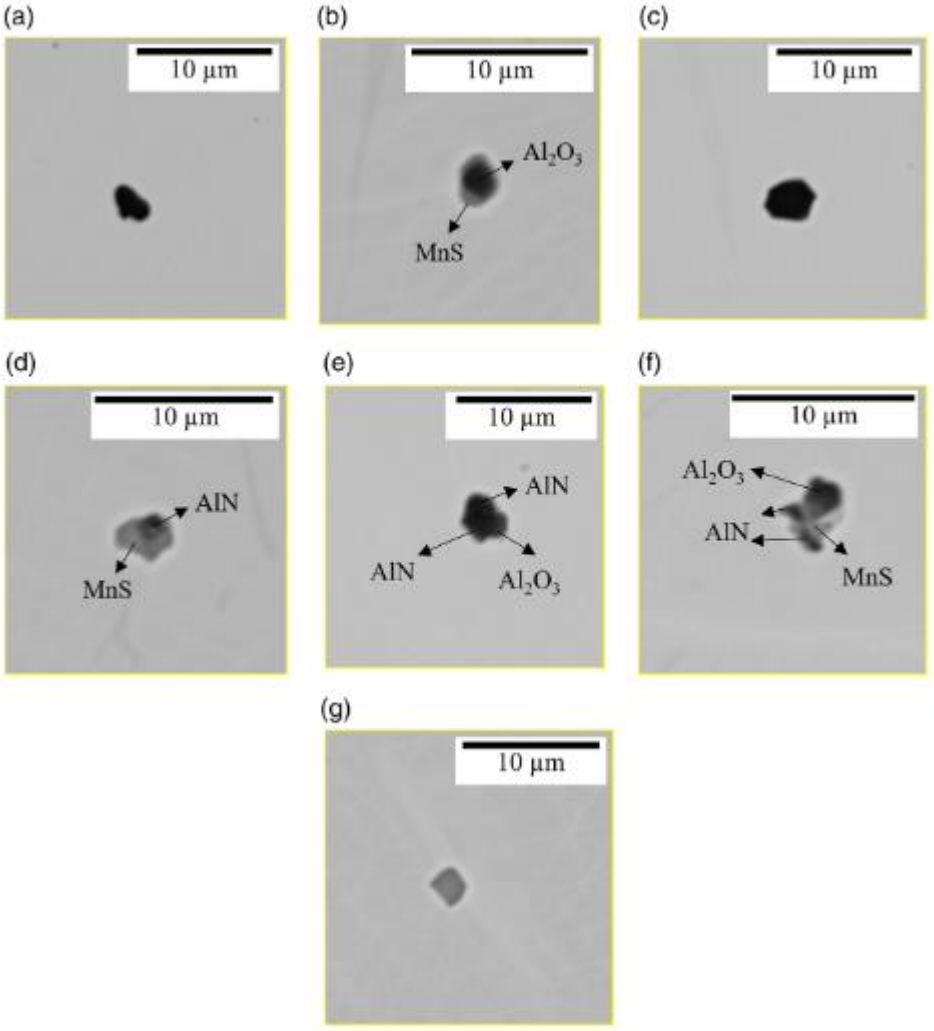

Figure 3. 6 Morphology of inclusions in Fe–Mn–Al steels, (a) $Al_2O_{3(pure)}$, (b) Al_2O_3–MnS, (c) $AlN_{(pure)}$, (d) AlN–MnS, (e) AlON, (f) AlON–MnS, and (g) MnS.

Due to the presence of various morphologies of MnS inclusions, the influence of steel chemistry on the characteristics of MnS inclusions is quantified by considering their shape factors, i.e., aspect ratio (AR) and circularity factor (CF). The AR is defined as the ratio of the maximum diameter to the minimum diameter of inclusion. The CF is calculated by Equation 3.1.

$$\text{Circularity Factor (CF)} = \frac{4\pi \times \text{Area of inclusion}}{\text{Perimeter}^2} \tag{3.1}$$

Figure 3.7 shows the AR and CF values of MnS inclusions in all three different steels. The results in Figure 3.7 show average values obtained from the analysis of MnS inclusions detected in 4 and 41 min holding time samples. It is shown that AR of MnS in 533 is the highest among the three steel types (AR = 13.1), whereas CF is the lowest, i.e., 0.23. This

suggests that MnS inclusions present in 533 samples are relatively elongated as compared with those in 233 and 2033.

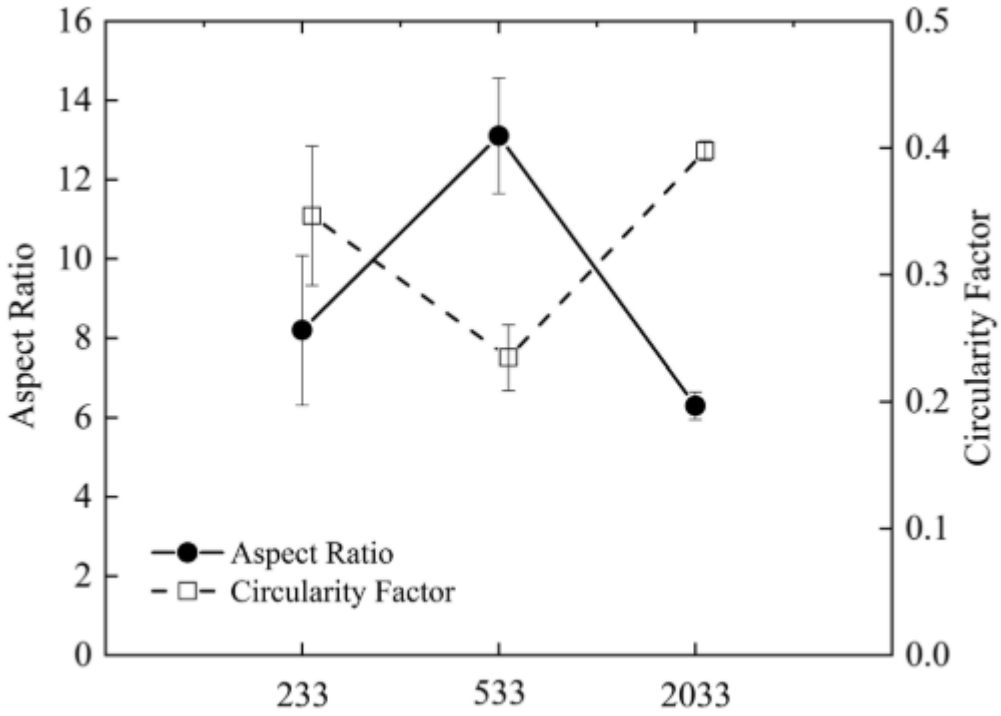

Figure 3. 7 The AR and CF values of the MnS inclusions present in 233, 533, and 2033 steel samples.

Further, to investigate the influence of steel chemistry on dual-phase inclusions, image analysis was conducted on several inclusions which involve measurement of the area of different phases present in dual-phase inclusions. This was mainly done for dual-phase Al_2O_3–MnS and AlN–MnS inclusions. Moreover, images of $Al_2O_{3(pure)}$, $AlN_{(pure)}$ were also analyzed. AlON and AlON–MnS were not considered due to difficulty in differentiating the Al_2O_3 phase from the AlN phase on an SEM image. The area of different phases was quantified using ImageJ 1.44p, Java 1.6.0_20 (32 bit). In this analysis, the SEM image is converted to a binary image. Then the threshold is adjusted manually to measure the area of different regions of the complex inclusions. In Figure 3.8, the back-scattered electron image of an AlN–MnS inclusion and a visual representation of area measurement of this particular inclusion is shown. This analysis was conducted for 12–35 inclusions from the aforementioned classes in samples from all three steel compositions, and average values are used for better presentation.

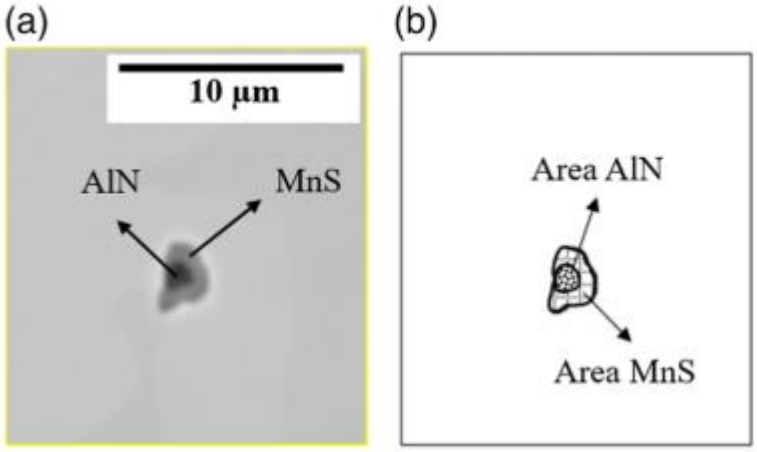

Figure 3. 8 (a) Back-scattered image of AlN-MnS and (b) the visual representation of different areas of AlN-MnS inclusion.

A comparison of the area of single-phase and dual-phase inclusions is shown in Figure 3.9. Figure 3.9(a) compares the area of $AlN_{(pure)}$ and AlN–MnS, where areas of individual phases (AlN and MnS) present in AlN–MnS inclusion are also given. A similar comparison between the area of $Al_2O_{3(pure)}$ and Al_2O_3–MnS is shown in Figure 3.9(b). In Figure 3.9(a), it is shown that the area of $AlN_{(pure)}$ inclusion in 233 steel is higher than that in 533 steel. Moreover, for both these steels, it is observed that the area of $AlN_{(pure)}$ inclusions is smaller than the area of AlN–MnS inclusions. This tendency could not be confirmed for 2033 steel due to a lack of $AlN_{(pure)}$ inclusions. Further, the area of AlN–MnS inclusions is significantly large for 2033 (≈5.4 μm^2) as compared with that of AlN–MnS inclusions in 233 and 533 samples (≈3.5 μm^2). Similarly, Al_2O_3–MnS inclusions present in 2033 samples have a larger area (≈1.9 μm^2, 19% larger) as compared with that of 533 samples. Furthermore, the area of $Al_2O_{3(pure)}$ is prominent than the area of the Al_2O_3 phase in Al_2O_3–MnS inclusion. Also, the area of $Al_2O_{3(pure)}$ inclusions of 533 steel is relatively larger than that of 233 steel.

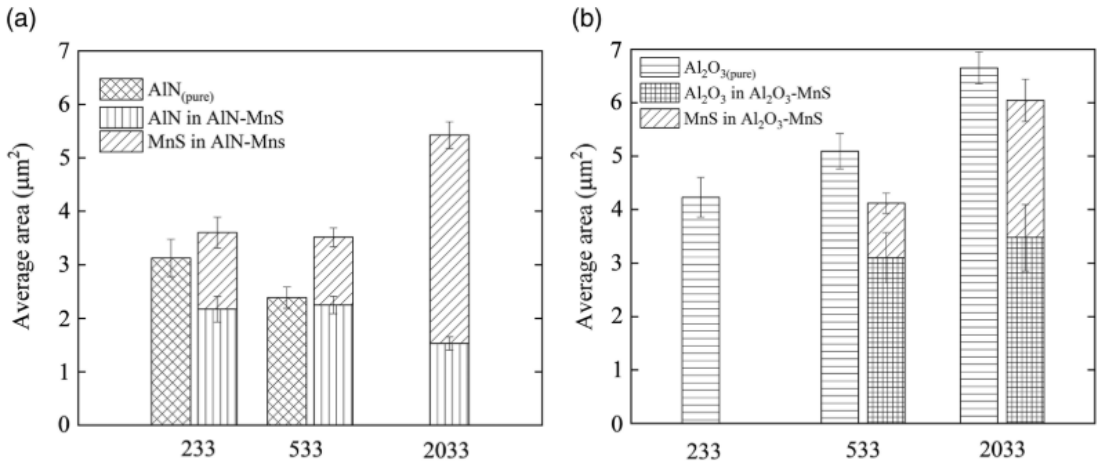

Figure 3. 9 Comparison of the area of (a) $AlN_{(pure)}$ and AlN-MnS inclusions and (b) $Al_2O_{3(pure)}$ and Al_2O_3-MnS inclusions present in 233, 533, and 2033 steels.

3.3.3 Inclusion Density and Composition

A comparison of the total number per unit area, N_A, of inclusions as a function of holding time for all experiments is shown in Figure 3.10. It is shown that the total N_A of inclusions increases with an increase in the manganese content of liquid steel. The N_A value for 233 steel lies between 7 and 16 mm^{-2}. For 533 steel, this value increased to a range of 7–30 mm^{-2}. A significant increase in the number of inclusions is shown for 2033 steel, where N_A lies between 50 and 70 mm^{-2}. An increase in the N_A of inclusions can be observed for samples taken at 2 min after the addition of Al_2O_3 particles. The N_A values reach a maximum at 4 min after the Al_2O_3 addition. It is followed by a decrease in the N_A values, which become constant in samples taken at 11 min after the Al_2O_3 addition.

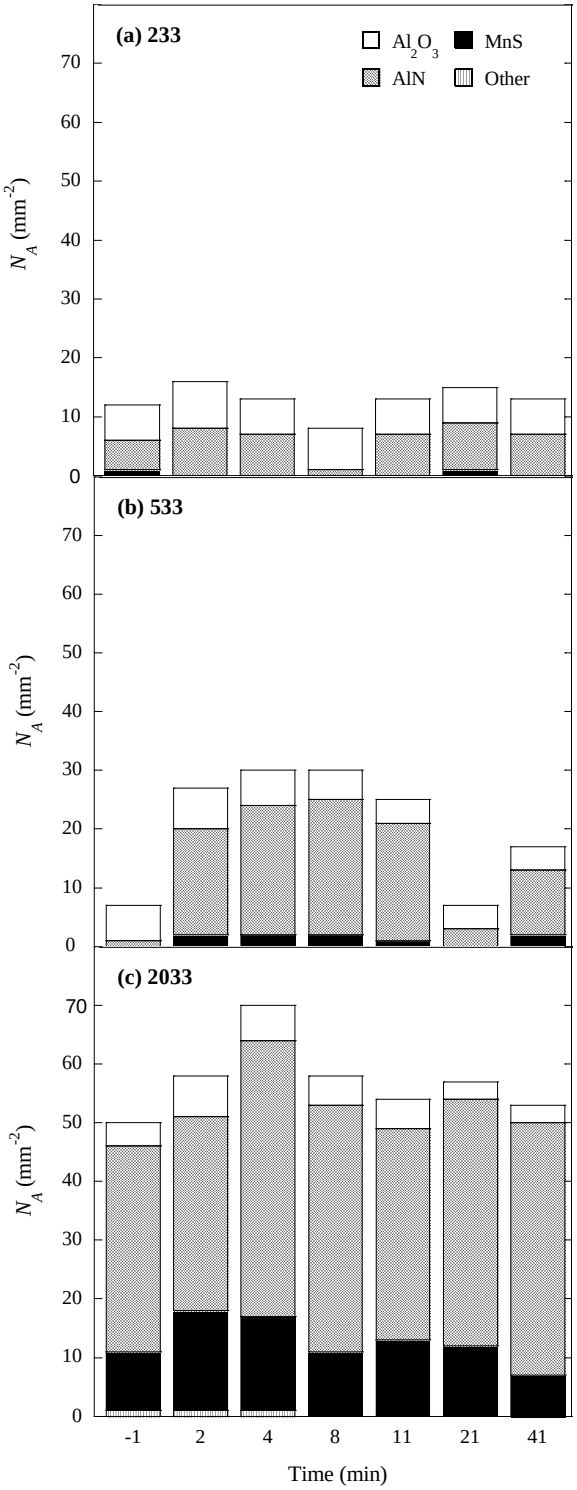

Figure 3. 10 Comparison of total number per unit area, N_A, of inclusions as a function of inclusion classes and holding time in (a) 233, (b) 533, and (c) 2033 steels.

Figure 3.10 also compares the N_A of the different types of inclusions. For 233 steel (Figure 3.10(a)), the N_A value of Al_2O_3 is between 6 and 8 mm^{-2} throughout the experiment, whereas 533 and 2033 steel samples contain a relatively lower amount of Al_2O_3 inclusions as compared with that in 233 samples, i.e., between 3 and 7 mm^{-2}. A significant difference in the N_A of AlN inclusions can be seen in the three experiments. The 233 steel samples contain 1–8 mm^{-2} AlN inclusions. The N_A of these inclusions increases to 1–23 mm^{-2} for 533 samples, which counts for 6–67% of total inclusions. Around 53–75% of inclusions observed for 2033 samples (i.e., N_A = 33–47 mm^{-2}) are AlN inclusions. Like AlN inclusions, the N_A of MnS inclusions is also increased by increasing the Mn content of the steel. The 233 steel samples contain ≈1 mm^{-2} of MnS inclusions, whereas, this is relatively higher for the case of 533 (1–2 mm^{-2}) steel. The N_A of MnS inclusions drastically increased to 7–19 mm^{-2} for 2033 steel. Moreover, all the samples from three experiments contain a negligible amount of "other" type of inclusions (less than 2% of the total number of inclusions).

3.4 Discussion

3.4.1 Effect of Manganese on the Morphology of MnS Inclusions

Figure 3.7 shows that despite having the highest Mn content, MnS inclusions in 2033 steel samples have the lowest AR and the highest CF values among all three experimental steel compositions. This phenomenon can be justified by considering the different morphologies of MnS inclusions. Based on the classification by Sims and Dahle,[19] the morphology of MnS inclusions can be classified into three types, as shown in Figure 3.11(a), where Type 1 is globular, Type 2 is rod-like (elongated), and Type 3 is a faceted or angular shape. Figure 3.11(b) compares the fraction of different types of MnS morphologies observed in 4 and 41 min samples of all steel compositions. MnS morphology in 233 steel is dominated by Type 1 (≈60%) and Type 2 (≈40%). Whereas, almost 80% of MnS inclusions in 533 steel samples are Type 2, and the remaining are Type 1 and Type 3. In the case of 2033 samples, Type 3 and Type 2 MnS inclusions count for around ≈60% and ≈30%, respectively. A predominant fraction of Type 2 MnS inclusions in 533 samples and Type 3 in 2033 samples explains the tendencies of AR and CF values shown in Figure 3.7. Moreover, these results show that an increase in Mn content from 2% to 5%, significantly increases the fraction of rod-like MnS inclusions (Type 2). With further increase in Mn content (to 20%), the fraction of these Type 2 inclusions is replaced by an escalation in the fraction of Type 3 inclusions.

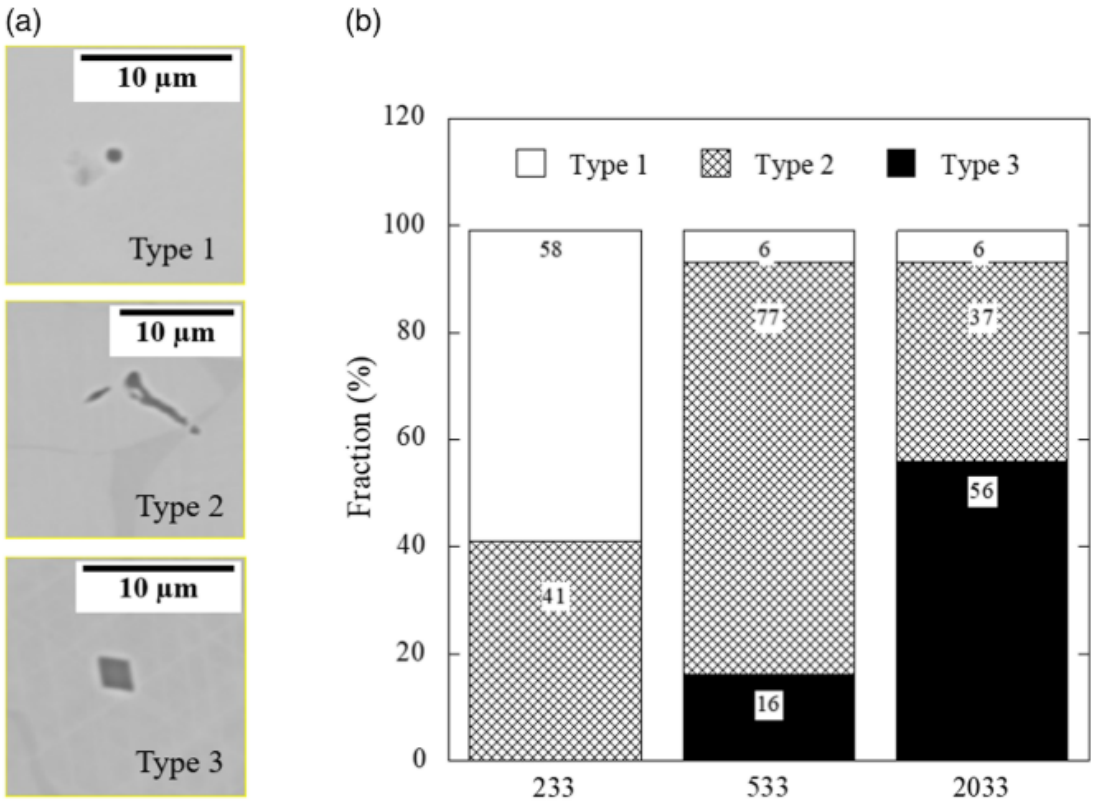

Figure 3. 11 (a) The typical morphology of MnS inclusion, Type 1: globular, Type 2: elongated, and Type 3: angular, and (b) the fraction of the morphology of MnS (Type 1, Type 2, and Type 3) in 233, 533, and 2033.

3.4.2 Effect of Manganese Content on the Inclusion Chemistry

The influence of the Mn content of steel on the composition of Al_2O_3 and AlN inclusions is shown in Figure 3.12(a),(b), respectively. As shown in Figure 3.12(a), the composition of Al_2O_3 inclusions changes from $Al_2O_{3(pure)}$ to Al_2O_3–MnS by increasing the Mn content in the steel. Notably, for the case of 233 steel samples, the $Al_2O_{3(pure)}$ subclass is dominant (96–98%). As the manganese content increased to 5%, the fraction of Al_2O_3–MnS slightly increased, counting for 1–7.5% of Al_2O_3-type inclusions. A further increase in the Mn content to 20% resulted in a significant increase in the N_A of Al_2O_3–MnS (1–3 mm^{-2}), which makes up more than 25–52% of Al_2O_3-type inclusions in 2033 samples.

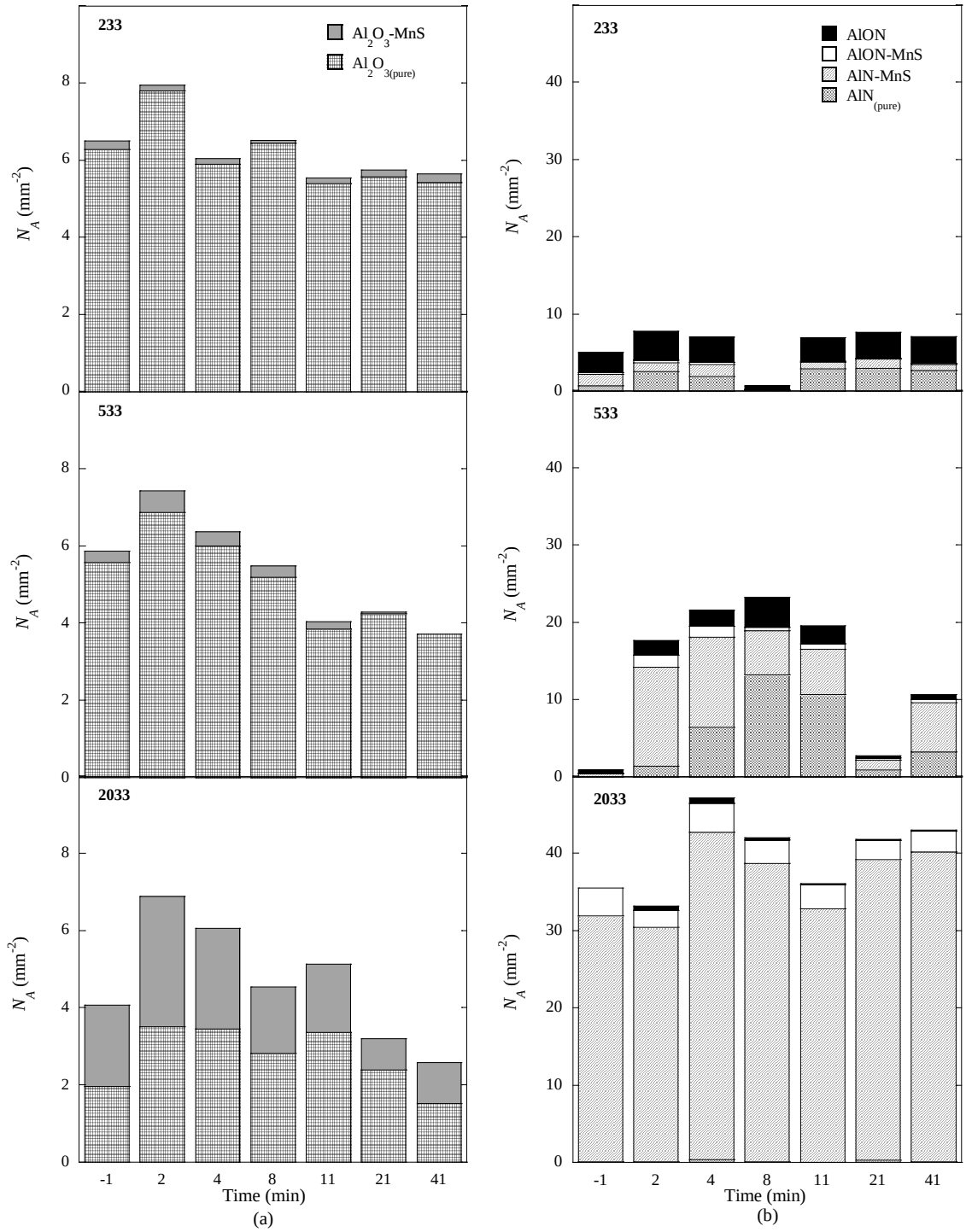

Figure 3. 12 A comparison of (a) Al_2O_3 and (b) AlN inclusion subclasses present in all three steels.

As mentioned earlier and shown in Figure 3.12(b), the total amount of AlN-type inclusions increased with increasing manganese content, which can be justified by the fact that the N solubility in molten steel increases as the manganese content in the steel increases.[102] This increase in N solubility reflected as the N content of steel has been observed in this study; i.e., the nitrogen content in the steel melt increased from 4 to 11 ppm as the manganese content increased from 2% to 20%. Therefore, a higher number of AlN-type inclusions are anticipated in 2033 steel samples. Moreover, it is also shown in Figure 3.12(b) that with increasing manganese content, the fraction of AlN–MnS and AlON–MnS inclusions increased at the expense of that of $AlN_{(pure)}$ and AlON inclusions. 233 steel mainly contains $AlN_{(pure)}$ inclusions (13–42%, N_A = 1–3 mm^{-2}) and AlON (N_A = 2–3 mm^{-2}) inclusions, and a small amount of AlN–MnS inclusions (N_A = ≈1 mm^{-2}). It also contains a negligible amount of AlON–MnS inclusions. As the manganese content increased to 5%, the fraction of MnS-containing AlN inclusions (i.e., AlN–MnS and AlON–MnS) increased to 30–81%. The amount of AlN–MnS and AlON–MnS varies from about 24% to 72% and 1% to 8%, respectively. For 2033 steel, AlN-type inclusions mainly consist of MnS-containing AlN subclasses (i.e., AlN–MnS and AlON–MnS). The fraction of AlN–MnS and AlON–MnS in 2033 samples is more than 97%, out of which 84–90% are AlN–MnS inclusions. Figure 3.12(a),(b) shows that an increased Mn content in steel leads to an increase in the MnS containing subclasses of Al_2O_3 and AlN inclusions. This indicates that MnS has coprecipitated with Al_2O_3 and AlN, especially when there is an abundance of Mn and S present in the molten steel (i.e., 2033 steel).

3.4.3 Formation of AlN Inclusions

The formation of AlN inclusions can be calculated thermodynamically using the following equations.[8,21,22]

$$[\mathrm{Al}] + [\mathrm{N}] = (\mathrm{AlN})_{(s)} \tag{3.2}$$

$$\Delta G^{\theta}_{\mathrm{AlN}} = -303500 + 134.6T_{steel}\ \mathrm{J/mol} \tag{3.3}$$

$$\log K_{\mathrm{AlN}} = \log\frac{a_{\mathrm{AlN}}}{h_{\mathrm{Al}}h_{\mathrm{N}}} = \log\frac{1}{f_{\mathrm{Al}}f_{\mathrm{N}}[\mathrm{wt\%\ Al}][\mathrm{wt\%\ N}]} \tag{3.4}$$

where $\Delta G^{\theta}_{\mathrm{AlN}}$ is the standard Gibbs free energy change of reaction (Equation 3.2), T_{steel} is the working temperature (1873 K, 1600 °C), and K_{AlN} is the equilibrium constant of the reaction. h_{Al} and h_{N} are the Henrian activities of Al and N, respectively. In this case, the activity of AlN is assumed to be unity as pure solid AlN is the standard state. f_{Al} and f_{N} are the activity coefficients of Al and N, respectively, which can be calculated using Equation 3.5.

$$\log f_{\mathrm{i}} = \sum\left[e_i^j(\%j)\right], (i = \mathrm{Al, N; j = C, Si, Mn, S, N, O, Al}) \tag{3.5}$$

The first-order interaction coefficients of each element, e_i^j, at 1873 K (1600 °C) used in this study are shown in Table 3.3.[9,20,22-26]

Table 3. 3 First-order interaction parameters, e_i^j, at 1873 K (1600°C).[9,20,22-26]

i	j						
	Al	C	Mn	Si	O	N	S
Al	0.043	0.091	0	0.0056	-1.979	0.0322	0.03
N	0.017	0.13	-0.023	0.047	-	-	0.007

Figure 3.13 shows the stability diagram for AlN inclusions in different types (233, 533, and 2033) of steel at 1873 K. In addition, the liquidus (T_{liq}) and solidus (T_{sol}) temperatures for each steel composition are calculated using FactSage 7.3 (FSstel, FToxid, and FactPS databases). Figure 3.13 shows that AlN is not a stable phase at 1873 K for all three steel compositions. Moreover, aluminum and nitrogen contents of 233 and 533 steels are even below the T_{liq} line, suggesting that AlN cannot form in liquid steel for both 233 and 533 steels. However, for 2033 steel, the composition lies just above the T_{liq} line. It means that AlN inclusions in 2033 steel can be formed in liquid steel during cooling from 1873 K. Nevertheless, AlN is not stable at 1873 K but AlN inclusions were observed in the quartz samples taken at 1873 K for all three experiments. The presence of AlN in steel samples can be understood by considering the formation of AlN during cooling and solidification.

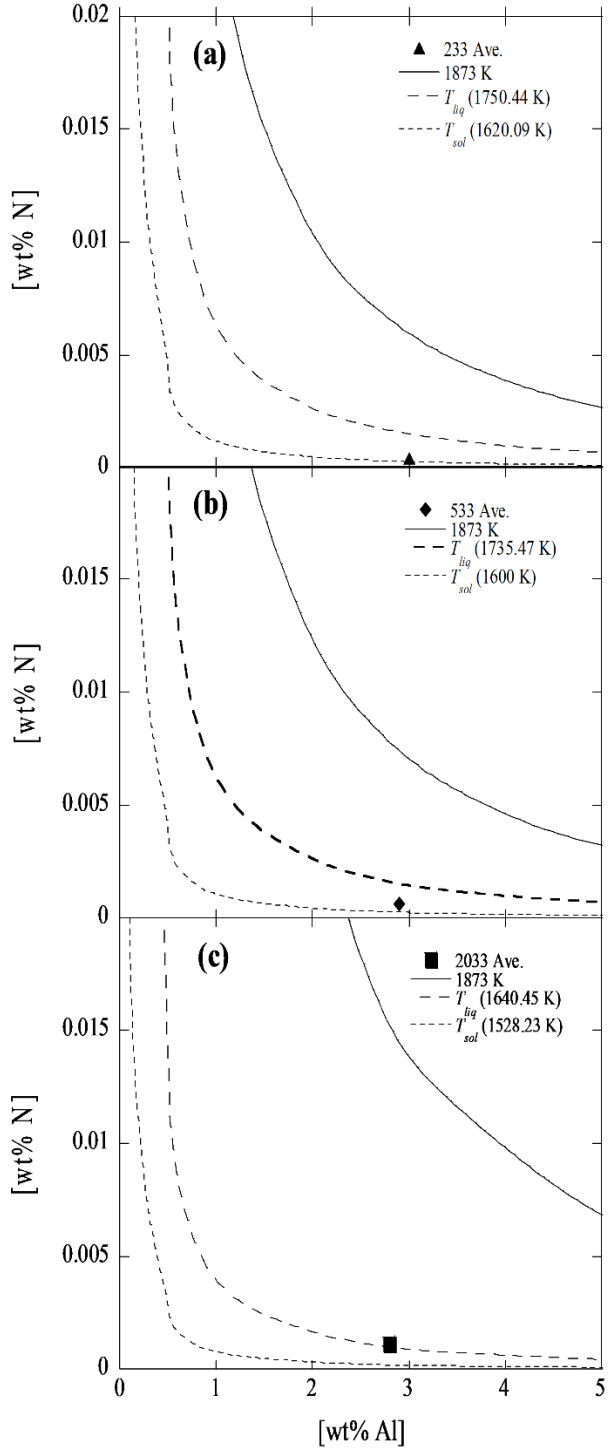

Figure 3. 13 AlN stability diagram for (a) 233, (b) 533, and (c) 2033 steels.

During solidification, the driving force for the formation of AlN increases due to the enrichment of Al and N at the solidification front. The concentration of [%Al] and [%N] in the liquid phase at the solidifying front and solid fraction (g_s) can be calculated using the Scheil equation.[15,18,20] The equations for [%Al] and [%N] are given in Equation 3.6 and 3.7.

$$[\%\mathrm{Al}] = [\%\ \mathrm{Al}]_0 (1 - \mathrm{g_s})^{(k_{\mathrm{Al}} - 1)} \tag{3.6}$$

$$[\%\mathrm{N}] = \frac{[\%\ \mathrm{N}]_0}{k_{\mathrm{N}} + (1 - k_{\mathrm{N}})(1 - \mathrm{g_s})} \tag{3.7}$$

where $[\%\mathrm{Al}]_0$ and $[\%\mathrm{N}]_0$ are the initial weight percentages of solute Al and N in liquid steel, respectively. k_{Al} and k_{N} are the equilibrium partition ratios of solute Al (0.6) and N (0.27), respectively.[20,27] K_{AlN} can be calculated using Equation 3.8.[22]

$$K_{\mathrm{AlN}} = 10^{-\frac{15850.93}{T_{steel}} + 7.0297} \tag{3.8}$$

Using Equation 3.6 and 3.7, the solid fraction ($\mathrm{g_s}$) for AlN precipitation in 233, 533, and 2033 steels is calculated to be 0.574, 0.422, and 0, respectively, where a $\mathrm{g_s}$ value of zero for 2033 means that AlN can start to form in liquid steel. From the results mentioned earlier, it can be inferred that the AlN inclusions observed in all steel samples are formed during the cooling and solidification of molten steel. Moreover, the decreasing trend of $\mathrm{g_s}$ value with increased Mn content suggests that AlN inclusion formation started earlier for 533 and 2033 steel samples as compared with 233 steel. Therefore, a higher number of AlN inclusions is expected for those steels.

3.4.4 Formation of MnS-Containing Multiphase Inclusions

It is worthy to restate that a higher fraction of MnS-containing AlN subclasses (i.e., AlN–MnS and AlON–MnS) are observed for increased Mn content of steel; especially the AlN–MnS subclass became dominant. The formation of AlN–MnS inclusions occurs by the coprecipitation of AlN and MnS. It is reported that this coprecipitation is facilitated by similar lattice parameters (or a low-lattice misfit) of AlN and MnS.[10,28] This means that it is feasible for AlN and MnS to precipitate on each other. The available literature reports both possible scenarios for AlN and MnS coprecipitation—i.e., Scenario 1: heterogeneous nucleation of AlN on MnS inclusions and Scenario 2: AlN acting as a nucleation site for MnS. Tuling and Mintz[10] and Kang et al.[12] reported that MnS inclusions appear to act as nucleation sites for the precipitation of AlN. Lückl et al.[29] also investigated the coprecipitation of AlN and MnS and concluded that the coprecipitates were formed according to Scenario 1, i.e., AlN precipitated on existing MnS particles. However, the steel compositions investigated in the aforementioned studies contain less Al (1–1.5%), for which the AlN precipitation temperature could be lower than that of MnS.

Liu et al.[8] analyzed inclusions in twinning-induced plasticity steel samples containing 3% Al and 25% Mn. They observed AlN inclusions present in liquid steel using a confocal scanning laser microscope and suggested that AlN inclusions can act as a site for

heterogeneous nucleation of MnS (Scenario 2). Moreover, recently the current authors[15] have also shown MnS precipitation on AlN inclusions in steel samples (cooled at 10 °C min^{-1}) having compositions very similar to that of 233 and 533 steel in this study. This observation is supported by thermodynamic calculations that the AlN formation temperature (T_{AlN}) is higher than MnS precipitation temperature (T_{MnS}); hence, AlN forms first and acts as a MnS nucleation site. T_{AlN} and T_{MnS} values for the current experimental steels, obtained by FactSage 7.3, are shown in Table 3.4. The values suggest that AlN formation should occur before MnS precipitation for all three steel compositions, and the expected morphology of AlN–MnS is a duplex inclusion having AlN present in the core surrounded by MnS. However, in addition to the expected morphology, the existence of an AlN particle attached to an MnS particle is also observed, as shown in Figure 3.14. This indicates that AlN and MnS coprecipitation took place according to both possible scenarios. The contradiction to the authors' previous report[15] is due to the difference in the cooling rates adopted in both studies. In the previous study, the samples were cooled at a rate of 10 °C min^{-1}, which enabled AlN inclusions to grow before MnS precipitation started, whereas in this study, the cooling rate of samples is estimated to be greater than 20 °C s^{-1}.[30] At such a high cooling rate, T_{AlN} and T_{MnS} would be somewhat inseparable, leading to precipitation of AlN and MnS at an almost similar time. Hence, a mixed/combined coprecipitation behavior can be expected. It is imperative to mention that AlN would act as nuclei for MnS precipitation in cases when AlN is formed in liquid steel, similar to that of Liu et al.[8]

Table 3. 4 AlN formation and MnS formation temperature of the studied steel compositions

Steel Type	T_{AlN} (K)	T_{MnS} (K)
233	1722.07	1455.8
533	1716.21	1457.01
2033	1678.02	1473.6

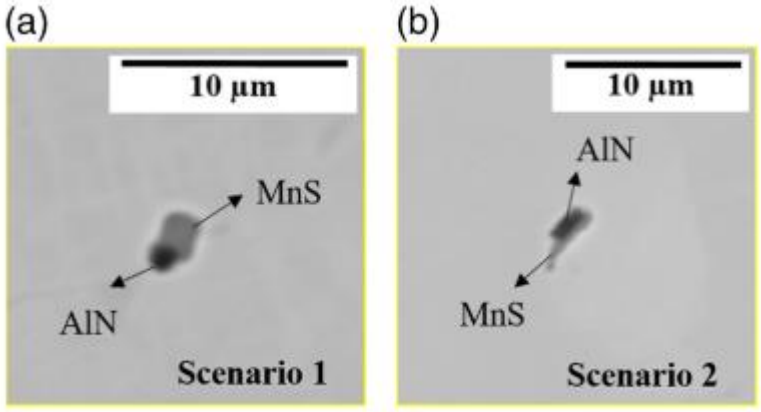

Figure 3. 14 Morphology of coprecipitates of AlN and MnS formed according to (a) Scenario 1 and (b) Scenario 2.

Occurrences of coprecipitation of Al_2O_3 and MnS are also observed in this study, especially for 2033 steel samples. Ohta and Suito[28] suggested that due to a high lattice misfit between Al_2O_3 and MnS particles, it is unlikely for MnS to precipitate on Al_2O_3 inclusions. However, it can be argued that this could happen during the solidification of high-Mn steels where there exists plenty of Mn and S in molten steel seeking sites for precipitation, particularly since Al_2O_3 inclusions can be pushed to the region of final solidification,[28] which is segregated with Mn and S.

3.4.5 Effect of MnS Precipitation on the Area of Inclusions

As shown in Figure 3.9, the coprecipitates of AlN and MnS (i.e., AlN–MnS inclusions) have a relatively larger area than the area of $AlN_{(pure)}$ inclusions. However, in the case of Al_2O_3 inclusions, the dual-phase inclusions (i.e., Al_2O_3–MnS inclusions) have a smaller area than that of $Al_2O_{3(pure)}$ inclusions. This everted tendency can be understood by considering the following: 1) a difference in the coprecipitation behavior of MnS with AlN and Al_2O_3; 2) the morphology of coprecipitates; and 3) influence of MnS precipitation on the growth rate of AlN and Al_2O_3.

As mentioned in Section 3.4.4, AlN and MnS coprecipitation occurs either by precipitation of AlN on MnS (Scenario 1) or vice versa (Scenario 2). In the former case, MnS has irregular morphology and has a larger size/area as compared with that of MnS precipitated on AlN (see Figure 3.14a). Whereas, in the latter case (see Figure 3.14b), MnS is present around the periphery of the polygonal AlN phase. However, in many cases, it protrudes to one side and grows. Thereby, the area of AlN–MnS is larger as compared with the area of $AlN_{(pure)}$ inclusions.

In the case of coprecipitation of Al_2O_3 and MnS, MnS precipitates on the existing Al_2O_3 particles. Mostly MnS wraps around Al_2O_3 particles while maintaining their shape and adding an even thickness to them (see Figure 3.6(b)). A presence of the MnS layer

would inhibit the growth of the Al_2O_3 phase in Al_2O_3–MnS inclusions, whereas $Al_2O_{3(pure)}$ inclusions would grow to larger sizes. A similar effect of the presence of MnS on the growth of AlN is observed for AlN–MnS inclusions, where the area of AlN phase in AlN–MnS is smaller than that of $AlN_{(pure)}$. However, the overall area of AlN–MnS inclusions become more substantial than the area of $AlN_{(pure)}$ due to irregular morphology and larger size/area of MnS present in AlN–MnS formed by Scenario 1, and protruding MnS phase in AlN–MnS formed by Scenario 2.

A larger area of AlN–MnS and Al_2O_3–MnS inclusions for 2033 as compared with those in other steels is due to its significantly high Mn and S contents. Figure 3.9 also shows some tendencies regarding the influence of steel composition on the area of $AlN_{(pure)}$ and $Al_2O_{3(pure)}$ inclusions. Further investigations are required to develop an understanding of those results.

3.5 Conclusions

The effect of manganese on the inclusion formation in light-weight Fe–Mn–Al steels is investigated by conducting laboratory experiments. The characteristics of inclusions are observed in three dimensions using an electrolytic extraction method and two dimensions on a polished cross-section by SEM. Moreover, an automated SEM analysis (ASPEX) is also used. The following can be concluded from the obtained results. A systematic inclusion analysis has been conducted to develop inclusion classification rules for an automated inclusion analysis (ASPEX) system to enable detection of AlN containing inclusions. Based upon that, ASPEX has been successfully used for analyzing inclusions in steels containing high Al (3%) and Mn (2–20%) contents. The inclusions observed in light-weight Fe–Mn–Al steels can be classified as $Al_2O_{3(pure)}$, Al_2O_3–MnS, $AlN_{(pure)}$, AlN–MnS, AlON–MnS, AlON, and MnS. Moreover, increasing the manganese content from 2% to 20% increases the total amount of inclusions by 4–8 times. Mainly, this increase is in the number of AlN and MnS inclusions. Furthermore, the AR of MnS inclusions increases (from 8 to 13) by increasing the Mn content of steel from 2% to 5%, and then it decreases with an increase in the Mn content to 20%. However, the decrease in AR is associated with a substantial rise in the MnS amount. For all three steel compositions, the AlN-containing inclusions formed during cooling and solidification due to their low nitrogen content. The inclusion analysis indicates that both AlN and Al_2O_3 inclusions can serve as a site for heterogeneous nucleation of MnS. Moreover, MnS inclusions can also be nuclei for the precipitation of AlN.

3.6 Acknowledgements

The authors would like to express gratitude to the Natural Sciences and Engineering Research Council of Canada (project no: 20002139) for the financial support for this work. Further, the authors thank Dr. Stanley Sun and Ms. Li Sun at ArcelorMittal Dofasco for their valuable time and fruitful discussions. The authors also acknowledge the Canadian Centre for Electron Microscopy (CCEM) at McMaster University for assistance with SEM analysis.

3.7 References

1. E. Billur, J. Dykeman, T. Altan, Stamp. J. 2014, Jan/Feb, 1.
2. A. S. Hamada, L. P. Karjalainen, Mater. Sci. Eng. A 2011, 528, 1819.
3. D. Z. Li, Y. H. Wei, B. S. Xu, L. F. Hou, P. D. Han, Ironmaking Steelmaking 2011, 38, 540.
4. R. Vaz Penna, L. N. Bartlett, T. Constance, Int. J. Meter. 2019, 13, 286.
5. J. H. Park, D. J. Kim, D. J. Min, Metall. Mater. Trans. A 2012, 43, 2316.
6. C. Zhuang, J. Liu, Z. Mi, H. Jiang, D. Tang, G. Wang, Steel Res. Int. 2014, 85, 1432.
7. G. Gigacher, W. Krieger, P. R. Scheller, C. Thomser, Steel Res. Int. 2005, 76, 644.
8. H. Liu, J. Liu, S. K. Michelic, S. Shen, X. Su, B. Wu, H. Ding, Steel Res. Int. 2016, 87,1.
9. M.-K. Paek, J.-M. Jang, K.-H. Do, J.-J. Pak, Met. Mater. Int. 2013, 19, 1077.
10. A. Tuling, B. Mintz, Mater. Sci. Technol. 2016, 32, 568.
11. N. Ånmark, A. Karasev, P. Jönsson, Materials 2015, 8, 751.
12. S. E. Kang, J. R. Banerjee, A. Tuling, B. Mintz, Mater. Sci. Technol. 2014, 30, 1328.
13. G. D. Funnell, R. J. Davies, Met. Technol. 1978, 5, 150.
14. M. Nabeel, M. Alba, S. Sun, A. Karasev, P. Jonsson, in AISTech 2018 Iron and Steel Technology Conf. and Exposition, 7 May 2018 through 10 May 2018, Association for Iron and Steel Technology, AISTech, Philadelphia 2018, pp. 1483–1491.
15. M. Nabeel, M. Alba, A. Karasev, P. G. Jönsson, N. Dogan, Metall. Mater. Trans. B 2019, 50, 1674.
16. N. Dogan, B. J. Monaghan, R. J. Longbottom, M. H. Reid, in 4th Annual High Temperature Processing Symp., Swinburne University of Technology, Melbourne, Australia 2012, p. 63.
17. N. Dogan, B. J. Monaghan, R. J. Longbottom, M. H. Reid, in Scanmet IV: 4th Int. Conf. on Process Development in Iron and Steelmaking, Swerea MEFOS, Luleå, Sweden 2012,p.1.
18. H. Liu, J. Liu, S. Michelic, F. Wei, C. Zhuang, Z. Han, S. Li, Ironmaking Steelmaking 2016, 43, 171.
19. C. E. Sims, F. B. Dahle, Trans. Am. Foundrym. Soc. 1938, 46, 65.
20. M. Paek, J. Jang, M. Jiang, J. Pak, ISIJ Int. 2013, 53, 973.
21. J.-M. Jang, M.-K. Paek, J.-J. Pak, ISIJ Int. 2017, 57, 1821.
22. M.-K. Paek, J.-M. Jang, H.-J. Kang, J.-J. Pak, ISIJ Int. 2013, 53, 535.
23. JSPS, Steelmaking Data Sourcebook, Revised, Gordon and Breach Science Publications, Montreux 1988.

24. G. K. Sigworth, J. F. Elliot, Met. Sci. 1974, 8, 298.
25. H. Itoh, M. Hino, S. Ban-Ya, Tetsu-to-Hagane 1997, 83, 773.
26. D. H. Kim, M. S. Jung, H. Nam, M. K. Paek, J. J. Pak, Metall. Mater. Trans. B 2012, 43, 1106.
27. E. T. Turkdogan, Fundamentals of Steelmaking, The Institute of Materials, London 1996.
28. H. Ohta, H. Suito, ISIJ Int. 2006, 46, 480.
29. M. Lückl, T. Wojcik, E. Povoden-Karadeniz, S. Zamberger, E. Kozeschnik, Steel Res. Int. 2018, 89,1.
30. O. T. Ericsson, M. Lionet, A. V. Karasev, R. Inoue, P. G. Jönsson, Ironmaking Steelmaking 2011, 39, 67.

Chapter 4

Effect of Aluminium Content on the Formation of Inclusions in Fe-5Mn-xAl Steels

Chapter 4 is a pre-publication version of the article published in Ironmaking and Steelmaking 2020, DOI: 10.1080/03019233.2020.1791549. The following chapter discussed the effects of aluminum content (0.5, 1, 3, and 6%) on the characterization of inclusions in the laboratory produced Fe-5Mn-xAl steels. In this investigation, the automatic scanning electron microscope (SEM) equipped with the ASPEX feature was used to detect and analyze the inclusions. The inclusion classification rules provided in Chapter 3 were applied in this chapter. It was found that as the Al content increased, the total amount of inclusions also increased. The types of detected inclusions were $Al_2O_{3(pure)}$, Al_2O_3-MnS, $AlN_{(pure)}$, AlN-MnS, AlON, AlON-MnS, and MnS. The thermodynamic calculations were conducted to study the formation mechanism of the AlN-containing inclusions. It was concluded that AlN inclusions were formed during the solidification of steel (except for 6% Al-containing steel) due to the low nitrogen content of the steel (<10 ppm). Moreover, MnS inclusions co-precipitate with Al_2O_3 or/and AlN inclusions, which act as the heterogeneous nucleation sites for MnS inclusion. The preference of MnS inclusion to co-precipitate together with Al_2O_3 or AlN was also investigated by calculating their precipitation ratio.

All the experiments, data collection, and analysis were completed by the primary author. Li Sun (ArcelorMittal Dofasco) provided training for using automated SEM (ASPEX). Dr. Muhammad Nabeel assisted with the mapping of the inclusions. The manuscript was written by the primary author. Dr. Muhammad Nabeel and Dr. Neslihan Dogan contributed to the discussion and proofread the manuscript.

Effect of Aluminium Content on the Formation of Inclusions in Fe-5Mn-xAl Steels

Michelia Alba,* Muhammad Nabeel, and Neslihan Dogan

Michelia Alba, Ph.D. Student, albam@mcmaster.ca
Department of Material Science and Engineering, McMaster University, 1280 Main Street West, Hamilton, ON L8S 4L7, Canada

Muhammad Nabeel, Postdoctoral Fellow,
Department of Material Science and Engineering, McMaster University, 1280 Main Street West, Hamilton, ON L8S 4L7, Canada

Neslihan Dogan, Assistant Professor,
Department of Material Science and Engineering, McMaster University, 1280 Main Street West, Hamilton, ON L8S 4L7, Canada

Abstract

The effect of Al content on the characteristics and formation of inclusions in the light-weight Fe–5Mn–xAl steels was investigated in this study. Four synthetic steels with different Al content were produced in the laboratory. The types of observed inclusions were $Al_2O_{3(pure)}$, Al_2O_3–MnS, $AlN_{(pure)}$, AlN–MnS, AlON–MnS, AlON, and MnS. Increasing Al content from 0.5% to 6% increased the total amount of inclusions by 2.5 times. As the Al content increased from 0.5% to 3%, the number of AlN–MnS inclusions increased significantly. Moreover, the $AlN_{(pure)}$ inclusions appeared 6% Al-containing steel. Thermodynamic calculations confirmed that AlN inclusions formed during the cooling of the steel. It is also observed that AlN can precipitate on Al_2O_3 to form AlN + Al_2O_3 inclusions, classified as multi-phase AlON inclusions in this study. Furthermore, MnS inclusions could co-precipitate with AlN and Al_2O_3 inclusions, but it preferred to co-precipitate with AlN inclusions.

4.1 Introduction

The development of Advanced High Strength Steel (AHSS) has reached the third generation.[1] The second generation of AHSS contains high manganese content (10–25%).

Its production has high cost[2] and faces difficulties.[1,3,4] Therefore, the development of AHSS with medium manganese content (3–10%) and varied aluminium content attracts the interest of steel industries.[4,5] The combination of high strength and light weight still remains the critical parameter for steel in automotive applications. Aluminium is one of the elements whose high content can make the steel lightweight,[6] since the addition of 1% of it can reduce the density of the steel by about 1.5%.[5,7] Nowadays, researchers have tried to produce Fe–Mn–Al steel with manganese content from 2% to 10% and aluminium content up to 9% in the laboratory.[3,5,8,9]

Although there are studies on the microstructure and mechanical properties of medium manganese steel,[3,5,8,9] research on inclusion formation in relatively high aluminium steels is still limited.[10] Conventional low Al-killed steels can contain complex inclusions; for instance, SiO_2–CaO–Al_2O_3 inclusions were observed in Al-killed steels with Al content <0.05%.[11] As the content of alloying elements increases in liquid steel, the formation of complex non-metallic inclusions cannot be avoided. Park et al.[10] observed that the types of inclusions formed in Fe–Mn–Al steels are Al_2O_3, AlN, $MnAl_2O_4$, Al_2O_3(–Al(O)N), Mn(S,Se), oxide core with MnS, and MnS with Al_2O_3(–Al(O)N). They also found that there is a change in the number of inclusions with increasing Al content from 1% to 6%. AlN inclusions increased from 8% to 10%, with increasing Al content from 3% to 6%. AlN–MnS inclusions first increased from 16% to 23%, with increasing Al content from 1% to 3%, and decreased to 20% at Al content 6%. Moreover, it was also observed that AlON inclusions increased two times with increasing Al content from 3% to 6%.

Owing to the similar lattice parameter, AlN inclusion can co-precipitate with MnS inclusion.[12] In the equilibrium condition, AlN can form first and become the nucleation site for MnS inclusion during solidification. However, in a non-equilibrium state, MnS inclusion can become the site for AlN inclusion to nucleate.[13] Besides AlN inclusion, Al_2O_3 inclusion can also be the nucleation site for MnS inclusion. Since Al_2O_3 inclusion is the stable inclusion in liquid steel, it will form first at steelmaking temperature and provide a nucleation site for MnS during cooling. All of these inclusions are detrimental to steel. AlN is harmful to the hot ductility of the steel[14] MnS is harmful to the toughness of the steel[15] and Al_2O_3 creates a clogging problem in steel processing.[16] So, it is essential to control the content of the reacting species such as N, S, and O to limit the volume fraction of the non-metallic inclusions.[17]

The current study investigates the effect of aluminium content on the characteristics of inclusions in Fe–5Mn–*x*Al steels. It is followed by the investigation for the co-precipitation of the detected inclusions. The thermodynamic calculations are also taken into account to discuss the formation of inclusions.

4.2 Experimental

Experiments were conducted using a resistance heating tube furnace, as shown in Figure 4.1.[18,19] The furnace chamber was evacuated before the experiment and was subsequently backfilled with high purity Ar gas (99.999%). Ar gas was passed through Ti turnings at 923

K to absorb any oxygen traces present in the gas. In each experiment, synthetic steel (500 gr), Fe–5Mn–(0.5–6)Al–3Si–0.1C, placed in an alumina crucible was heated to 1873 K (1600°C). After reaching the target temperature, the furnace chamber was once again evacuated and backfilled with argon gas. Immediately after this, the first sample (S1) was taken using a quartz tube, and it was defined as time zero for the experiment. Several samples were obtained at different holding times (0, 2, 4, 6, 8, 11, 21 and 41). The chemical analyses of steel samples were done by induction coupled plasma optical emission spectrometry (ICP-OES). The carbon–sulphur and oxygen–nitrogen contents of samples were measured by LECO C/S analyser and LECO O/N analyser.

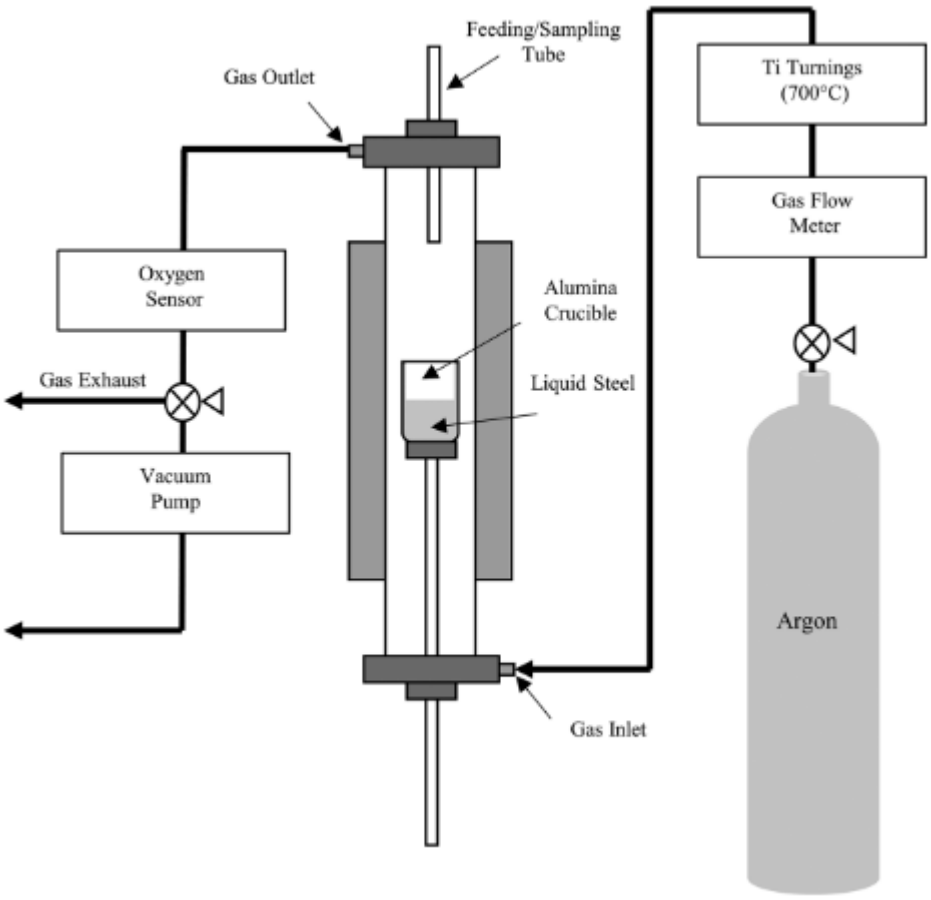

Figure 4. 1 Schematic diagram of the experimental set-up used in this study.[18,19]

The inclusion analysis was carried out by using the ASPEX inclusion analysis system and using the following parameters: magnification - 456x, accelerating voltage - 20 kV, emission current - 43.4 μA, and spot size - 35%. The analysed area and the number of observed inclusions varied from 15 to 50 mm and 180 to 880, respectively. In the current work, only the inclusions having a maximum diameter (D_{max}) > 2 μm were analysed, and they were calssified into different groups according to their chemical composition. The

details of experimental material and the inclusions classification rules are descrebed elsewhere.[20]

4.3 Results and Discussion

It was found that the chemical composition of steels did not vary during experiments. Hence, the average composition of pin samples taken at different holding times of each experiment is summarized in Table 4.1. The detected values for N and O contents were scattered and less than 10 ppm, which is close to the detection threshold. Further, it is expected to have ±2 ppm in the calibration of N and O analyses.

Table 4. 1 Chemical composition of steel samples for all experiments (in wt-%).

Steel type	Mn	Al	Si	C	S (ppm)	N (ppm)	O (ppm)
50.53	4.8	0.4	3.2	0.1	21.6	<10	<10
513	4.8	0.9	3.2	0.1	26	<10	<10
533	4.9	2.8	3.2	0.1	23.4	<10	<10
563	5.2	5.7	3.2	0.1	29.5	<10	<10

4.3.1 Inclusion Characteristics

The inclusions are classified into four major classes, i.e., Al_2O_3, AlN, MnS, and Other. The Al_2O_3 inclusions are further classified into two subclasses: $Al_2O_{3(pure)}$ and Al_2O_3-MnS. The AlN class consists of four subclasses, i.e., $AlN_{(pure)}$, AlN-MnS, AlON-MnS, and AlON. The 'Other' class contains complex oxide inclusions, which do not fall in the aforementioned classes. The details of the classification rules of inclusions were explained elsewhere.[20]

In the previous work of authors,[20] there were insignificant changes in the composition, size distribution, and the number of inclusions with time in an experiment. Therefore, the sample taken at 21 minutes holding time is selected for ease of presentation and to resemble the time needed for the refining process in the steel industry. The comparison of the total number per unit area (N_A) of inclusions in 21 minutes samples for each steel is depicted in Figure 4.2. The total number of inclusions increases with an increase in Al content in the steel. The N_A values in 50.53, 513, 533, and 563 samples are 12, 10, 23, and 29 mm^{-2}, respectively.

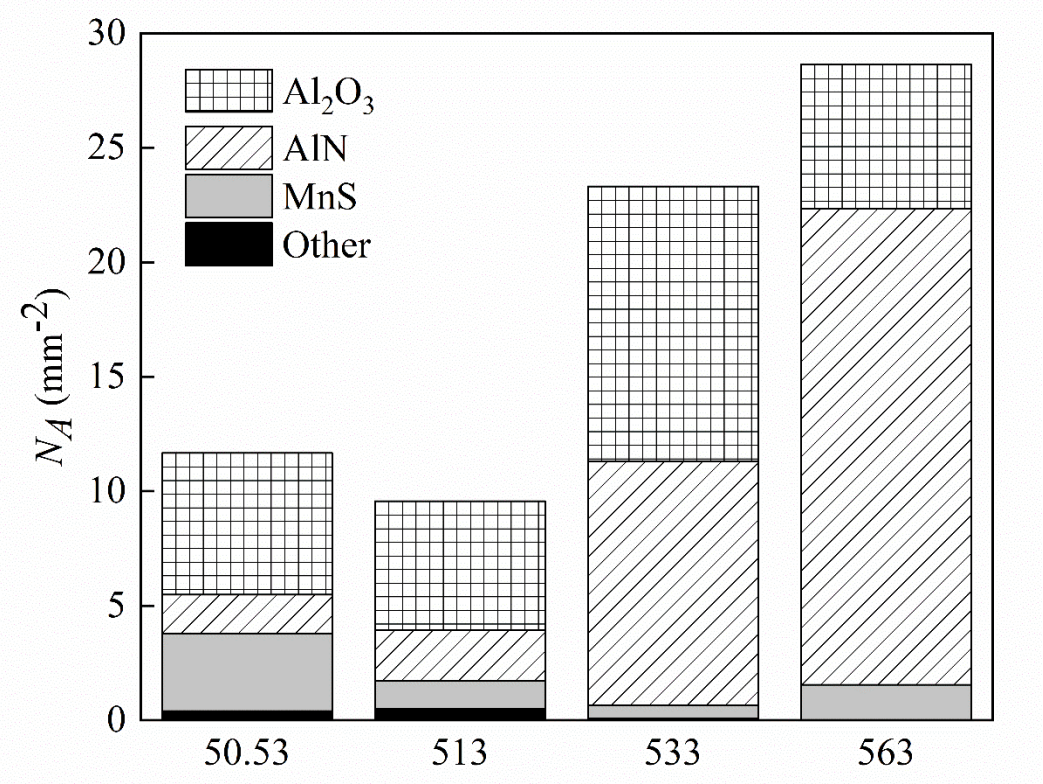

Figure 4. 2 Comparison of inclusion classes in 50.53, 513, 533, and 563 steel samples at the 21 minutes holding time.

Figure 4.2 also presents the number of inclusions for each major class of inclusions present in the experimental steels. It can be seen in Figure 4.2 that for both 50.53 and 513 steel samples, the number of Al_2O_3 (~6 mm^{-2}) and AlN (~2 mm^{-2}) inclusions are very similar. However, an increase of Al content to 3% results in ~12 mm^{-2} Al_2O_3, and a further increase in Al to 6% reduces the number of Al_2O_3 to ~6 mm−2. Similarly, a drastic increase in AlN inclusions is observed by increasing Al content. The number of AlN inclusions in 533 is ~11 mm^{-2}. When the Al content is increased to 6%, the number of AlN inclusions becomes almost twice as compared to 533 steel sample. The 'Other' inclusions count for only ~5% of the total number of inclusions; therefore, they are neglected for further analysis.

The distribution of Al_2O_3 and AlN in their subclasses is shown in Figure 4.3. It can be seen that there is no significant change in the chemistry of Al_2O_3 inclusions for all steel compositions. More than 80% of the Al_2O_3 inclusions are $Al_2O_{3(pure)}$ (Figure 4.3(a)). Whereas an increase in the Al content of steel has a pronounced influence on the composition of AlN inclusions (Figure 4.3b). AlN–MnS is the dominant subclass for 50.53 and 513 steel samples. As the Al content increased from 3% to 6%, the quantity of AlON and AlON–MnS increased counting for around 46% of the AlN inclusion class. The decrease in the amount of Al_2O_3 inclusions by increasing Al content from 3% to 6% is reflected as an increase in the fraction of AlON. This suggests that a part of Al_2O_3 inclusions transformed into AlON. In addition, a significant fraction of $AlN_{(pure)}$ (~30%) is

seen in the 563 steel sample. The formation of different subclasses of AlN inclusions is discussed later.

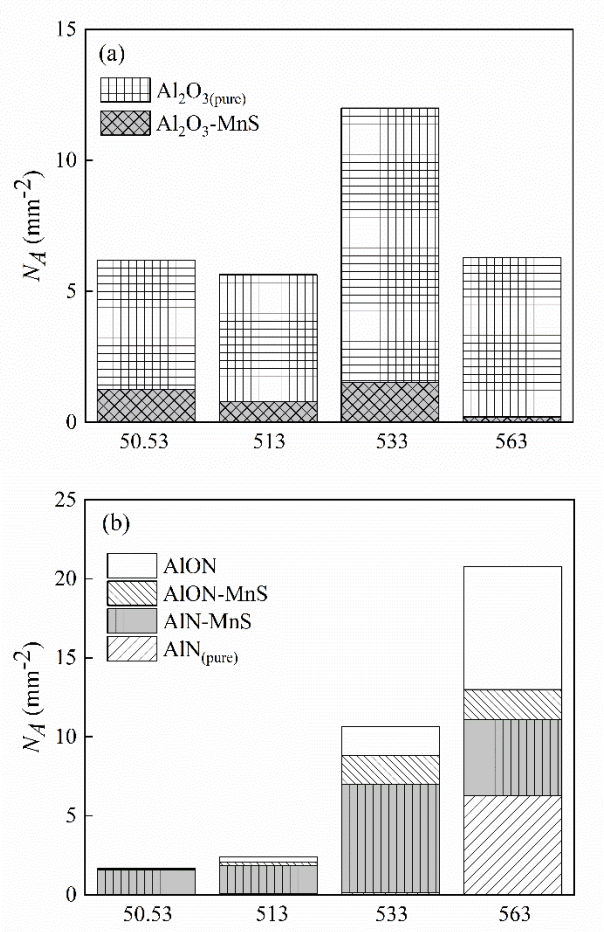

Figure 4. 3 (a) A comparison of Al_2O_3 inclusion subclasses and (b) AlN inclusion subclasses for 50.53, 513, 533, and 563 steel samples.

4.3.2 Formation of AlN inclusions

The reaction equilibrium for the formation of AlN inclusions in liquid steel can be written as below.[21-23]

$$[Al] + [N] = (AlN)_{(s)} \tag{4.1}$$

$$\Delta G^{\theta}_{AlN} = -303500 + 134.6T_{steel}\ \text{J/mol} \tag{4.2}$$

$$\log K_{AlN} = \log\frac{a_{AlN}}{h_{Al}h_N} = \log\frac{1}{f_{Al}f_N[\text{wt\% Al}][\text{wt\% N}]} \tag{4.3}$$

where ΔG^{θ}_{AlN} is the standard Gibbs free energy change of reaction (1), T_{steel} is the working temperature (1873 K, 1600°C), K_{AlN} is the equilibrium constant of the reaction (1), and h_{Al} and h_N are the Henrian activities of Al and N, respectively. f_{Al} and f_N are the activity coefficients of Al and N, respectively. A stability diagram for AlN formation was obtained using Equations (4.2) and (4.3). The activity coefficients of Al and N were calculated using the concentration of each element (Table 4.1) and first order interaction parameters from the literature.[23-29] The activity of AlN was assumed to be unity. Figure 4.4 shows the calculated stability diagram and the compositions of experimental steels. The average measured values of N and O contents were 3 and 10 ppm, respectively. These values were used to investigate the AlN formation in this study. It can be seen that all the steel compositions lie below the AlN stability line, which means that AlN is not stable at 1600°C for these compositions.

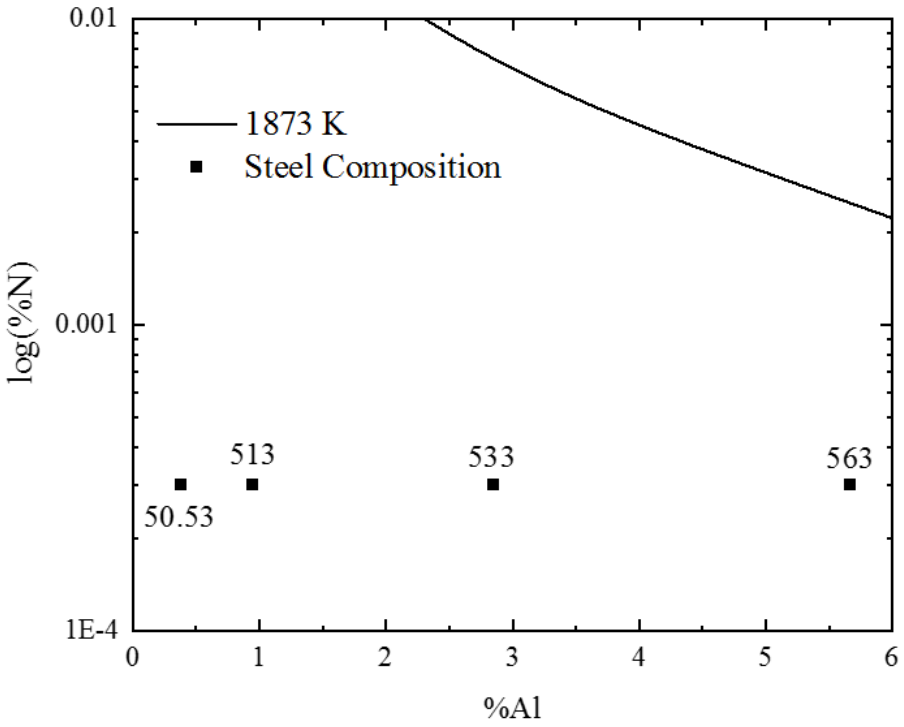

Figure 4. 4 The AlN stability diagram of Fe–5Mn–xAl alloy with different Al content at 1873 K.

Figure 4.4 also suggests that the AlN inclusions observed in the experimental steel would have formed during solidification and cooling of steel samples. This is because the driving force of AlN formation increases during solidification owing to the enrichment of Al and N at the solidification front. The Scheil equation[19,25,30] was used to calculate the concentration of [%Al] and [%N] in the liquid phase at the solidifying front. The equations for [%Al] and [%N] are given below.

$$[\%Al] = [\ \%Al]_0(1 - g_s)^{(k_{Al}-1)} \quad (4)$$

$$[\%N] = \frac{[\%\ N]_0}{k_N + (1 - k_N)(1 - g_s)} \quad (5)$$

where g_s is the solid fraction, and $[\ \%Al]_0$ and $[\%\ N]_0$ are the initial weight percentages of solute Al and N in liquid steel, respectively. k_{Al} (= 0.6) and k_N (= 0.27) are the equilibrium partition ratios of solute Al and N, respectively.[25,31] K_{AlN} can also be calculated according to Equation (4.6).[23]

$$K_{AlN} = 10^{-\frac{15850.93}{T_{steel}}+7.0297} \quad (4.6)$$

The relationship between the temperature at the solidifying front (T) and the solid fraction (g_s) is shown in Equation (4.7).[30]

$$T = T_m - \frac{T_m - T_{liq}}{1 - g_s \frac{T_{liq} - T_{sol}}{T_m - T_{sol}}} \quad (4.7)$$

where T_m, $T_{sol,}$ and T_{liq} are the melting temperature of pure Fe (1811 K, 1538°C), the solidus temperature of steel, and the liquidus temperature of steel, respectively. The values of T_{sol} and T_{liq} were obtained by FactSage 7.3 (FSstel, FToxid, and FactPS databases) and are listed in Table 4.2 for each type of steel.

Table 4. 2 The solidus and liquidus temperature of each steel type.

Steel	T_{sol} (K)	T_{liq} (K)
50.53	1647.4	1739.4
513	1629	1739.4
533	1619	1735.5
563	1605.93	1722.04

A relationship between the solid fraction (g_s) and product of [%Al] and [%N] was determined using Equations (4.4) – (4.6) and is plotted in Figure 4.5 for different N contents (3, 5, and 10 ppm). It also presents the variation in K_{AlN} for different g_s values. Figure 4.5

can be used to determine the value of g_s at which AlN formation starts during solidification. For instance, for 50.53 steel, the critical value of g_s for AlN formation at N = 3 ppm is 0.95 (Figure 4.5(a)). The formation of AlN inclusions can start at a lower g_s for 513, 533, and 563 steel samples (N = 3 ppm), i.e. at 0.89, 0.64, and 0.22, respectively. As the N content increases from 3 to 10 ppm, the g_s values decrease. In the case of 563 steel (Figure 4.5(d)), the g_s values for 5 and 10 ppm N contents are shallow which indicates that AlN inclusions can form in the liquid steel. This discussion explains thermodynamic conditions for the formation of AlN inclusions. According to the inclusion classification rules adopted in the current study, these inclusions would be classified as $AlN_{(pure)}$ inclusions, and only 563 steel contained $AlN_{(pure)}$ inclusions. This could be related to the low g_s value at which AlN formation starts in 563 steel.

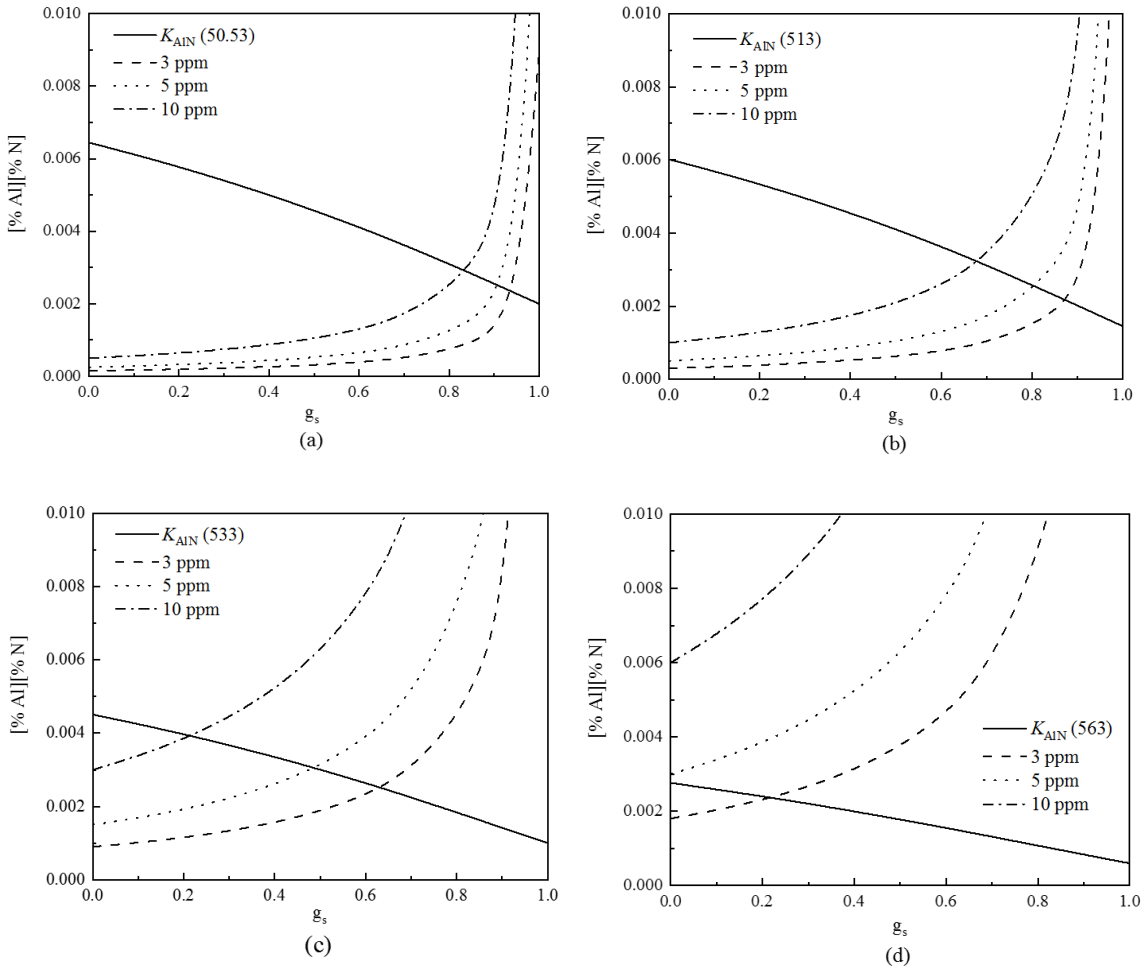

Figure 4. 5 The calculated value for a solid fraction of (a) 50.53, (b) 513, (c) 533, and (d) 563 steel samples.

Moreover, apart from $AlN_{(pure)}$ inclusions, complex nitride inclusions (AlON, AlON–MnS, and AlN–MnS) were also observed in steel samples. The formation mechanism of such inclusions is discussed in the subsequent sections.

4.3.2 Formation of AlON inclusions

According to the used inclusion classification rules, AlON inclusions contain both O and N. These inclusions could be either single-phase inclusions (i.e. AlON phase) or multiphase inclusions (i.e. Al_2O_3 + AlN). An Al_2O_3-AlN phase diagram suggests that the AlON phase is stable only above 1923 K (1650°C) and below this temperature dissociates into AlN + Al_2O_3.[32] This indicates that AlON inclusions observed in the current study were multi-phase inclusions (i.e. Al_2O_3 + AlN). Figure 4.6 presents an example of a typical AlON inclusion observed in 563 steel sample. The EDS mapping confirms that it is not a single AlON phase, rather it contains distinct Al_2O_3 and AlN phases, where Al_2O_3 is the core, and the periphery consists of AlN. Therefore, in the current study, AlON inclusions refer to multi-phase inclusions containing Al_2O_3 and AlN (a result of co-precipitation). As concluded in the previous section, for the current experimental steel compositions, AlN is not stable in liquid steel at 1600°C. Whereas Al_2O_3 is a stable phase in liquid steel. Based on the stability of these both phases, it can be inferred that the observed AlON inclusions are the result of AlN nucleation on the existing Al_2O_3 inclusions. The EDS mapping is shown in Figure 6 also approves this inference.

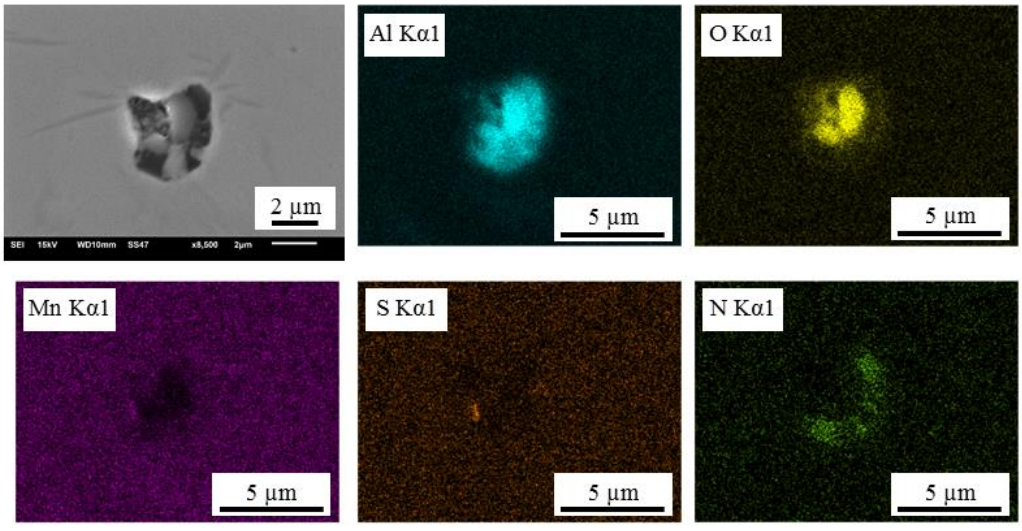

Figure 4. 6 Backscattered image and elemental mapping of typical AlON inclusion.

The nucleation of AlN on Al_2O_3 can be understood by considering the lattice disregistry concept. Bramfitt[33] suggested that an inclusion can act as an effective nucleation site for a solid phase when the disregistry between the substrate inclusion and nucleated solid is less than 12%. Dovidenko et al.[34] reported that the disregistry between (0001) AlN plane and (0001) Al_2O_3 plane is about 12%, which means that AlN can nucleate on Al_2O_3 inclusions.

The extent of Al_2O_3 inclusions to act as nucleation sites for AlN can be quantified in terms of precipitation ratio (PR) of AlN on Al_2O_3, which is defined as in Equation (4.8).

$$PR_{AlN\ on\ Al_2O_3} = \frac{N_{A_{(AlON)}}}{N_{A_{(Al_2O_3)}} + N_{A_{(AlON)}}} \times 100\% \quad (4.8)$$

where $N_{A_{(AlON)}}$ and $N_{A_{(Al_2O_3)}}$ are the number per unit area of AlON and $Al_2O_{3(pure)}$ inclusions, respectively.

Figure 4.7 shows the influence of Al content on the PR of AlN on Al_2O_3. The presented results are the values of 21 minutes samples. The results show that as the Al content increases from 0.5% to 6%, the value of PR increases from 1.2% to 56%. This can be justified by considering the presence of a higher amount of nucleation sites (Al_2O_3) and the formation of AlN at lower g_s values for high Al content steels as compared to those with low Al content.

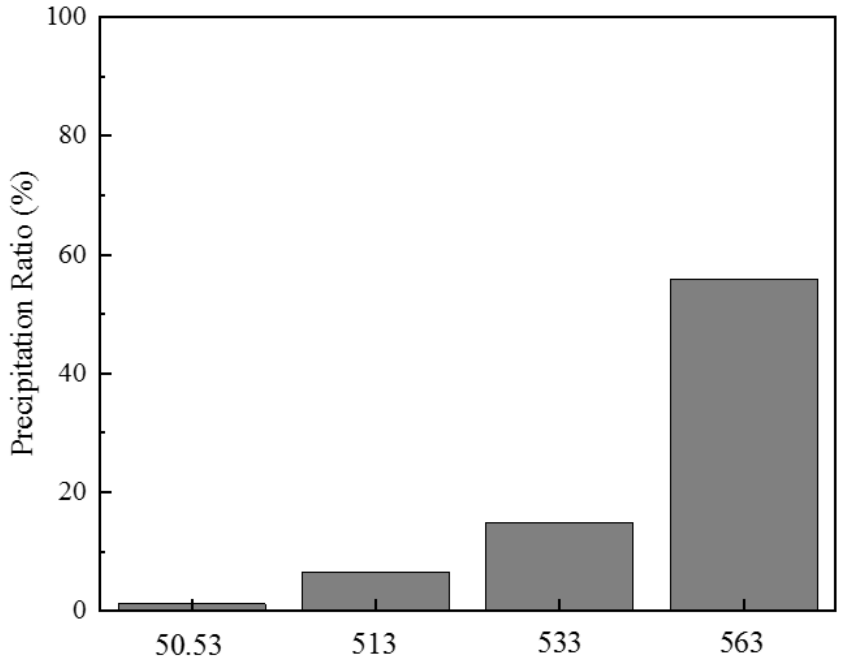

Figure 4. 7 The precipitation ratio of AlN on Al_2O_3 as in AlON inclusions detected in steel samples at the 21 minutes holding time.

4.3.3 Influence of Al on the amount of complex MnS inclusions

The effect of Al content on the complex MnS inclusions (Al_2O_3–MnS, AlN–MnS and AlON–MnS) is considered. Figure 4.8 illustrates the variation in the amount of MnS and MnS-complex inclusions with Al content in the steel. It can be seen that the total number

of MnS containing inclusions (MnS and MnS-complex inclusions) slightly decreases by increasing the Al content from 0.5% to 1%. Further, an increase in Al content to 3% and 6% resulted in a significant increase (almost two times) in this number. It can be clearly seen that this substantial difference is caused by MnS-complex inclusions. Hence, Figure 4.8 implies that increased Al content introduces a higher number of MnS-complex inclusions. The formation of MnS-complex inclusions occurs owing to the co-precipitation of MnS and other inclusions. The precipitation ratio (PR) of MnS on different inclusions can be assessed according to Equations (4.9) and (4.10).

$$\mathrm{PR}_{\mathrm{MnS\ on\ Al_2O_3}}\,(\%) = \frac{\mathrm{N}_{\mathrm{A}_{(\mathrm{Al_2O_3-MnS})}}}{\mathrm{N}_{\mathrm{A}_{(\mathrm{Al_2O_3})}} + \mathrm{N}_{\mathrm{A}_{(\mathrm{Al_2O_3-MnS})}}} \times 100\% \tag{4.9}$$

$$\mathrm{PR}_{\mathrm{MnS\ on\ AlN}}\,(\%) = \frac{\mathrm{N}_{\mathrm{A}_{(\mathrm{AlN-MnS})}}}{\mathrm{N}_{\mathrm{A}_{(\mathrm{AlN})}} + \mathrm{N}_{\mathrm{A}_{(\mathrm{AlN-MnS})}}} \times 100\% \tag{4.10}$$

where $\mathrm{N}_{\mathrm{A}_{(\mathrm{AlN})}}$, $\mathrm{N}_{\mathrm{A}_{(\mathrm{AlN-MnS})}}$ and $\mathrm{N}_{\mathrm{A}_{(\mathrm{Al_2O_3-MnS})}}$ are the number per unit area of $\mathrm{AlN_{(pure)}}$, AlN–MnS and Al_2O_3–MnS, respectively.

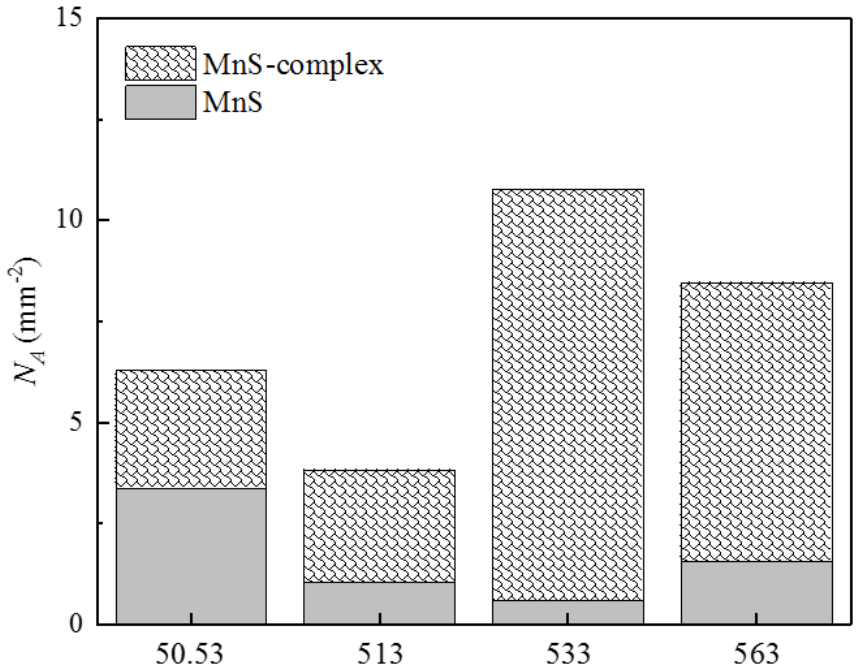

Figure 4. 8 Comparison of MnS and MnS-complex inclusions in 50.53, 513, 533, and 563 steel samples at the 21 minutes holding time.

Figure 4.9 presents the PR values of MnS on Al_2O_3 and AlN for each steel. It shows that MnS prefers to co-precipitate with AlN than Al_2O_3 as the PR value of MnS on AlN is more than 93% (except for 563 steel), whereas this value for Al_2O_3 is only 3–20%. However, the PR value of MnS on AlN for 563 steel is lower (41%) compared to that of other steels due to the formation of $AlN_{(pure)}$. The difference in the PR of MnS on AlN and Al_2O_3 inclusions is related to the potency of the latter to act as a nucleation site. As mentioned earlier, the potency of a particle to act as a nucleation site for another particle depends on the crystallographic matching between them. A lower mismatch means a higher possibility of heterogeneous nucleation. Ohta and Suito[35] calculated the lattice mismatch between MnS and different types of inclusions.They reported that the mismatch between MnS and AlN is ~6%, whereas that between MnS and Al_2O_3 is more than 12%.[36] This means less interfacial energy is required for the nucleation of MnS on AlN in comparison to that on Al_2O_3; hence, MnS would preferentially co-precipitate with AlN.

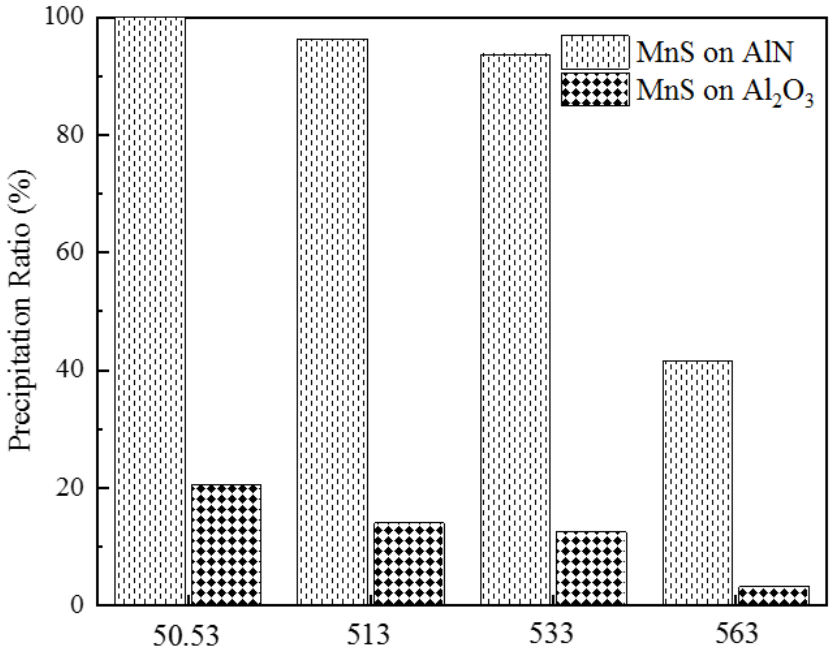

Figure 4. 9 Precipitation ratio of MnS on AlN and Al_2O_3 for 50.53, 513, 533, and 563 steel samples.

Further, due to the low mismatch between MnS and AlN, both AlN and MnS can act as nucleation sites for each other.[12] In a previous study,[20] the authors reported that MnS could co-precipitate with AlN by two scenarios: Scenario 1: Heterogeneous nucleation of AlN on MnS inclusions, and Scenario 2: AlN acting as a nucleation site for MnS. In Scenario 1, AlN is located at the edge or boundary of MnS inclusion, whereas, in Scenario 2, MnS is on the periphery of AlN inclusion. Typical examples of both two scenarios are presented in Figure 4.10.

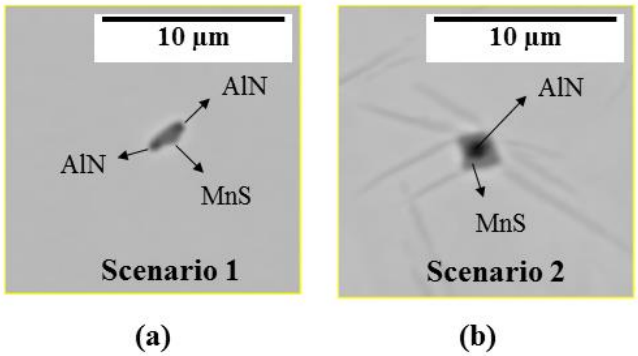

Figure 4. 10 Morphology of co-precipitates of AlN and MnS formed according to (a) Scenario 1 and (b) Scenario 2.

In the current study, it was observed that the co-precipitation behaviour of MnS and AlN is influenced by Al content in the steel. In order to quantify this observation, the morphological information of the MnS and AlN co-precipitates (AlN–MnS inclusions) was used to divide them into two groups. The groups represent co-precipitates formed according to Scenario 1 and Scenario 2. This analysis was conducted for 533 and 563 steel samples because of the abundance of AlN–MnS inclusions in these steels, which is required to have enough statistics to see a clear tendency. Figure 4.11 shows the obtained results. It can be seen that for 533 steel ~93% of AlN–MnS inclusions exhibit morphology in accordance with Scenario 1. For the case of 6% Al in steel (563), ~35% of co-precipitates are formed according to Scenario 2. This is in agreement with the thermodynamic data presented in Table 4.2. In the case of 563 steel, the AlN formation temperature is almost similar to the liquidus temperature. So, AlN inclusions most likely form first in liquid steel followed by MnS formation, resulting in a higher fraction of Scenario 2 morphology.

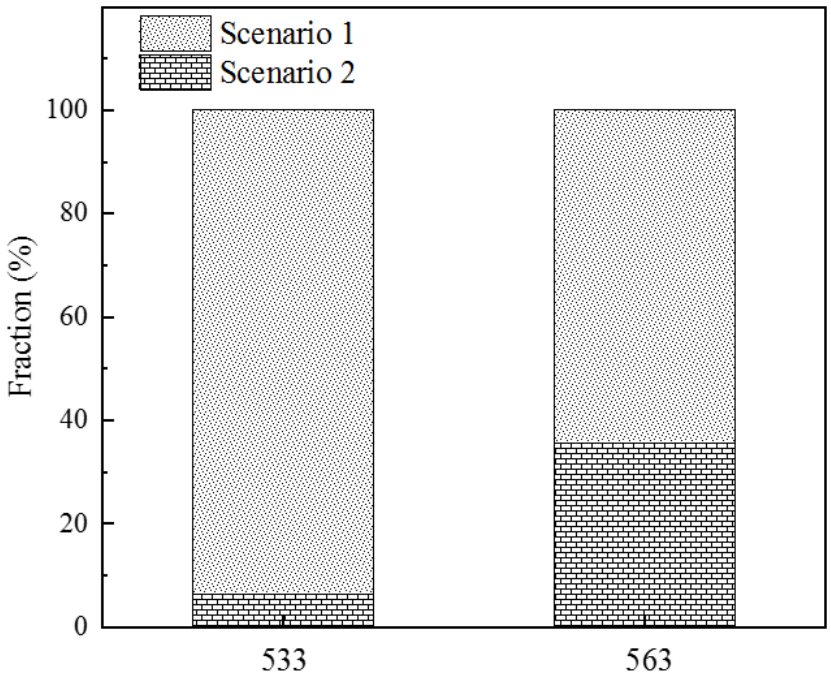

Figure 4. 11 Comparison of the morphology of AlN and MnS co-precipitates in 533 and 563 steel samples at the 21 minutes holding time.

Based upon the previous discussion, it can be presumed that AlON–MnS inclusions are the result of duplex heterogeneous nucleation, where Al_2O_3 is the first nucleation site. The formation sequence of AlON–MnS could be:

a. AlN nucleates on Al_2O_3 and later MnS nucleates on AlN

b. Al_2O_3 is nucleation site for MnS and then AlN nucleates on MnS

c. Both AlN and MnS nucleate simultaneously on Al_2O_3.

Further investigations are required to explore the formation mechanism of AlON–MnS inclusions.

4.5 Conclusion

The effect of aluminium on the inclusion formation in lightweight Fe–5Mn–xAl steels is investigated by conducting laboratory experiments. In these observations, an automated SEM analysis (ASPEX) is utilized. The following can be concluded from the obtained results.

- The observed inclusions in light-weight Fe–5Mn–Al steels are $Al_2O_{3(pure)}$, Al_2O_3–MnS, $AlN_{(pure)}$, AlN–MnS, AlON–MnS, AlON and MnS.
- Increasing aluminium content from 0.5% to 6% increases the total amount of inclusions by 2.5 times. The increase in the number of inclusions is specifically due to the rise in the number of AlN inclusions.
- For all four steel compositions, the AlN containing inclusions are solidification products due to their low nitrogen contents.

- AlN and Al_2O_3 inclusions can serve as a site for heterogeneous nucleation of MnS. MnS inclusion prefers to coprecipitate with AlN than Al_2O_3 inclusions.

4.6 Acknowledgement

The authors would like to express gratitude to the Natural Sciences and Engineering Research Council of Canada (Project No: 20007079) for the financial support for this work. Further, we want to thank Dr. Stanley Sun and Ms. Li Sun at ArcelorMittal Dofasco for their valuable time and fruitful discussions.

4.7 References

1. Lee Y-K, Han J. Current opinion in medium manganese steel. Mater Sci Technol 2015;31:843.
2. Billur E, Altan T. Three Generations of Advanced High Strength Steels for Automotive Applications, Part III - The Third Generation. Stamp. J. 2014: 12.
3. Aydin H, Essadiqi E, Jung IH, et al. Development of 3rd generation AHSS with medium Mn content alloying compositions. Mater Sci Eng A. 2013;564:501.
4. Hu B, Luo H, Yang F, et al. Recent progress in medium-Mn steels made with new designing strategies, a review. J Mater Sci Technol 2017;33:1457.
5. Cai ZH, Cai B, Ding H, et al. Microstructure and deformation behavior of the hot-rolled medium manganese steels with varying aluminum- content. Mater Sci Eng A. 2016;676:263.
6. Mapelli C, Barella S, Gruttadauria A, et al. Decomposition in Fe–Mn– Al–C lightweight steels. J Mater Res Technol. 2020;9:4604.
7. Kim H, Suh DW, Kim NJ. Fe–Al–Mn–C lightweight structural alloys: a review on the microstructures and mechanical properties. Sci Technol Adv Mater. 2013;14(1).
8. Suh DW, Park SJ, Lee TH, et al. Influence of Al on the microstructural evolution and mechanical behavior of low-carbon, manganese transformation-induced-plasticity steel. Metall Mater Trans A Phys Metall Mater Sci. 2010;41:397.
9. Arlazarov A, Gouné M, Bouaziz O, et al. Evolution of microstructure and mechanical properties of medium Mn steels during double annealing. Mater Sci Eng A. 2012;542:31.
10. Park JH, Kim DJ, Min DJ. Characterization of nonmetallic inclusions in high-manganese and aluminum-alloyed austenitic steels. Metall Mater Trans A. 2012;43:2316.
11. Mapelli C. Control and engineering of non-metallic inclusions belonging to $xSiO_2$–$yCaO$–zAl_2O_3 system in Ca-treated Al-killed and Al–Si-killed steel. Steel Res Int. 2006;77:462.
12. Tuling A, Mintz B. Crystallographic and morphological aspects of AlN precipitation in high Al, TRIP steels. Mater Sci Technol 2016;32:568.
13. Kang SE, Banerjee JR, Mintz B. Influence of S and AlN on hot ductility of high Al, TWIP steels. Mater Sci Technol 2012;28:589.

14. Funnell GD, Davies RJ. Effect of aluminium nitride particles on hot ductility of steel. Met Technol. 1978;5:150.
15. Ånmark N, Karasev A, Jönsson P. The effect of different Non-metallic inclusions on the machinability of steels. Materials (Basel). 2015;8:751.
16. He S, Chen G, Guo Y, et al. Morphology control for Al2O3 inclusion without Ca treatment in high-aluminum steel. Metall Mater Trans B. 2015;46:585.
17. Mapelli C. Non-metallic inclusions and clean steel. Metall Ital 2008;100:43.
18. Nabeel M, Alba M, Sun S, et al. in AISTech, 2018.
19. Nabeel M, Alba M, Karasev A, et al. Characterization of inclusions in 3rd generation advanced high-strength steels. Metall Mater Trans B. 2019;50:1674.
20. Alba M, Nabeel M, Dogan N. Investigation of inclusion formation in light-weight Fe–Mn–Al steels using automated scanning electron microscope equipped with energy-dispersive X-ray spectroscopy. Steel Res Int. 2020;91(3).
21. Jang J-M, Paek M-K, Pak J-J. Thermodynamics of nitrogen solubility and AlN formation in multi-component high Mn steel melts. ISIJ Int 2017;57:1821.
22. Liu H, Liu J, Michelic SK, et al. Cover picture: steel research int. 1/ 2016. Steel Res Int. 2016;87:1.
23. Paek M-K, Jang J-M, Kang H-J, et al. Reassessment of AlN (s)= Al+N equilibration in liquid Iron. ISIJ Int 2013;53:535.
24. Paek M-K, Jang J-M, Do K-H, et al. Nitrogen solubility in high manga- nese-aluminum alloyed liquid steels. Met Mater Int 2013;19:1077.
25. Paek M, Jang J, Jiang M, et al. Thermodynamics of AlN formation in high manganese-aluminum alloyed liquid steels. ISIJ Int 2013;53:973.
26. JSPS. Steelmaking data sourcebook. Revised. Gordon and Breach Science Publications; 1988.
27. Sigworth GK, Elliot JF. The thermodynamics of liquid dilute iron alloys. Met Sci 1974;8:298.
28. Itoh H, Hino M, Ban-Ya S. Assessment of Al deoxidation equilibrium in liquid iron. Tetsu-to-Hagane. 1997;83:773.
29. Kim DH, Jung MS, Nam H, et al. Thermodynamic relation between silicon and aluminum in liquid iron. Metall Mater Trans B Process Metall Mater Process Sci. 2012;43:1106.
30. Liu H, Liu J, Michelic S, et al. Characteristics of AlN inclusions in low carbon Fe–Mn–Si–Al TWIP steel produced by AOD-ESR method. Ironmak Steelmak 2016;43:171.
31. Turkdogan ET. Fundamentals of steelmaking. London: The Institute of Materials; 1996.
32. Willems HX, Hendrix MMRM, de With G, et al. Thermodynamics of Alon II: phase relations. J Eur Ceram Soc 1992;10:339.
33. Bramfitt BL. The effect of carbide and nitride additions on the het- erogeneous nucleation behavior of liquid iron. Metall Trans. 1970;1:1987.

34. Dovidenko K, Oktyabrsky S, Narayan J, et al. Aluminum nitride films on different orientations of sapphire and silicon. J Appl Phys 1996;79:2439.
35. Ohta H, Suito H. Precipitation and dispersion control of MnS by deoxidation products of ZrO2,Al2O3, MgO and MnO–SiO2 particles in Fe–10mass%Ni alloy. ISIJ Int 2006;46:480.
36. Li F, Li H, Huang D, et al. Mechanism of MnS precipitation on Al_2O_3–SiO_2 inclusions in non-oriented silicon steel. Met Mater Int 2018;24:1394

Chapter 5

Effect of Nitrogen Content on the Formation of Inclusions in Fe-5Mn-3Al Steels

Chapter 5 is a pre-publication version of the article published in the special edition journal of Crystals 2020, DOI: 10.3390/cryst10090836. The following chapter discusses the effects of nitrogen content (2-54 ppm) on the characterization of inclusions in the laboratory produced Fe-5Mn-3Al steels. In this study, two different techniques for nitrogen addition were applied. Previously in Chapter 3, FeN was introduced to the synthetic melt, whereas N_2 gas was either purged on the liquid metal or injected through a lance into the liquid metal. Similar to Chapters 3 and 4, the analysis of the inclusion was performed by an automated scanning electron microscope (SEM) equipped with the ASPEX feature, and identical inclusion classification rules were applied in this chapter. It was found that as the N content increased, the total amount of inclusions increased; however, there were no changes in the composition of detected inclusions. It was found that AlN-MnS inclusions were the primary inclusion type when the N content in the steel is low (~2 ppm N). As the N content in the steel increased to 54 ppm, the dominant inclusions changed to $AlN_{(pure)}$. The thermodynamic calculations were conducted to study the formation mechanism of the AlN-containing inclusions. The AlN inclusions formed in low N content steel are the solidification products, while the AlN inclusions in high N content steel are formed in the liquid steel. Moreover, the samples with different cooling rates were also discussed. In the slow cooling rate steel, AlN-MnS inclusions always formed regardless of the content of N in the steel. AlN inclusions were also observed to have different morphologies such as plate-like, needle, angular, agglomerate, and irregular.

All the experiments, data collection, and analysis were completed by the primary author. Li Sun (ArcelorMittal Dofasco) provided training for using automated SEM (ASPEX). Dr. Muhammad Nabeel assisted with the SEM inclusion imaging. The manuscript was written by the primary author. Dr. Muhammad Nabeel and Dr. Neslihan Dogan contributed to the discussion and proofread the manuscript.

Effect of Nitrogen Content on the Formation of Inclusions in Fe-5Mn-3Al Steels

Michelia Alba,* Muhammad Nabeel, and Neslihan Dogan

Michelia Alba, Ph.D. Student, albam@mcmaster.ca
Department of Material Science and Engineering, McMaster University, 1280 Main Street West, Hamilton, ON L8S 4L7, Canada

Muhammad Nabeel, Postdoctoral Fellow,
Department of Material Science and Engineering, McMaster University, 1280 Main Street West, Hamilton, ON L8S 4L7, Canada

Neslihan Dogan, Assistant Professor,
Department of Material Science and Engineering, McMaster University, 1280 Main Street West, Hamilton, ON L8S 4L7, Canada

Abstract

The effect of N content on the characteristics and formation of inclusions in the Fe-5Mn-3Al steels was investigated in this study. Two synthetic steel melts were produced by two different methods to introduce nitrogen into the melt. They are namely N_2 gas purging and injecting. The N content of steel melt varied from 2 to 54 ppm. An increase in the N content to 47 ppm (for 533N-P) and 58 ppm (for 533N-I) increased the total amount of inclusions from 13 to 64 mm^{-2} and from 21 to 101 mm^{-2}, respectively. The observed inclusions were $Al_2O_{3(pure)}$, Al_2O_3-MnS, $AlN_{(pure)}$, AlN-MnS, AlON, AlON-MnS, and MnS. When the N content was less than 10 ppm, AlN-MnS inclusions were the primary type of inclusions, and they formed as solidification products. With an increase in the N content, $AlN_{(pure)}$ inclusions became the dominant type of inclusions as AlN was stable in the liquid steel. These findings were confirmed with the thermodynamic calculations. The influence of cooling rate on the types of inclusions was studied and a higher number of AlN-MnS inclusions were observed in samples with a slow cooling rate.

5.1 Introduction

Among the third generation of Advanced High Strength Steel (AHSS), medium manganese steels are getting more popular because they have a high tensile strength similar to that of

high manganese steels while having reduced production cost.[1] Medium manganese steels are preferred over the high manganese steels because of problems associated with continuous casting due to poor hot ductility of high manganese steels.[2-4] This poor hot ductility is caused by the precipitation of inclusions (e.g., AlN) in the steel.[3] The presence of inclusions in steel is known for their adverse impact on the mechanical properties of the steel and the information regarding the characteristics of inclusions (such as their size, morphology, and composition) in medium manganese steels is limited.[3,5-13] Notably, the influence of the alloying elements on the formation of inclusions in the medium manganese steel is not well known.[5,8] The authors[14,15] investigated the effect of Mn and Al contents in liquid steel on the formation of inclusions. They found that with an increase in the Mn content, the number of inclusions increased, particularly AlN and MnS inclusions.[14] It was justified by the fact that manganese content can increase the solubility of nitrogen in the steel.[16,17] Moreover, it was also found that with increasing Al content from 0.5% to 6% in the medium manganese steel (~5% Mn), the total number of inclusions also increased 2.5 times, especially the number of AlN inclusions which increased from 2 mm^{-2} to around 20 mm^{-2}.[15]

Liu et al.[18] investigated the formation of AlN inclusions in high manganese steel (Fe-25Mn-3Al-3Si) produced in Electroslag Remelting (ESR) and Argon Oxygen Decarburization (AOD) processes with a nitrogen content of 6 and 24 ppm, respectively. They reported that the AlN inclusions observed in ESR steel (6 ppm N) formed during the solidification process and the AlN inclusions found in AOD steel (24 ppm N) formed in liquid steel during cooling. Xin et al.[19] also observed AlN inclusions in high manganese steel (Fe-17Mn-2Al-0.6C) with N content of 43 ppm. The calculated formation temperature of AlN in the steel was around 9 degrees lower than the liquidus temperature,[19] which suggests that AlN inclusions were formed in the mushy zone during solidification of steel. Thus, the formation behavior of AlN inclusions depends on the N content of steel, i.e., AlN inclusions can be solidification products in low N containing steels[20] or they can form during the refining of liquid steel with high nitrogen content.[18,21] The inclusions that are formed as a solidification product usually exist in small sizes.[22] On the other hand, the inclusions which form in liquid steel can grow to a larger size or agglomerate with other inclusions. Thus, a difference in the size distribution of AlN inclusions formed at different N contents can be expected. Moreover, AlN inclusions exhibit different morphologies. In the previous studies,[9,23-25] the morphology of AlN inclusions has been reported as hexagonal,[9] plate-like,[24] rod[9] or needle-like,[23] and dendritic[25] form. To the authors' knowledge, there is no systematic study on the effect of N content on the characteristic of inclusions and their formation behavior in medium Mn steel.

Therefore, this study aims at investigating the influence of N content on the formation of inclusions in medium Mn steels. For this, two experimental steel melts were produced in the laboratory by introducing N gas into steel through different methods. Both steel melts were investigated for variation in the characteristics of inclusions, i.e., their number density, composition, size, and morphology. Furthermore, the formation mechanism of inclusions is discussed, considering the characteristics of inclusions and thermodynamics.

5.2 Materials and Methods

A resistance-heated vertical tube furnace was used to produce synthetic steel containing Fe-5Mn-3Al-3Si-0.1C. A schematic diagram of the experimental set up is shown in Figure 1. Before heating, the furnace chamber was evacuated and backfilled with high purity Ar gas (99.999%) at a flow rate of 500 ml/min. The oxygen content in Ar gas was reduced by passing it through Ti turnings at 923 K. The steel material was charged in an alumina crucible and heated to 1873 K. Two experiments were set up using different methods for introducing N_2 gas into the molten steel. In both experiments, the furnace chamber was evacuated after reaching the target temperature. In the first experiment (533N-P), the chamber was backfilled by purging a mixture of Ar and N_2 gas (1:1). After 180 minutes, the mixing ratio was changed to Ar:N_2 = 1:2. In the second experiment, after the evacuation, the chamber was backfilled with only Ar gas (500 ml/min), and N_2 gas was introduced by injecting it into the molten steel bath by using alumina tube at a rate of 300 ml/min. The alumina tube was at the height of 1.5 cm from the bottom of the crucible, i.e., almost in the center of the molten steel bath. This set of experiments is denoted as 533N-I. In this experiment, N_2 gas was purged directly from a cylinder (99.999% N_2) without passing through Ti turnings, see Figure 5.1. In both experiments, several pin samples were taken to monitor the N content in the steel melts. The sampling sequence is shown in Table 5.1. The first sample (S1) was taken before introducing N_2 gas in the system. All the pin samples were air-cooled, while the remaining bulk steel was cooled along with the furnace, at a cooling rate of 0.167 K/sec. In the case of the 533N-P experiment, there is a 180 minutes gap between S4 and S5 samples. Several samples were taken between S4 and S5; however, there was no significant change in the N content during that holding time. So, the samples shown in Table 5.1 were chosen to represent the considerable variation in the N content of steel melt.

Table 5. 1 Experimental steps

533N-P	533N-I
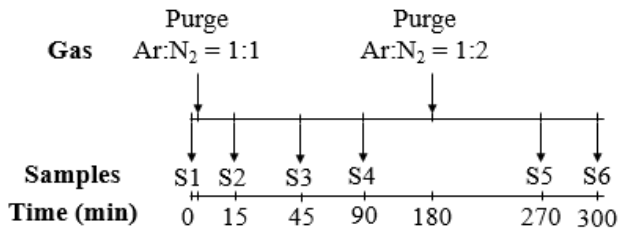	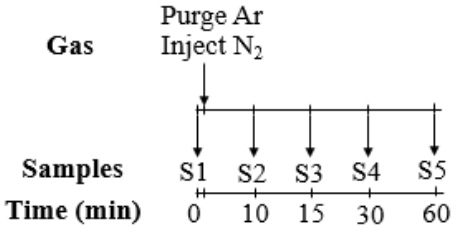

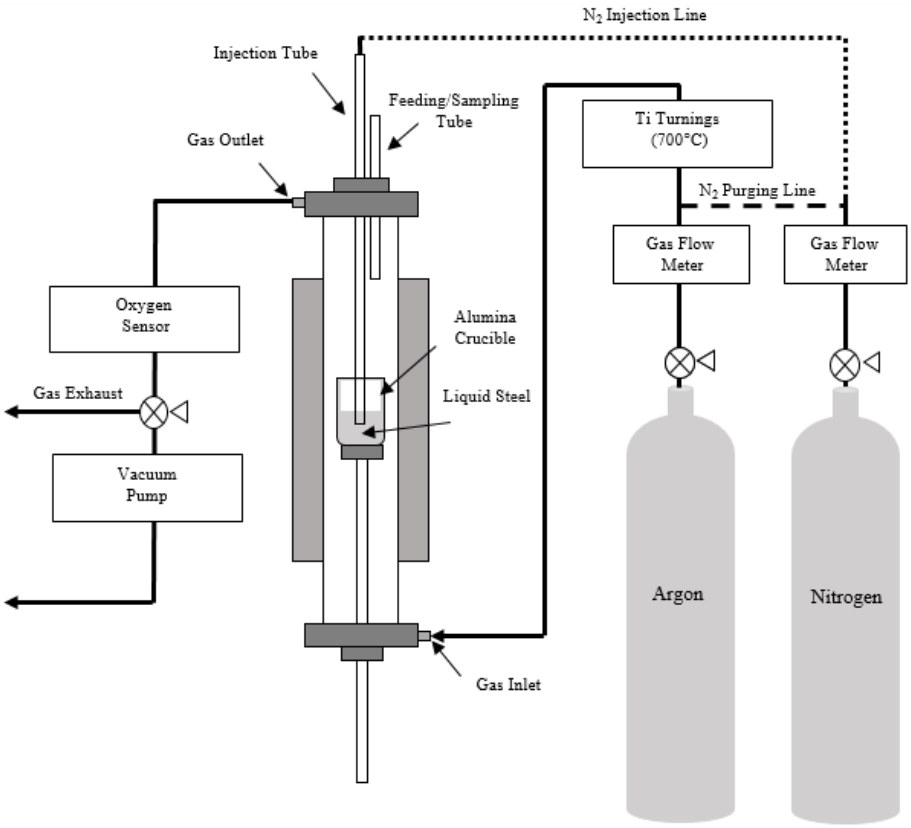

Figure 5. 1 Schematic diagram of the experimental set-up used in this study.

The oxygen-nitrogen and carbon-sulfur contents of samples were measured by commercial LECO O/N (ON736)™[26] and LECO C/S (CS744)™[27] analyzer, respectively. The chemical analysis of steel samples was conducted by Induction Coupled Plasma Optical Emission Spectrometry (ICP-OES). The steel samples were analyzed for inclusions by using an automated scanning electron microscope (SEM) equipped with an ASPEX™,[28] which is a commercial system for inclusion analysis. The following parameters were used: magnification – 356x, accelerating voltage – 20 kV, emission current – 43.4 µA, and spot size – 35%. The analyzed area and the total number of detected inclusions varied from 10 to 42 mm^2 and around 330 to 2943, respectively. In this study, the inclusions having a maximum diameter (D_{max}) > 2 µm were detected. All the inclusions were classified into four major inclusion classes, which are Al_2O_3, AlN, MnS, and Other. Furthermore, the Al_2O_3 class was divided into two subclasses, $Al_2O_{3(pure)}$ and Al_2O_3-MnS. In the case of AlN, it had four subclasses, which were $AlN_{(pure)}$, AlN-MnS, AlON-MnS, and AlON. The 'Other' class contained complex oxide inclusions besides the aforementioned classes. The details of the inclusion classification were described elsewhere.[14]

5.3 Results

5.3.1 Chemical Composition of the Steels

The chemical composition of the steel samples is listed in Table 5.2. The nitrogen content of the 533N-P steel samples increased with the holding time. For Ar:N_2 = 1:1, the highest value of N content was measured in S4. An increase in the N_2 ratio in the gas mixture (Ar:N_2 = 1:2) resulted in a maximum value of 54 ppm after 270 minutes (S5). However, the N content in the 533N-I steel reached 54 ppm only after 10 minutes of injecting N_2 gas into the steel melt, and it remained almost constant throughout the experiment. The O content of the samples of 533N-I steel was higher, especially for samples taken at 10 and 15 minutes. These high values could be the result of oxygen impurities in N_2 gas, which was injected into the steel melt. N_2 gas was not passed through the titanium turning in the 533N-I experiment. The results from the LECO analyzer will have a deviation of around ± 2 ppm while the elemental analysis using ICP-OES has a relative standard deviation (RSD) of less than 5%.

Table 5. 2 The chemical composition of the steel melts.

Steel Set	Sample	Time (min)	Mn (%)	Al (%)	Si (%)	C (%)	S (%)	N (ppm)	O (ppm)
533N-P	S1	0	4.96	2.63	3.77	0.103	0.0028	2	14
	S2	15						23	3
	S3	45						33	9
	S4	90						47	2
	S5	270						54	2
	S6	300						52	3
533N-I	S1	0	4.77	2.74	4.12	0.102	0.0027	-	4
	S2	10						54	16
	S3	15						54	25
	S4	30						-	-
	S5	60						54	11

5.3.2 Characteristics of Inclusions

Figure 5.2 presents the number per unit area of inclusions (N_A) observed in samples taken during the two experiments. It could be seen that sample S1, which was taken before introducing N to the steel melt, contained 13 mm^{-2} and 21 mm^{-2} of inclusions in 533N-P and 533N-I steel, respectively. In sample S1 from 533N-P, the Al_2O_3 inclusions counted for almost 80%, and the rest of the inclusions were AlN. While, before N_2 injection in 533N-I steel melt, it contained ~40% of Al_2O_3 and AlN inclusions each. In 533N-P steel melt, the N_A value of inclusions gradually increased from 13 to 64 mm^{-2} as the N content of steel reached 47 ppm (after 90 minutes of N purging in the system). Thereafter, the N_A value remained almost constant with increasing holding time despite a slight increase in the N content of steel (to more than 50 ppm). The N_A value of Al_2O_3 inclusions decreased from 10 to less than 1 mm^{-2}, while the N_A value of AlN inclusions substantially increased from

3 to 62 mm^{-2}. The number of MnS and 'Other' inclusions were generally low, i.e., < 5% of total inclusions.

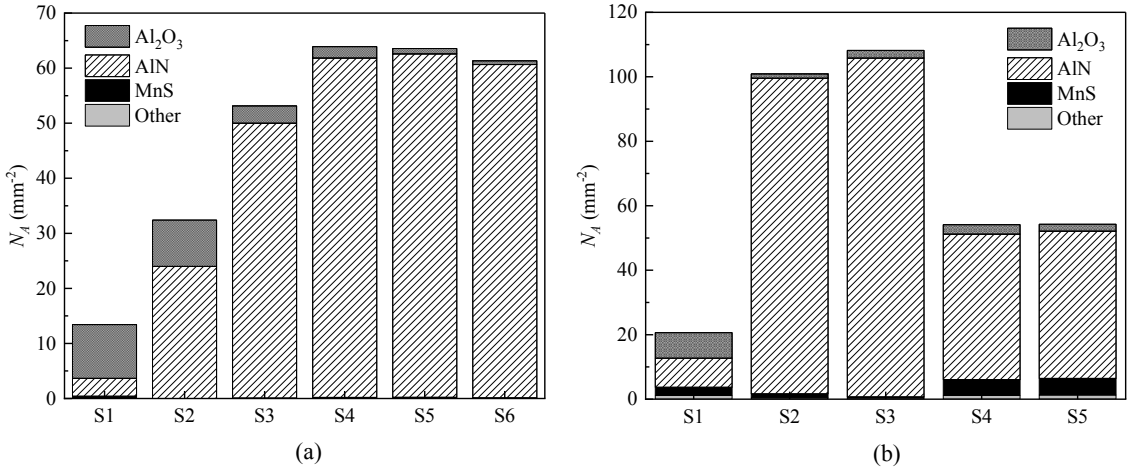

Figure 5. 2 The total number of inclusions per unit area and their composition detected in (a) 533N-P and (b) 533N-I steel melts.

Similar to 533N-P, a significant increase in N_A of inclusions was observed in 533N-I steel samples after injection of N_2 gas in the steel melt (Figure5. 2(b)). The N_A value increased from 21 to 101 mm^{-2} within 10 minutes of N_2 injection as the melt achieved an N content of 58 ppm. A little increase in the N_A value of inclusions occurred in sample S3 (15 minutes after N_2 injection). Thereafter, although the N content of steel did not show much variation, the number of inclusions decreased by almost 50% after 30 minutes of holding, and then it remained virtually constant. Similar to the 533N-P steel, as N content of 533N-I steel increased, the N_A value of Al_2O_3 inclusions decreased to less than 1 mm^{-2}, and that of AlN substantially increased counting for more than 95% of the total number of inclusions. The N_A of MnS inclusions in 533N-I steel samples was also relatively small (N_A < 5 mm^{-2}), and the N_A of 'Other' inclusion was negligible.

A comparison of both experiments shows that it took a longer holding time (more than 90 minutes) for steel to achieve the highest N content when N_2 gas was purged in the system, while the maximum N content was attained within 10 minutes of injecting N_2 gas into the melt. Moreover, 533N-I steel contained ~60% higher number of inclusions as compared to that of 533N-P steel for a similar N content of steel melt.

The variation in the characteristics of inclusions was further explored by analyzing the sub-classes of Al_2O_3 and AlN inclusions. In 533N-P samples, more than 90% of Al_2O_3 inclusions were $Al_2O_{3(pure)}$, and remaining were Al_2O_3-MnS. The sample S1 from 533N-I contained 8 mm^{-2} of Al_2O_3 inclusions, out of which ~60% are $Al_2O_{3(pure)}$. In the remaining samples, the percentage of $Al_2O_{3(pure)}$ varied from 20-90% of Al_2O_3 inclusions. However,

the fraction of Al_2O_3 inclusions were generally insignificant in all samples except in S1 and S2 from 533N-P and S1 from 533N-I steel.

Figure 5.3 presents the influence of N content on the characteristics of sub-classes of AlN inclusions. AlN-MnS was the dominant sub-class before the purging of N_2 gas in 533N-P steel (Figure 5.3(a)). It made over 60% of AlN inclusions in S1, while the fractions of AlON and AlON-MnS were ~18% each. As the N content increased to 23 ppm in sample S2, a significant amount (more than 50%) of $AlN_{(pure)}$ inclusions appeared, and the fraction of AlN-MnS was reduced to less than 10%. The fraction of AlON inclusions in S2 was almost 40%, and the amount of AlON-MnS was negligible. With further increase in N content in 533N-P steel, the percentage of $AlN_{(pure)}$ inclusions kept on increasing at the expense of that of AlN-MnS and AlON-MnS. The AlN inclusions in sample S5 (54 ppm N) and S6 (52 ppm N) contained more than 95% of $AlN_{(pure)}$ and ~5% of AlON, while ~1% of these inclusions was AlN-MnS.

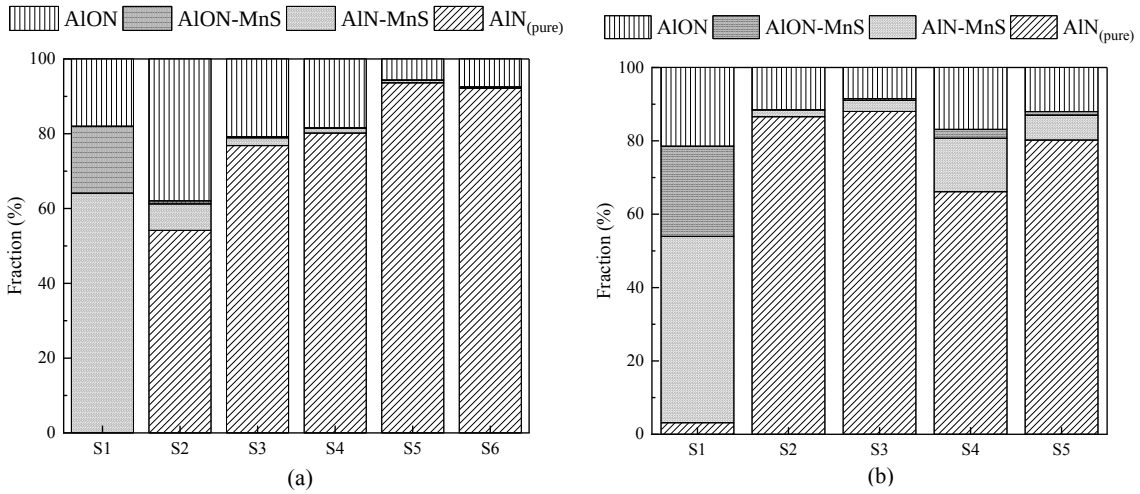

Figure 5. 3 The fraction of subclasses of AlN inclusions for (a) 533N-P and (b) 533N-I steels.

As shown in Figure 5.3(b), before N_2 gas injection, MnS containing nitrides (i.e., AlN-MnS and AlON-MnS) were also dominated sub-classes among others of AlN in 533N-I steel. AlN-MnS and AlON-MnS added up to ~80% of AlN inclusions. The AlN inclusions in S2 (58 ppm N) and S3 (56 ppm N) from 533N-I steel exhibited similar characteristics as those of AlN inclusions observed in S5 and S6 from 533N-P steel. AlN inclusions in these samples contained <5% MnS containing nitrides. Thereafter, despite the high N content of samples S4 and S5, the fraction of AlN-MnS and AlON-MnS inclusions increased to (~26%) and (~10%), respectively. Though Figure 5.3 suggested that the fraction of AlN-MnS and AlON-MnS inclusions was significantly influenced by the N content of steel, the N_A value of these inclusions was not much affected by N content. It can be seen in Table

5.3 that the N_A values of AlN-MnS and AlON-MnS were consistently low (≤ 6 mm^{-2}) compared to the total amount of inclusions in each sample in both steel melts.

Table 5. 3 The N_A values of AlN-MnS and AlON-MnS inclusions in 533N-P and 533N-I steel melts.

533N-P	S1	S2	S3	S4	S5	S6
AlN-MnS (mm^{-2})	2.08	1.70	1.05	0.76	0.41	0.23
AlON-MnS (mm^{-2})	0.58	0.20	0.14	0.12	0.08	0.03
533N-I	S1	S2	S3	S4	S5	
AlN-MnS (mm^{-2})	4.57	1.78	3.20	6.58	3.10	
AlON-MnS (mm^{-2})	2.21	0.11	0.50	1.10	0.45	

5.4 Discussions

5.4.1 Thermodynamics of AlN Formation

The thermodynamic analysis was carried out to evaluate the formation behavior of AlN inclusions. The analysis aimed at determining: the critical N content required for the formation of AlN in liquid steel, the effect of temperature on the formation of AlN, and the solid fraction (g_s) values at which AlN forms during solidification.

Figure 5.4 presents an AlN stability diagram for the experimental steel composition of 533N-P and 533N-I, obtained by using FactSage 7.3 (FSstel, FToxid, and FactPS databases). The figure also shows AlN stability lines for different temperatures, including liquidus temperature (T_{liq}) of experimental steels. T_{liq} was around 1726.3 K, while the critical N content for the formation of AlN at 1873 K was 50 ppm for the steel melt containing 2.67% Al (average value) in the current study. Whereas, at 1823 K and 1773 K it was 30 ppm and 15 ppm, respectively. The experimental compositions plotted in Figure 5.4 indicate that AlN could form in liquid steel at 1873 K in sample S5 and S6 from 533N-P. The composition of S4 lay just below the 1873 K line, and those of S3 and S2 were above the 1773 K line. This indicates that AlN is not stable at 1873 K for S4, S3, and S2. However, AlN can form in liquid steel at temperatures above 1773 K during the cooling of these samples. Moreover, the composition of S1 was below the T_{liq} line, suggesting that AlN can only form in the mushy zone during solidification of S1.

For the case of 533N-I steel, AlN can form at 1873 K in all the samples, except S1. The N content of S1 was not known. However, authors have observed in previous work[15] that Fe5Mn3Si3Al steels (without N addition) contained < 10 ppm of N. Therefore, it was reasonable to assume that S1 in 533N-I steel had an N content of less than 10 ppm. This assumption would locate the S1 below the T_{liq} line in Figure 5.4. Thus, the AlN inclusions observed in S1 samples of both experiments were formed during solidification of the steel due to the enrichment of Al and N at the solidifying front. The enrichment led to a higher driving force for the formation of AlN. The solid fraction (g_s) values at which AlN would

start to form for the S1 compositions were calculated by adopting the Scheil equation.[18,29,30] The detailed procedure for this calculation was given elsewhere.[14,18] According to the estimates, the g_s values for S1 samples should be higher than 0.11 (based on 10 ppm N), and they could be as high as 0.71 assuming 2 ppm N content.

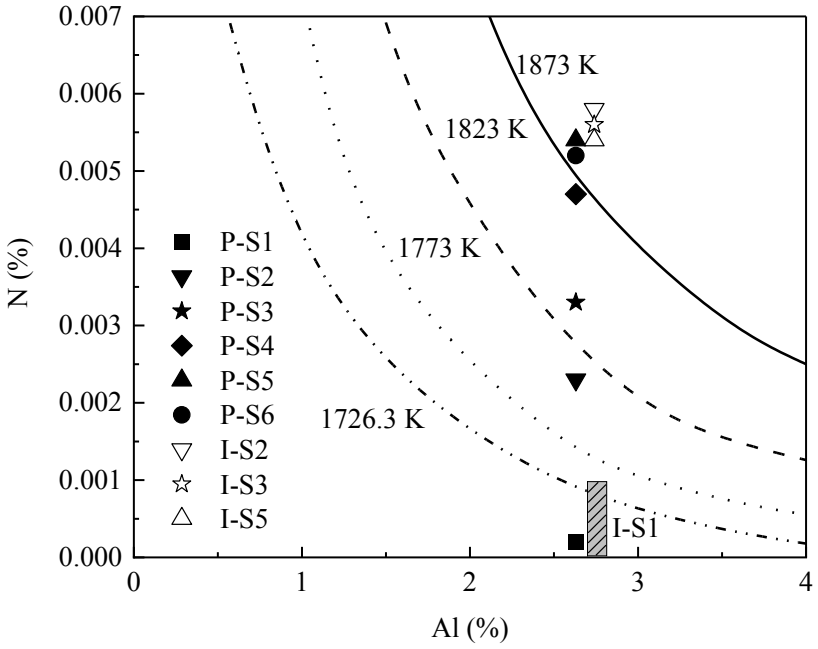

Figure 5. 4 AlN stability diagram for the experimental steel composition of 533N-P and 533N-I, obtained by using FactSage 7.3

The current steel compositions could be divided into three groups following their N contents, i.e., low N (2-10 ppm), medium N (23-47 ppm), and high N (> 50 ppm) containing steels. Based on the thermodynamic analysis, it could be inferred that for low N containing steel samples, AlN inclusions formed in the mushy zone due to the segregation of Al and N at the solidification front. For both medium and high N containing samples AlN formed in the liquid steel. However, AlN formation occurred during the cooling of medium N containing samples. Whereas, AlN observed in high N containing samples formed at the experimental temperature.

A variation in the characteristics of AlN inclusions in the above mentioned three groups could be expected due to the difference in the formation behavior of AlN inclusions in them. These characteristics included the number density of inclusions, their chemical composition, and their size distribution. The expected response was reflected in the results presented in Figure 5.3(a) and Figure 5.3(b).

The influence of N content on the particle size distributions (PSD) of AlN inclusions can be seen in Figure 5.5. In the case of low N containing samples (i.e., S1), most of the AlN inclusions lay in size range of 1-2 μm. Specifically, 92% and 80% of AlN inclusions in S1

from 533N-P and 533N-I steel melts had D_{ave} < 2 μm, respectively. It is evident from Figure 5.5(a) that the percentage of AlN inclusions with D_{ave} < 2 μm decreased as the N content increased in samples of 533N-P steel. In high N containing samples (S5 and S6), ~40% of AlN inclusions were greater than 2 μm. Similarly, the samples with high N from the 533N-I melt (Figure 5.5(b)) contained only ~20% of AlN (except S3, which contains ~45%) in the size range of D_{ave} < 2 μm in comparison to 80% in low N sample. A higher fraction of small-sized inclusions (D_{ave} < 2 μm) in samples with low N levels supports the inference that AlN inclusions form during solidification in these samples. Interestingly, the fraction of large-sized inclusions in high N containing samples of 533N-I was considerably higher than in those of 533N-P. This can be attributed to a higher growth rate of AlN inclusions due to turbulence induced by injection of N_2 gas in the melt. The increased size of inclusions was also reflected as a decreased number of AlN inclusions in S4 and S5 of 533N-I (Figure 5.2(b)) steel, which was probably due to the floatation of inclusions to the steel surface.

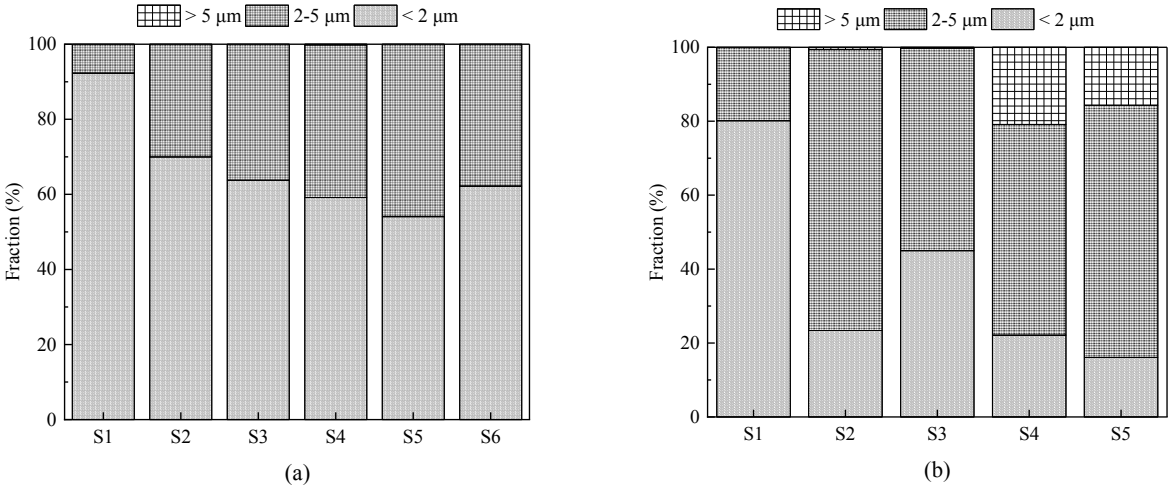

Figure 5. 5 The particle size distribution of AlN primary class for (a) 533N-P and (b) 533N-I steels.

The thermodynamic analysis and characteristics of observed AlN inclusions also suggest that at low N levels, AlN-MnS inclusions are formed. Moreover, medium and high N levels resulted in $AlN_{(pure)}$ inclusions. It could be inferred that AlN formed at the solidification front ended up having a composition of AlN-MnS, while the ones formed in liquid steel did not promote AlN-MnS formation; instead, they became $AlN_{(pure)}$ inclusions. This phenomenon was investigated by considering the effect of the cooling rate and presented in the following section.

5.4.2 Formation of AlN Inclusions during Solidification

Samples from bulk steel had been analyzed to study the behavior of AlN at the solidification front. The bulk samples were cooled at a slow cooling rate, i.e., 0.167 K/sec, as compared to 20-30 K/sec[31] of air-cooled pin samples. The obtained data were compared to the results of a previous study.[15] The data of the prior research was for steel containing Fe5Mn3Si3Al and < 10 ppm N. This steel was referred to as 533 steel in the current study. Figure 5.6 compares the fractions of different sub-classes of AlN inclusions observed in pin and bulk samples of 533N-P and 533 steel melts. For this comparison, the pin samples were taken before the cooling of bulk steel starts have been selected, i.e., the sample was taken at 300 minutes of holding time from 533N-P steel and at 41 minutes of holding time from 533 steel. The selection of these pin samples enabled a plausible comparison to their respective bulk samples as in both experiments, the bulk steel was exposed to similar holding time and cooling rates after these pin samples were taken.

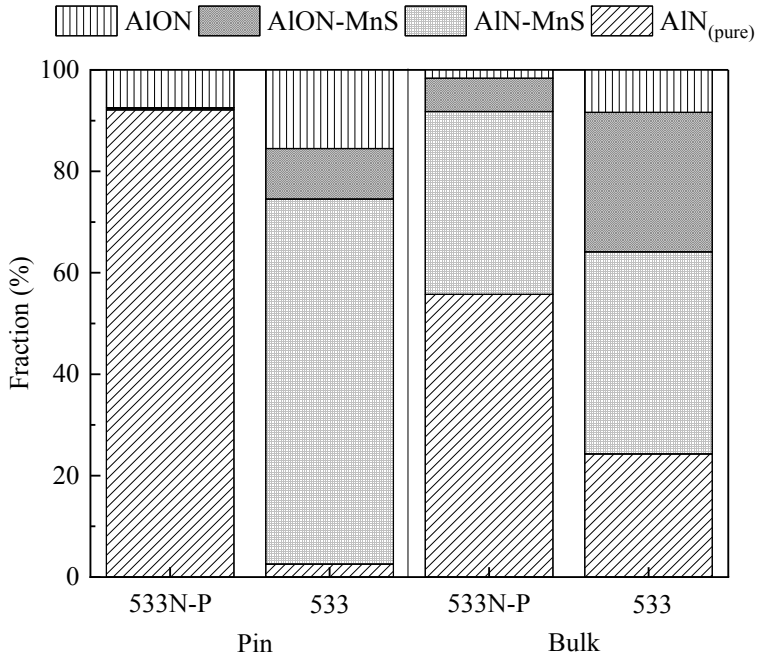

Figure 5. 6 The fraction of AlN subclasses in the pin and bulk samples of 533N-P and 533 steel melts.

As can be seen in Figure 5.6, $AlN_{(pure)}$ inclusions were the dominant sub-class (more than 90%) in the pin sample of 533N-P steel. Whereas, AlN-MnS made a significant portion (~80%) of AlN inclusions in 533 steel's pin sample, and the remaining were AlON (15%), AlON-MnS (5%), and a negligible amount of $AlN_{(pure)}$. The fraction of $AlN_{(pure)}$ inclusions decreased to ~60% in the bulk sample of 533N-P as compared to its respective pin sample. Moreover, a significant fraction (~30%) of AlN-MnS inclusions appeared in the bulk sample, and these inclusions were not present in the pin sample. On the contrary, in 533 steel melt, the slow cooling resulted in an increase (~20%) and a decrease (~30%) in the

percentage of $AlN_{(pure)}$ and AlN-MnS inclusions, respectively. It was interesting to see that despite a high N level in both pin and bulk samples of 533N-P steel, a substantial quantity of AlN-MnS inclusions was found in the slowly cooled bulk sample. Similarly, although 533 steel contained a low N level, its bulk sample had a considerable amount of $AlN_{(pure)}$ inclusions. To understand this and elucidate the formation behavior of $AlN_{(pure)}$ and AlN-MnS inclusions, two things needed to be considered: formation temperature of AlN and MnS, and capability of AlN and MnS to heterogeneously nucleate on each other.

Firstly, the formation temperature of AlN (T_{AlN}) and that of MnS (T_{MnS}), along with liquidus and solidus temperature of both 533N-P and 533 steel samples are given in Table 5.4. Secondly, it is known that AlN and MnS can co-precipitate together due to similarities in their crystal structures.[20] For co-precipitation, AlN can act as the nucleation site for MnS or MnS can act as the nucleation site for AlN.[1]

Table 5. 4 The temperature of liquidus, solidus, AlN, and MnS inclusion formation in the steel.

533N Steel Melt	N (%)	T_{AlN} (K)	T_{MnS} (K)	T_{liq} (K)	T_{sol} (K)
Low N	0.0002	1679.05	1472.78	1726.3	1611
Medium N	0.0023	1796.09	1473.89		
	0.0047	1865.39	1473.96		
High N	0.0054	1879.46	1473.97		

For low N level samples (533 steel), T_{AlN} was higher than T_{MnS} and lay between liquidus and solidus temperatures. AlN was formed at the solidification front, which was enriched in solute elements Al, N, Mn, and S. There was ~206 K difference between T_{AlN} and T_{MnS}. At a high cooling rate, the formation of AlN and MnS took place almost at the same time resulting in AlN-MnS inclusions. In the case of the bulk sample, the slow cooling rate facilitated the formation of $AlN_{(pure)}$ at an early stage of solidification (g_s value in the range of 0.71-0.11 for N < 10 ppm). This occurred before the liquid steel at the solidification front becomes enriched in Mn and S at a level that enabled MnS formation. However, the AlN inclusions formed at the end of solidification, closer to Mn and S segregated region, became sites for heterogeneous nucleation of MnS and eventually had a composition of AlN-MnS inclusions.

In the case of a pin sample from 533N-P, a higher difference (~405 K) between T_{AlN} and T_{MnS} resulted in the formation of a higher fraction of $AlN_{(pure)}$ inclusions. When this high N containing steel solidified at a slow rate, $AlN_{(pure)}$ inclusions formed in liquid steel at 1873 K until the start of solidification and at the early stage of solidification, and AlN-MnS inclusions formed at the end of solidification.

According to the above discussion and in section 5.4.1, the AlN-MnS should always form due to segregation at the end of solidification. The fraction of AlN-MnS inclusions appeared to be very low in the pin sample of 533N-P (Figure 5.6); however, as shown in Table 5.3, there was a similar amount (N_A) of AlN-MnS present in all the pin samples of 533N-P. It is to mention a scatter was observed in the (N_A) of AlN-MnS inclusions in the pin samples taken at different holding times during an experiment. This scatter could be caused by a difference in the mass of the sample, leading to some variation in the cooling rate of the individual pin sample. However, it appeared that the N content of steel did not influence the amount of AlN-MnS inclusions in samples taken during an experiment. For instance, the N_A value of AlN-MnS inclusions in low N sample (S1) of 533N-I was ~4.5 mm^{-2}, whereas S4 and S5 (high N samples) contained ~6.5 mm^{-2} and ~3 mm^{-2} of AlN-MnS inclusions. The (N_A) of AlN-MnS inclusions in low and high N samples (S1 and S4) of 533N-P was ~2 mm^{-2} and ~0.8 mm^{-2}, respectively. Hence, there was no apparent influence of N content on the amount of AlN-MnS inclusions. This was in agreement with the explanation that AlN-MnS inclusions were formed at solidification front enriched with Mn and S and that their amount depended on the cooling rate.

As mentioned, AlN and AlN-MnS inclusions were the common types of inclusions present in the current experimental steels. Few studies[32,33] focused on the influence of AlN and AlN-MnS inclusions on the mechanical properties of the steel. AlN inclusions could be found both inside the grain[34] or at the grain boundaries.[32,34] However, the AlN inclusions were reported to be more detrimental when they were located at the grain boundaries. Kang et al.[32] studied the hot ductility on the TWIP steels and observed that AlN inclusions precipitated at the austenite grain boundaries promoted the poor ductility of the steel. The AlN inclusions that precipitate at grain boundaries usually combine with MnS to form AlN-MnS due to the ease of co-precipitation of AlN and MnS to occur. Ushioda et al.[33] observed that AlN-MnS inclusion formed in the austenite grain boundaries in low carbon steel and reported that the complex precipitation of AlN and MnS is harmful to the hot ductility of the steel. The current study suggests that the N content of steel did not influence the amount of AlN-MnS inclusions. However, this inference is based on fast cooled pin samples and inclusions having a D_{ave} >2µm. In the case of slow-cooled samples, the N content of steel could influence the amount of AlN-MnS inclusions, i.e., a higher N content could result in a higher number of AlN-MnS inclusions especially considering that the AlN inclusions could be pushed to the solidification front during solidification of steel.

The formation of AlON and AlON-MnS took place as follows. First Al_2O_3 inclusions were formed in the liquid steel, as they were stable at 1873 K. It was followed by the formation of AlN inclusions when the N content in the steel was sufficient for AlN formation. AlON could be a result of AlN precipitation on Al_2O_3 or collision of AlN and Al_2O_3 particles. The precipitation of AlN on Al_2O_3 is possible, but on specific crystallographic orientations,[35] therefore, the number of observed AlON inclusions was small. Similar to AlN-MnS, the formation of AlON-MnS occurred during the solidification process, where either Al_2O_3 and/or AlN in AlON inclusion became the nucleation site for MnS inclusion.

5.4.3 Co-precipitation of Inclusions

In the current study, the formation of complex inclusions (AlN-MnS, Al_2O_3-MnS, and AlON) mostly occurred due to co-precipitation. The co-precipitation behavior can be quantified by considering precipitation ratio (PR) of one phase on another. The PR of phase 1 on phase 2 to form co-precipitates is defined as the ratio of the number of co-precipitates to the sum of the number of phase 2 particles and co-precipitates. The PR value is related to the potency of a phase to act as a heterogeneous nucleation site for others. In a previous study,[15] the authors compared the PR values of MnS on AlN and Al_2O_3 for the formation of AlN-MnS and Al_2O_3-MnS co-precipitates, respectively. It was reported that the PR value of MnS on AlN was always higher than that on Al_2O_3 due to a low mismatch between MnS and AlN (~5%)[36] as compared to that of MnS and Al_2O_3 (~12%).[36] However, that was based on low N containing steels. In the current study, it was observed that the PR values of AlN containing co-precipitates could be influenced by the N content of the steel.

Figure 5.7 shows a comparison of the PR values of MnS on AlN and Al_2O_3 observed in the previous study[171] (533 steel), which had low N content and the present study for 533N-P, which has low, medium, and high N containing samples. In the case of the PR value of MnS on AlN inclusions, in the low N content (533 and S1 of 533N-P), the PR value was more than 98%. However, in the medium (S2-S4) and high (S5 and S6) N containing samples, the PR values were significantly low, less than 15%. On the other hand, the PR values of MnS on Al_2O_3 were always less than 15% and were not influenced by the N content of the steel. It appeared that for samples having medium and high N content, the MnS PR values could be higher for Al_2O_3 as compared to for AlN. However, it should be noted that the lower PR values in medium and high N containing samples did not indicate that MnS prefers to nucleate on Al_2O_3. The lower MnS PR values on AlN were due to the formation of $AlN_{(pure)}$ in liquid steel.

The N content also influenced the PR values of AlN on Al_2O_3 to form AlON. Figure 5.8 shows the AlN PR values observed in 533[15] and 533N-P. The low N containing samples (533 and S1 from 533N-P) had PR values of less than 20%. As the N content in the steel increased (S2-S6), the PR values increased dramatically to over 80%. This implied that more AlN inclusions were available to co-precipitate with $Al_2O_{3(pure)}$ to form AlON inclusion.

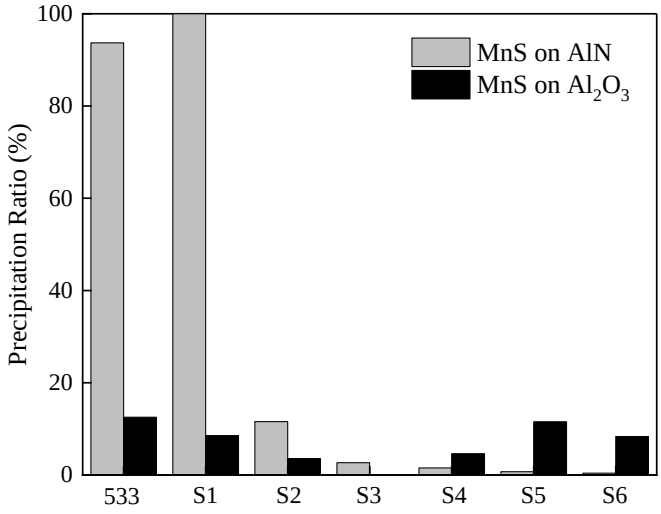

Figure 5. 7 A comparison of the MnS precipitation ratio (PR) values for AlN and Al_2O_3 inclusions.

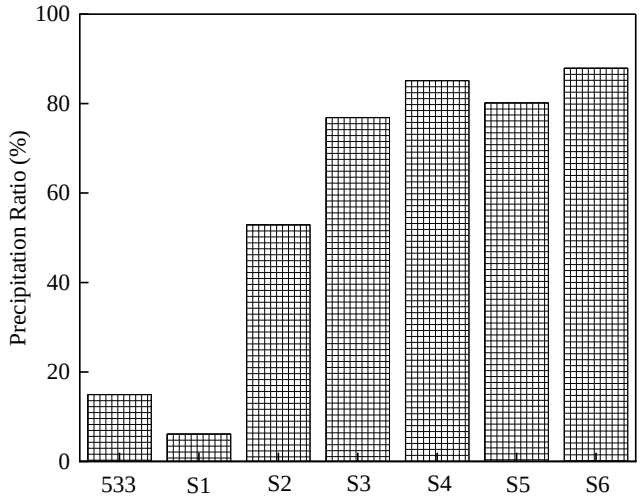

Figure 5. 8 The precipitation ratio (PR) value for AlN on $Al_2O_{3(pure)}$ inclusions on 533N-P steels.

5.4.4 Effect of N Content on the Morphology of $AlN_{(pure)}$ Inclusions

In this study, the $AlN_{(pure\ )}$ inclusions were classified into five types based on their morphology, as displayed in Table 5.5. The inclusions having 5 or 6 sides were grouped as a plate-like type, and those with 3 or 4 sides were classified as angular. The inclusions exhibiting a long and thin morphology were grouped as a needle-like type. Agglomerates represented inclusions that consist of two or more particles. The remaining inclusions had irregular morphology.

Table 5. 5 Morphology of $AlN_{(pure)}$ inclusions

Plate-like	Angular	Needle	Agglomerate	Irregular
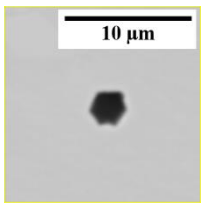	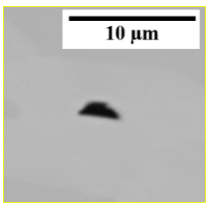	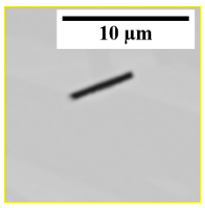	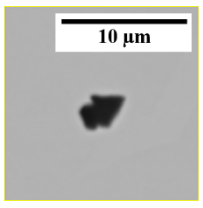	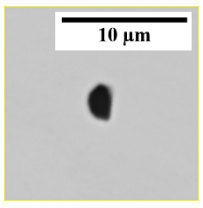

The low N containing sample (S1) from 533N-P did not contain any $AlN_{(pure)}$ inclusions, and that from 533N-I contained only 4 $AlN_{(pure)}$ inclusions, which were all angular. The morphology of $AlN_{(pure)}$ inclusions observed in the medium and high N containing samples of both steel melts was shown in Figure 5.9(a) and 5.9(b), respectively. In 533N-P samples, around 70% of $AlN_{(pure)}$ inclusions have angular morphology. A small fraction (~ 6%) of inclusions with needle shape was found in samples containing medium N levels (S3 and S4). The number of plate-like inclusions was relatively higher in high N samples, i.e., around 14-18%, as compared to 8-9% in medium N samples. Approximately 6-13% inclusions were agglomerate, while irregular morphology makes 4-13%. In the case of 533N-I steel samples, plate-like morphology was a dominating type (36-60%). It was followed by an angular type that is around 26-36%. The fraction of agglomerate inclusions increased from 11 to 32% with increased holding time (S2 to S4) and then decreased to 19% in sample S5. The needle and irregular shaped inclusions were present in small amounts, i.e., 4-10% and ~ 2%, respectively.

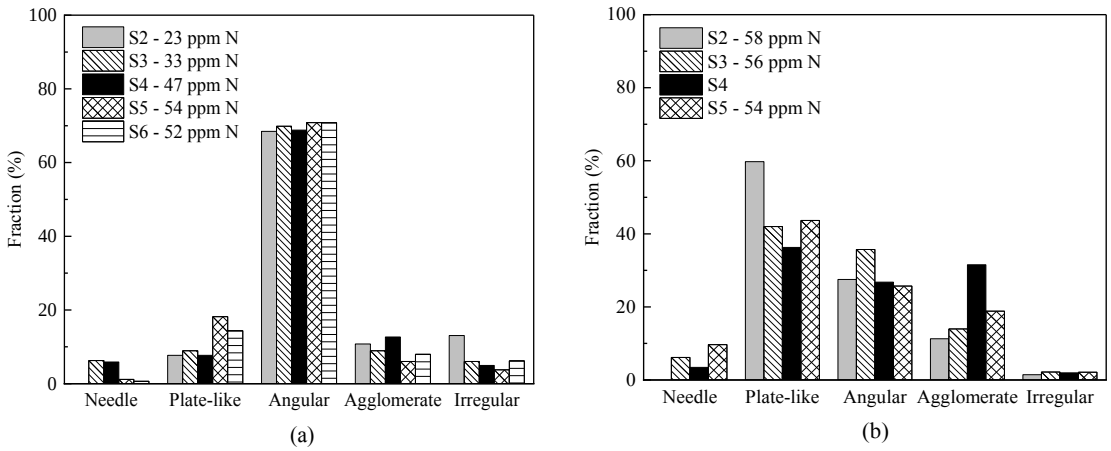

Figure 5. 9 The fraction of morphology of $AlN_{(pure)}$ inclusions in (a) 533N-P and (b) 533N-I steel melts.

It is of interest to observe a higher fraction of plate-like inclusions in samples with high N content. It could be related to the stability of AlN at 1873 K for high N containing samples. The effect of N content was observed in both experimental steel melts; moreover, the fraction of plate-like inclusions in 533N-I was significantly higher than that observed in S5 and S6 of 533N-P steel. This could be due to fast kinetics conditions in this steel. The turbulent conditions could lead to a faster growth rate of inclusions, enabling them to be detected under settings of current inclusion analysis (D_{ave} > 2 um).

Moreover, a few samples were electrolytically etched in a 10% AA (10 v/v% acetylacetone - 1 w/v% tetramethylammonium chloride - methanol) electrolyte to expose three-dimensional morphology of inclusions. It was found that a considerable number of AlN inclusions were oriented at different angles to the analyzed surface. Such orientation of plate-like inclusions could make them appear as angular inclusions on a two-dimensional surface. Figure 5.10 shows examples of such inclusions. It was clear from secondary electron images (SEI) (Figure 5.10(a)) that the observed inclusions are, in fact, plate-like in shape. While from the back-scattered electron (BSE) images (Figure 10(b)), they could be defined as angular inclusions, especially if the surface had been polished.

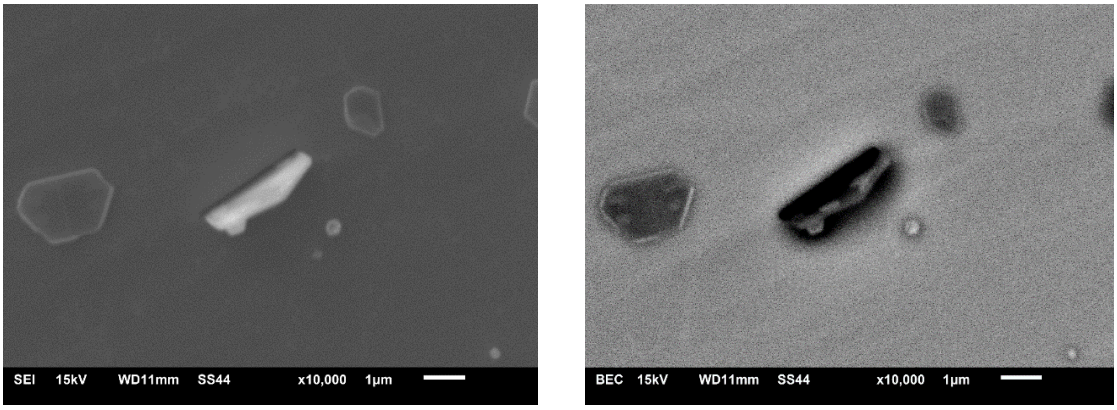

(a) (b)

Figure 5. 10 (a) SEI and (b) BSE images of AlN inclusions which are positioned in a different angle.

Applying the same reasoning, it could be argued that there is a possibility that inclusions with needle morphology could also be plate-like when observed in three-dimensions. To clarify this, the maximum diameter (D_{max}) of plate-like and needle inclusions observed in S4 and S5 of 533N-P steel was compared and shown in Figure 5.11. It could be seen that the D_{max} values of plate-like inclusion varied from 1 to 5 μm (Figure 5.11(a)). Whereas needle-shaped inclusions had D_{max} values in the range of 3 to 10 μm, and more than 90% of them were larger than 5 μm (Figure 5.11(b)). It is evident from Figure 11 that needle-shaped inclusions were not plate-like inclusions oriented at an angle as the D_{max} values of needle-shaped inclusions were significantly higher than those of plate-like inclusions.

Based on Figure 5.9 through Figure 5.11, AlN inclusions were detected in various morphologies. A similar observation was made by previous researchers.[3,4,9,20] Tuling and Mintz[20] investigated the morphology of AlN inclusions in high Al transformation induced plasticity (TRIP) steels with 2.5% Mn, 60-70 ppm N, and 1%-1.5% Al. According to the thermodynamics, AlN inclusions were formed during solidification for both 1% and 1.5% Al containing TRIP steels. Dendritic and hexagonal (plate-like) AlN inclusions were observed in steel with 1% Al and 1.5% Al, respectively. Liu et al.[4] reported plate-like morphology of single AlN inclusions in the twin-induced plasticity (TWIP) steel (Fe-18Mn-1.5Al with 78 ppm N) and suggested that these AlN inclusions were formed above the T_{liq} of the investigated steel. Wang et al.[3] detected fine particles of AlN inclusions at the grain boundaries of TWIP steel (Fe-16Mn-0.54Al) with 63 ppm N content and coarse hexagonal (plate-like) AlN particles at the fracture site of TWIP steel (Fe-17Mn-2.1Al) with 43 ppm N content. For both these compositions of steel, thermodynamically AlN should form during solidification i.e., below the T_{liq}. Moreover, Kang et al.[9] suggested that the presence of MnS inclusions can affect the morphology of AlN inclusions. They observed AlN inclusions in high Al TWIP steel (Fe-18Mn-1.5Al and 80-93 ppm N) with different sulfur content. It was reported that in the absence of MnS inclusions i.e., when the steel had 32 ppm S, the AlN inclusions had hexagonal (plate-like) shape. In case of an abundance of MnS (S content up to 100-230 ppm), AlN inclusions exhibited dendritic and hexagonal (plate-like) morphologies. Based on thermodynamics, AlN inclusions would have formed during solidification for all the compositions investigated by Kang et al.[9]. From the above mentioned literature it can be seen that AlN inclusions can exhibit various morphologies regardless of whether they are formed during solidification or above T_{liq}. Similar behavior is observed in the current study. A three-dimensional inclusion analysis is recommended for further investigation.

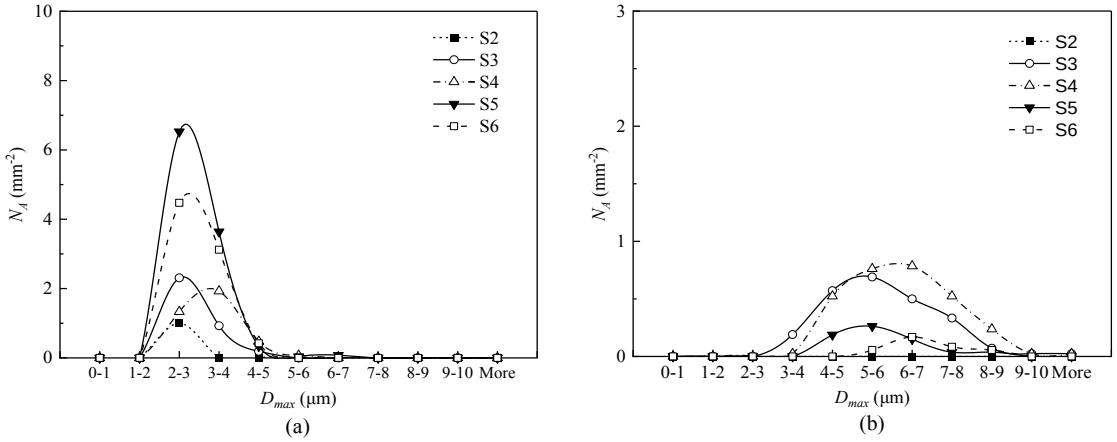

Figure 5. 11 The size distribution of the AlN inclusions with (a) the plate-like and (b) needle shape in 533N-P steel samples.

5.5 Conclusions

The influence of N content on the characteristics of inclusions in Fe-5Mn-3Al-3Si steel was investigated in the current study. N was added into liquid steel by purging the N_2 gas into the atmosphere of a sealed furnace containing molten steel or by directly injecting N_2 gas into the molten steel. The steel compositions were divided into three groups based on their N levels, i.e., low N (<10 ppm), medium N (23-47 ppm), and high N (> 50 ppm) containing steels. The following findings are obtained.

1. A high N content of steel can be achieved in a short time by injection of N_2 gas into the melt.

2. The number of inclusions increased from ~13 mm^{-2} to ~64 mm^{-2} as N content increased from low to medium level, as observed in 533N-P steels. The number of inclusion remained constant by a further increase in N content. However, in the case of 533N-I steels, the number of inclusion increased up to 108 mm^{-2} at the high level of N content.

3. In low N content steel, AlN-MnS inclusions were dominating class (40-60% of the total inclusions). While in medium and high N content steel samples, $AlN_{(pure)}$ inclusions are the primary class of inclusions (50-90% of the total inclusions).

4. The number of AlN-MnS inclusions is not affected by the N content of steel as they are formed during solidification. However, the cooling rate has an influence on their number.

5. The amount of Al_2O_3 inclusions decreases with an increase in the N content of the steel. Low N samples contained 10 mm^{-2} of Al_2O_3 inclusions, which decreased to 2 mm^{-2} and 1 mm^{-2} in medium and high N containing samples, respectively.

6. AlN inclusions exhibit different morphologies such as plate-like, needle-like, angular, and agglomerates. Three-dimensional observation of angular AlN inclusions showed that they could be plate-like inclusions which are positioned at different orientations, making them appear angular.

7. Since the morphological information can be misinterpreted in a two-dimensional observation, a three-dimensional inclusion analysis is recommended for detailed morphological investigation of AlN inclusions.

5.6 Acknowledgments

The authors would like to express gratitude to Dr. Stanley Sun and Ms. Li Sun at ArcelorMittal Dofasco for her valuable time and fruitful discussions. Further, we also want to thank the Canadian Centre for Electron Microscopy (CCEM) to provide access to the JEOL 6610 to conduct the scanning electron microscopy analysis.

5.7 References

1. Hu, B.; Luo, H.; Yang, F.; Dong, H. Recent progress in medium-Mn steels made with new designing strategies, a review. J. Mater. Sci. Technol. 2017, 33, 1457–1464.
2. Steenken, B.; Rezende, J.L.L.; Senk, D. Hot ductility behaviour of high manganese steels with varying aluminium contents. Mater. Sci. Technol. 2017, 33, 567–573.
3. Wang, Y.-N.; Yang, J.; Wang, R.-Z.; Xin, X.-L.; Xu, L.-Y. Effects of Non-metallic Inclusions onHot Ductility of High Manganese TWIP Steels Containing Different AluminumContents. Metall. Mater. Trans. B 2016, 47, 1697–1712.
4. Liu, H.; Liu, J.; Wu, B.; Shen, Y.; He, Y.; Ding, H.; Su, X. Effect of Mn and Al contents on hot ductility of high alloy Fe-xMn-C-yAl austenite TWIP steels. Mater. Sci. Eng. A 2017, 708, 360–374.
5. Kong, L.; Deng, Z.; Zhu, M. Formation and Evolution of Non-metallic Inclusions in Medium Mn Steel during Secondary Refining Process. ISIJ Int. 2017, 57, 1537–1545.
6. Yu, Z.; Liu, C. Modification mechanism of spinel inclusions in medium manganese steel with rare earth treatment. Metals (Basel) 2019, 9, 804.
7. Grajcar, A.; Wo´zniak, D.; Kozłowska, A. Non-Metallic Inclusions and Hot-Working Behaviour of Advanced High-Strength Medium-Mn Steels. Arch. Metall. Mater. 2016, 61, 811–820.
8. Yu, Z.; Liu, C. Evolution Mechanism of Inclusions in Medium-Manganese Steel by Mg Treatment with Different Aluminum Contents. Metall. Mater. Trans. B Process Metall. Mater. Process. Sci. 2019, 50, 772–781.
9. Kang, S.E.; Banerjee, J.R.; Mintz, B. Influence of S and AlN on hot ductility of high Al, TWIP steels. Mater. Sci. Technol. 2012, 28, 589–596.
10. Thornton, P.A. The influence of nonmetallic inclusions on the mechanical properties of steel: A review. J. Mater. Sci. 1971, 6, 347–356.
11. Maciejewski, J. The Effects of Sulfide Inclusions on Mechanical Properties and Failures of Steel Components. J. Fail. Anal. Prev. 2015, 15, 169–178.
12. Ånmark, N.; Karasev, A.; Jönsson, P. The Effect of Different Non-Metallic Inclusions on the Machinability of Steels. Materials (Basel) 2015, 8, 751–783.
13. Tomita, Y. Effect of morphology of nonmetallic inclusions on tensile properties of quenched and tempered 0.4C-Cr-Mo-Ni steel. Mater. Charact. 1995, 34, 121–128.
14. Alba, M.; Nabeel, M.; Dogan, N. Investigation of Inclusion Formation in Light-Weight Fe–Mn–Al Steels using Automated Scanning Electron Microscope Equipped with Energy-Dispersive X-Ray Spectroscopy. Steel Res. Int. 2019, 91, 1900477.
15. Alba, M.; Nabeel, M.; Dogan, N. Effect of aluminium content on the formation of inclusions in Fe–5Mn–xAl steels. Ironmak. Steelmak. 2020.
16. Paek, M.-K.; Jang, J.-M.; Do, K.-H.; Pak, J.-J. Nitrogen Solubility in High Manganese-Aluminum Alloyed Liquid Steels. Met. Mater. Int. 2013, 19, 1077–1081.
17. Jang, J.-M.; Paek, M.-K.; Pak, J.-J. Thermodynamics of Nitrogen Solubility and AlN Formation in Multi-Component High Mn Steel Melts. ISIJ Int. 2017, 57, 1821–1830.

18. Liu, H.; Liu, J.; Michelic, S.K.; Wei, F.; Zhuang, C.; Han, Z.; Li, S. Characteristics of AlN inclusions in low carbon Fe–Mn–Si–Al TWIP steel produced by AOD-ESR method. Ironmak. Steelmak. 2016, 43, 171–179.
19. Xin, X.L.; Yang, J.; Wang, Y.N.; Wang, R.Z.; Wang, W.L.; Zheng, H.G.; Hu, H.T. Effects of Al content on non-metallic inclusion evolution in Fe–16Mn– x Al–0.6C high Mn TWIP steel. Ironmak. Steelmak. 2016, 43, 234–242.
20. Tuling, A.; Mintz, B. Crystallographic and morphological aspects of AlN precipitation in high Al, TRIP steels. Mater. Sci. Technol. 2016, 32, 568–575.
21. Liu, H.; Liu, J.; Michelic, S.K.; Shen, S.; Su, X.; Wu, B.; Ding, H. Characterization and Analysis of Non-Metallic Inclusions in Low-Carbon Fe-Mn-Si-Al TWIP Steels. Steel Res. Int. 2016, 87, 1–10.
22. Hsiao, C. Fine Aluminium Nitride Precipitates in Steel. Nature 1958, 181, 1527–1528. [CrossRef] 23. Wilson, F.G.; Gladman, T. Aluminium nitride in steel. Int. Mater. Rev. 1988, 33, 221–286.
23. Wilson, F.G.; Gladman, T. Aluminium nitride in steel. Int. Mater. Rev. 1988, 33, 221–286.
24. Li, X.; Wang, M.; Bao, Y.; Gong, J.; Wang, X.; Pang, W. Precipitation Behavior of AlN in High-Magnetic-Induction Grain-Oriented Silicon Steel Slab. JOM 2019, 71, 3135–3141.
25. Croft, N.H.H.; Entwisle, A.R.R.; Davies, G.J.J. Origins of dendritic AlN precipitates in aluminium-killed-steel castings. Met. Technol. 1983, 10, 125–129.
26. LECO Corp. Oxygen and Nitrogen Determination in Refractory Metals and Their Alloys; LECO Corporation: Saint Joseph, MI, USA, 2020; pp. 1–2.
27. LECO Corp. Carbon and Sulfur Determination in Low Carbon Ferroalloys; LECO Corporation: Saint Joseph, MI, USA, 2018; pp. 1–3.
28. FEI. ASPEX Explorer-Automated Industrialized SEM with OmegaMax EDX Technology; FEI Company: Fremont, CA, USA, 2014; pp. 1–2.
29. Paek, M.; Jang, J.; Jiang, M.; Pak, J. Thermodynamics of AlN Formation in High Manganese-Aluminum Alloyed Liquid Steels. ISIJ Int. 2013, 53, 973–978. [CrossRef]
30. Nabeel, M.; Alba, M.; Karasev, A.; Jönsson, P.G.; Dogan, N. Characterization of Inclusions in 3rd Generation Advanced High-Strength Steels. Metall. Mater. Trans. B 2019, 50, 1674–1685. [CrossRef]
31. Ericsson, O.T.; Lionet, M.; Karasev, A.V.; Inoue, R.; Jönsson, P.G. Changes in inclusion characteristics during sampling of liquid steel. Ironmak. Steelmak. 2011, 39, 67–75.
32. Kang, S.E.; Tuling, A.; Banerjee, J.R.; Gunawardana, W.D.; Mintz, B. Hot ductility of TWIP steels. Mater. Sci. Technol. 2011, 27, 95–100.
33. Ushioda, K.; Suzuki, H.G.; Komatsu, H.; Esaka, K. Influence of sulfur on AlN precipitation during cooling after solidification and resulting hot shortness in low carbon steel. Nippon Kinzoku Gakkaishi J. Jpn. Inst. Met. 1995, 59, 373–380.

34. Chen, Y.-L.; Wang, Y.; Zhao, A.-M. Precipitation of AlN and MnS in Low Carbon Aluminium-Killed Steel. J. Iron Steel Res. Int. 2012, 19, 51–56.
35. Li, F.; Li, H.; Huang, D.; Zheng, S.; You, J. Mechanism of MnS Precipitation on Al2O3–SiO2 Inclusions in Non-oriented Silicon Steel. Met. Mater. Int. 2018, 24, 1394–1402.
36. Ohta, H.; Suito, H. Precipitation and Dispersion Control of MnS by Deoxidation Products of ZrO2, Al2O3, MgO and MnO–SiO2 Particles in Fe–10mass%Ni Alloy. ISIJ Int. 2006, 46, 480–489.

Chapter 6

Precipitation Mechanism of (Ca,Mn)S with AlN Inclusions

6.1 Introduction

As investigated in previous chapters, the inclusions that are formed in medium manganese steel and high manganese steel are primarily AlN-containing inclusions. These inclusions can be harmful to steel production because their presence leads to poor hot ductility.[4] As mentioned previously, AlN inclusions can form both in the liquid steel and during the solidification of steel, depending on the N content of the steel. Moreover, AlN inclusions can co-precipitate with other inclusions, for example, MnS, and form AlN-MnS inclusions.[1,114] In the secondary steelmaking process, adding Ca is a common approach for modifying the composition of oxide inclusions[117] and controlling the shape of sulfide inclusions.[172] It is possible that MnS in AlN-MnS inclusions can react with Ca to form a (Ca,Mn)S phase as MnS and CaS both can form a (Ca,Mn)S solid solution.[173–175]

This brief chapter investigates the effect of Ca addition on characteristics of inclusions in medium manganese steel with emphasis on modification of AlN inclusions. For this purpose, two experiments were conducted, and thermodynamic calculations were carried out to study the stability of inclusions at experimental temperature.

6.2 Experimental

Two synthetic steel melts (300 grams) containing Fe-5Mn-3Al-3Si-0.1C were produced by using a resistance heating vertical furnace.

Experiment 1. Fe-5Mn-3Al-3Si-0.1C steel with Ca addition (533-Ca steel): the furnace chamber was evacuated after the temperature reached 1873 K (1600°C) and backfilled with Ar gas. Then the calcium particles (~0.48 gr) and Fe electrolytic (~3.3-3.5 gr) encapsulated in Fe foil were added into the steel melt. Steel samples were taken before and after the addition of calcium at different holding times, as shown in Figure 6.1(a).

Experiment 2. Fe-5Mn-3Al-3Si-0.1C steel with both Ca addition and N injection (533N-I-Ca steel): a similar experimental procedure (as 533-Ca) was adopted. In addition, N_2 gas was injected into the steel melt after the addition of Ca. The sampling timeline for 533N-I-Ca is given in Figure 6.1(b).

All the samples were analyzed for their oxygen-nitrogen content with LECO O/N (ON736) and carbon-sulfur content with LECO C/S (CS744) analyzer. Calcium, manganese, aluminum, and silicon contents were analyzed by Induction Coupled Plasma Optical Emission Spectrometry (ICP-OES). The inclusion analysis was conducted by an automated SEM equipped with the ASPEX feature. For these Ca-containing steels, elemental Ca was

included in earlier used inclusion classification rules (presented in Chapter 3) to classify Ca-containing inclusions.

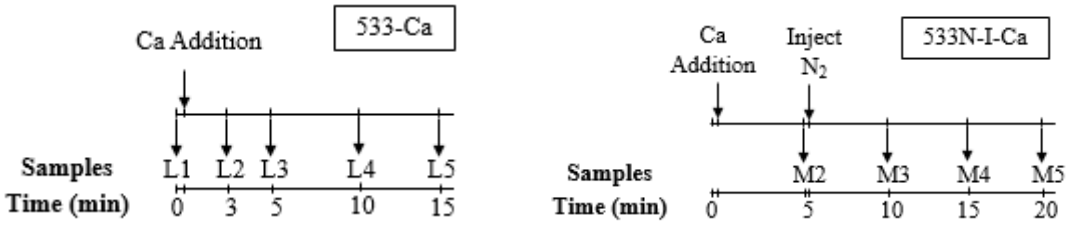

(a) (b)

Figure 6. 1 Experimental steps.

6.3 Results and Discussion

The compositions of experimental steel melts are listed in Table 6.1. The concentrations of Mn, Al, Si, C, and S were constant during the experiments. In 533-Ca steels, the initial Ca content in the steel (sample L1) was about 4 ppm. After Ca addition, the Ca content was increased to the targeted value of around 20 ppm and was almost stable except in the L3 sample, which was slightly lower. It was most likely due to the time required for the homogenization of Ca after the addition. In the 533N-I-Ca steel, the fluctuation of Ca content could be due to turbulence generated by the injection of N_2 gas. The average Ca content in 533-Ca and 533N-I-Ca steels after the addition was ~ 23 ppm.

There were some missing values for N and O contents in 533-Ca steel due to insufficient material to be analyzed. Since there was no addition of N in the 533-Ca steel, the N content in this steel should always be low. Even though an attempt was made to obtain a sample before Ca addition, M1 during Experiment 2 (533N-I-Ca steel), the sampling was unsuccessful. It should be noted that the chemical composition of this sample is expected to be similar to L1 in 533-Ca steel since the initial conditions are the same. Moreover, before the injection of N_2 gas, the N content was 5 ppm (M2 sample). After the N_2 injection, the N content of the M3 steel sample was significantly high. This value was decreased with time as the bath became homogenized. The high O content in the L2 sample in 533-Ca could be due to some air introduced while adding Ca from the top of the furnace. The O content in 533N-I-Ca steel was relatively high due to the oxygen impurities in the N_2 gas.

Table 6. 1 The chemical composition of 533-Ca and 533N-I-Ca steels.

Steel Set	Mn (%)	Al (%)	Si (%)	C (%)	S (ppm)	Ca (ppm)	N (ppm)	O (ppm)	Time (min)	Sample
533-Ca	5.03	2.61	2.44	0.101	25.6	4	-	-	0	L1
						24	2	21	3	L2

						18	-	-	5	L3
						23	3	1	10	L4
						27	-	-	15	L5
533N-I-Ca	4.69	2.63	2.99	0.105	19.3	21	5	7	0	M2
						23	92	18	5	M3
						15	74	16	10	M4
						32	68	6	15	M5

The steel composition in Table 6.1 was used for the thermodynamic calculations to predict the stable inclusions in the 533-Ca (Ca = 23, N = 3, O = 10 ppm) and 533N-I-Ca (Ca = 23, N = 78, O = 13 ppm) by using FactSage 8.0 (Fsstel, FToxid, and FactPS). The stable inclusions at 1873 K for 533-Ca steel were liquid calcium aluminate and CaS (Figure 6.2(a)). As the temperature decreased, other calcium aluminate inclusions such as CA, CA_2, and CA_6 were formed (C stands for CaO and A stands for Al_2O_3). Figure 6.2(b) shows the thermodynamic calculations for 533N-I-Ca steel. At 1873 K, the stable inclusions were liquid calcium aluminate, CaS, and AlN inclusions. Similar to 533-Ca steel, as the temperature decreases during cooling, CA, CA_2, and CA_6 were formed.

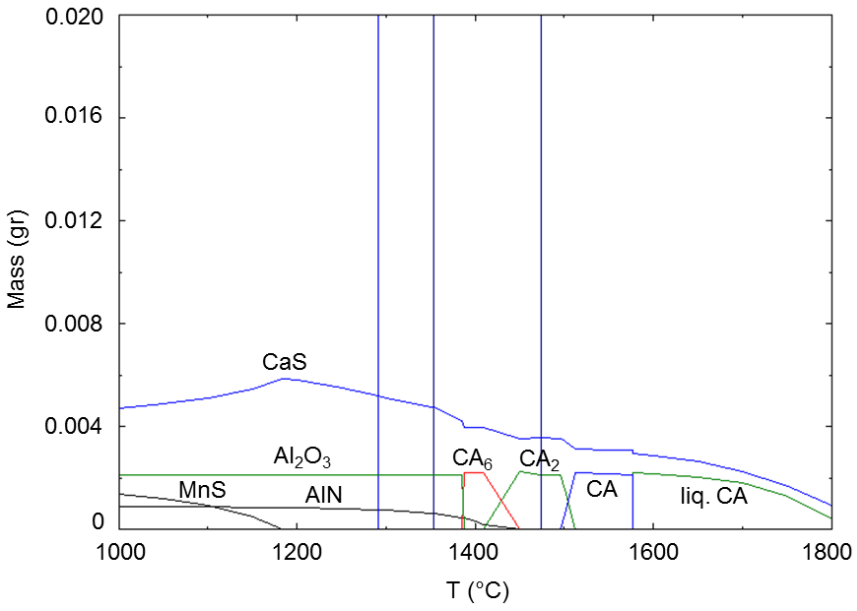

(a)

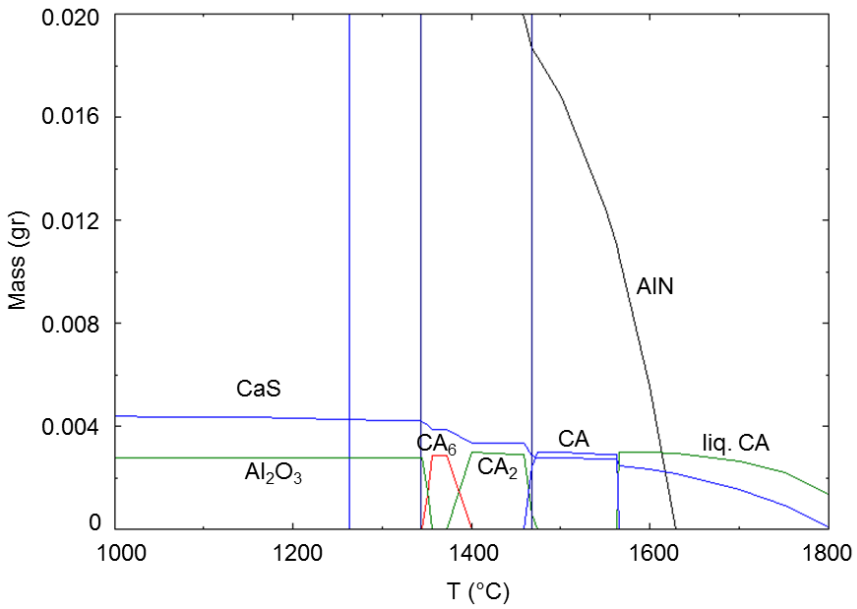

Figure 6. 2 Thermodynamic calculation of (a) 533-Ca and (b) 533N-I-Ca steel melts at 1873 K using FactSage 8.0.

Figure 6.3 shows the number per unit area (N_A) of different types of inclusions. In 533-Ca, the total number of inclusions was initially around 10 mm^{-2} (Figure 6.3(a)). After Ca addition, the total number of inclusions gradually increased, and it reached approximately 47 mm^{-2} at 15 minutes of holding time (the L5 sample). Al_2O_3 (N_A = 6 mm^{-2}), and AlN (N_A = 3 mm^{-2}) inclusions were present initially. After the addition of Ca, Ca-containing inclusions started to form, such as CAx and CaS-Other inclusions. The CAx inclusions included all calcium and alumina-containing inclusions regardless of the presence of nitride in them. Similarly, CaS-Other inclusions included all calcium sulfide-containing inclusions, either CaS or combined with oxide and/or nitride inclusions on it. The number of CAx inclusions increased with time from 2 to 5 $mm^{-2,}$ and that of CaS-other inclusions also increased from 6 to 27 mm^{-2}.

In 533N-I-Ca (Figure 6.3(b)), after the addition of Ca, the total number of inclusions was around 7 mm^{-2}. The steel mostly contained CAx and CaS-Other inclusions with an amount of 2 and 3 mm^{-2}, respectively. After the injection of N_2 gas, the total number of inclusions drastically increased to N_A = 108 mm^{-2}. There was a variation in the total number of inclusions with time. It is probably due to the inhomogeneity of the melt just after the injection of N_2 gas. AlN inclusion became the dominant type of inclusion. Furthermore, the number of CAx inclusions decreased, but the number of CaS-Other slowly increased to 5 mm^{-2} after 15 minutes of injection of N_2 gas (the M5 sample).

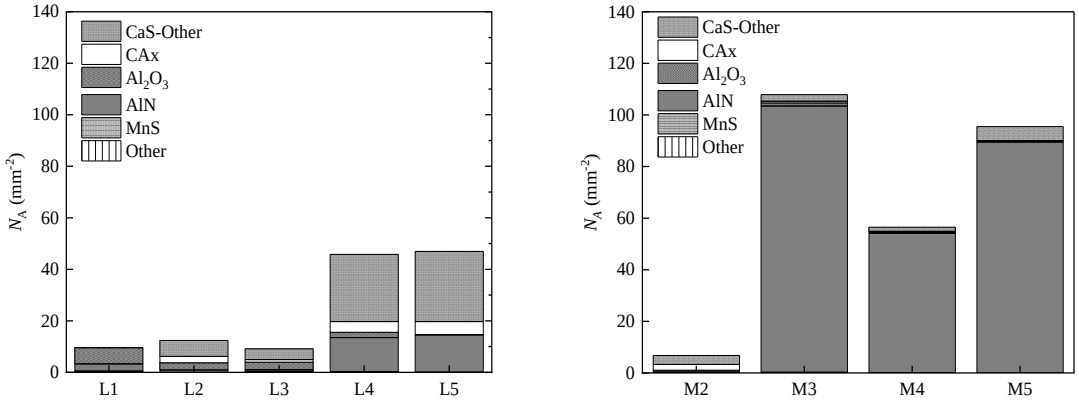

(a) (b)

Figure 6. 3 The total number and type of inclusions in (a) 533-Ca and (b) 533N-I-Ca steel melts.

The CaS-Other inclusions were classified into three sub-classes, i.e., (Ca,Mn)S, (Ca,Mn)S-Nitride, and (Ca,Mn)S-Oxide inclusions. Due to relatively high Mn content, Mn was always detected in CaS-Other inclusions. Thus, no pure CaS inclusions were observed. Figure 6.4 shows the number of CaS-Other inclusions in both 533-Ca and 533N-I-Ca steel melts. It can be seen that more than 92% of the CaS-Other inclusions were (Ca,Mn)S-Nitride or (Ca,Mn)S-Oxide, whereas the percentage of (Ca,Mn)S was really low in both melts. In the 533-Ca steel (Figure 6.4(a)), after the addition of Ca (L2 sample), (Ca,Mn)S-Oxide inclusions were the dominant inclusions (N_A = ~5 mm^{-2}), and few (Ca,Mn)S-Nitride inclusions were detected (N_A < 2 mm^{-2}). Then, the N_A of (Ca,Mn)S-Nitride inclusions (N_A = 20 mm^{-2}) was three times more than that of (Ca,Mn)S-Oxide inclusions (L5 sample). A similar trend was also shown in Figure 6.4(b). After the addition of Ca (M2 sample), (Ca,Mn)S-Oxide became a dominant inclusion (N_A = 3 mm^{-2}). With the injection of N_2 gas, the formation of (Ca,Mn)S-Nitride inclusions started. Their N_A value increased to 5 mm^{-2} after 15 minutes of N_2 gas injection (M5 sample). A possible reason for the lower number of CaS-Other inclusions in 533N-I-Ca steel could be related to the higher N content of the steel. In this steel, AlN was stable in liquid steel and existed as $AlN_{(pure)}$, and as discussed in Chapter 5, $AlN_{(pure)}$ particles did not participate in co-precipitation. The difference in the number of CaS-Other inclusions could be due to different process conditions involved in both experiments, and they also could form as solidification products. In addition, the lower N_A value of CAx and CaS-Other in 533-I-Ca than 533-Ca steel is due to the turbulence from the injection of N_2 gas in 533-I-Ca, which promotes inclusions that float up to the steel surface.

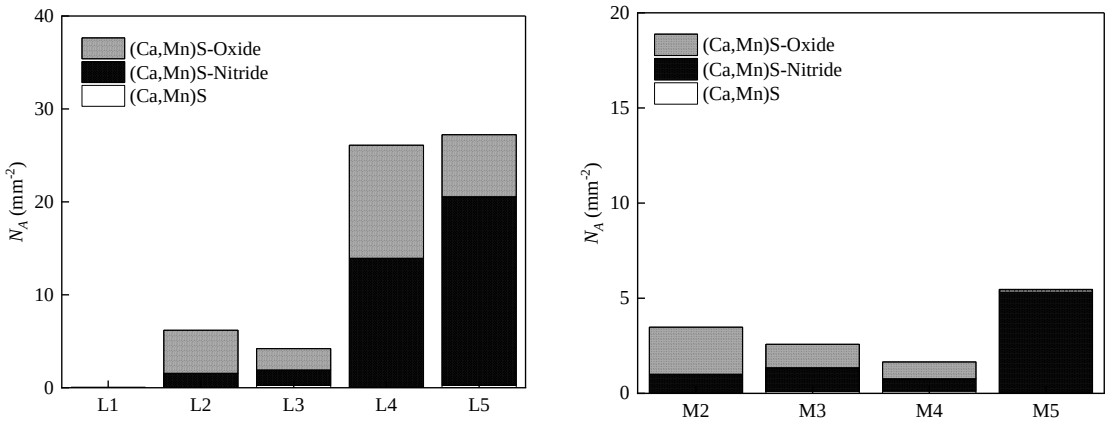

(a) (b)

Figure 6. 4 The number of (Ca,Mn)S-contained inclusions in (a) 533-Ca and (b) 533N-I-Ca steel melts.

6.4. Co-precipitation of Inclusions

It is known that CaS and MnS inclusions can form a solid solution in steel.[175] Moreover, they can also precipitate during solidification. The presence of other types of inclusions, such as Al_2O_3 and AlN, makes it possible for both CaS and MnS inclusions to co-precipitate and form complex inclusions. The possibility of two inclusions to co-precipitate as a result of heterogeneous nucleation can be determined by calculating the lattice misfit between the crystal structures of two inclusions. Table 6.2 lists the lattice parameters and the crystal structures of inclusions detected in the current steel composition. The data in Table 6.2 is used to calculate the misfit by applying Equation (6.1) below.[115]

Table 6. 2 List of lattice parameter and the crystal structure of inclusions.[114,115,176,177]

Inclusion	a (nm)	c (nm)	Crystal Structure
MnS	0.52	0.52	Cubic
AlN	0.31	0.49	HCP
CaS	0.57	0.57	Cubic
Al_2O_3	0.48	1.30	Rhombic

$$Misfit = \frac{|a_n - a_s|}{a_s} \times 100\% \quad (6.1)$$

where a_n and a_s are the lattice parameters of the nucleated inclusion and substrate, respectively. The calculated misfit between two types of inclusions is listed in Table 6.3. For AlN, the 'c' lattice parameter is used in misfit calculations because it is almost similar to the lattice of other inclusions, which provide the preferential co-precipitation site. Zhang and Kelly[178] reported that the interatomic spacing misfit should be less than 10% for two

crystal structures to have the minimum strain energy and precipitate together. Moreover, Bramfitt[110] also analyzed that the misfit (or disregistry) between the nucleated solid and substrate inclusion should be less than 12% to be ideal for the nucleation site. Based on previous criteria, Table 6.3 shows that the misfit between CaS and MnS, and between AlN and MnS is less than 10%, whereas the misfit between CaS and AlN, and between CaS and Al_2O_3 is more than 14%. These values imply that the co-precipitation of CaS and MnS is relatively easier than the co-precipitation of CaS and AlN, and CaS and Al_2O_3. These values are in agreement with the result of the previous researchers.[113] Ohta and Suito[113] calculated the misfit parameter of various inclusions with MnS and reported that the misfit between CaS and MnS is 8% and between AlN and MnS is 6-9%. Tuling and Mintz[114] mentioned that although AlN and MnS do not have a similar crystal structure, they can co-precipitate because the 'c' lattice of hcp crystal of AlN is almost identical to the lattice of cubic crystal of MnS.

Table 6. 3 Calculated interatomic spacing misfit of inclusions

Nucleated Inclusion	Substrate	Misfit (%)
MnS	CaS	8.77
CaS	MnS	9.61
CaS	AlN	16.33
AlN	CaS	14.03
MnS	AlN	6.12
AlN	MnS	5.77

6.4.1 Formation of (Ca,Mn)S-Nitride Inclusions

It is apparent from Table 6.3 that AlN and CaS cannot co-precipitate. However, the ease of co-precipitation of MnS with AlN and CaS can result in complex (Ca,Mn)S-Nitride inclusions. The formation of (Ca,Mn)S-Nitride inclusions could occur as follows:

1. AlN-MnS co-precipitates during solidification of steel, and then CaS nucleates, collides, or dissolves in the MnS phase of AlN-MnS inclusions.
2. CaS-MnS forms due to heterogeneous nucleation and its MnS phase co-precipitates with AlN.
3. A solid solution of CaS and MnS precipitates on AlN inclusions.

6.4.2 Formation of (Ca,Mn)S-Oxide Inclusions

For both compositions, liquid calcium aluminates are formed in liquid steel. It is reported that CaS has some solubility in these liquid inclusions, which can precipitate out during cooling, and it creates a ring/crescent around calcium aluminate.[129] During cooling, MnS can co-precipitate with or dissolve in the CaS phase of calcium aluminate-CaS to form (Ca,Mn)S-oxide inclusions.

The above discussion on the mechanism of inclusion formation and co-precipitation is based on thermodynamic prediction and lattice misfit calculation. More detailed analysis and investigation to validate these proposed mechanisms are required. This validation has not been proceeded with due to limited time and data. Based on the above discussion, the addition of calcium to medium manganese steels in the present study cannot modify AlN inclusions directly. The addition of calcium contributes more to the formation of CAx, CaS, or (Ca,Mn)S-contained inclusions. The co-precipitation of CaS with MnS as (Ca,Mn)S inclusions can promote the formation of (Ca,Mn)S-Nitride, as AlN can nucleate on MnS. However, the co-precipitation of these types of inclusions has not been investigated so far, and there is no report on its effect on the mechanical properties of the steels.

In addition, Figure 6.5(a) and Figure 6.5(b) show the typical morphology of (Ca,Mn)S-Nitride and (Ca,Mn)S-Oxide inclusions, respectively. (Ca,Mn)S-Nitride inclusions are irregular/angular in shape whereas (Ca,Mn)S-Oxide inclusions appear to have a globular shape with (Ca,Mn)S present on the periphery of oxide inclusions. Both morphologies would deform differently during the hot rolling of steel. However, it needs more analysis and investigation of these inclusions' morphology to have a more meaningful discussion.

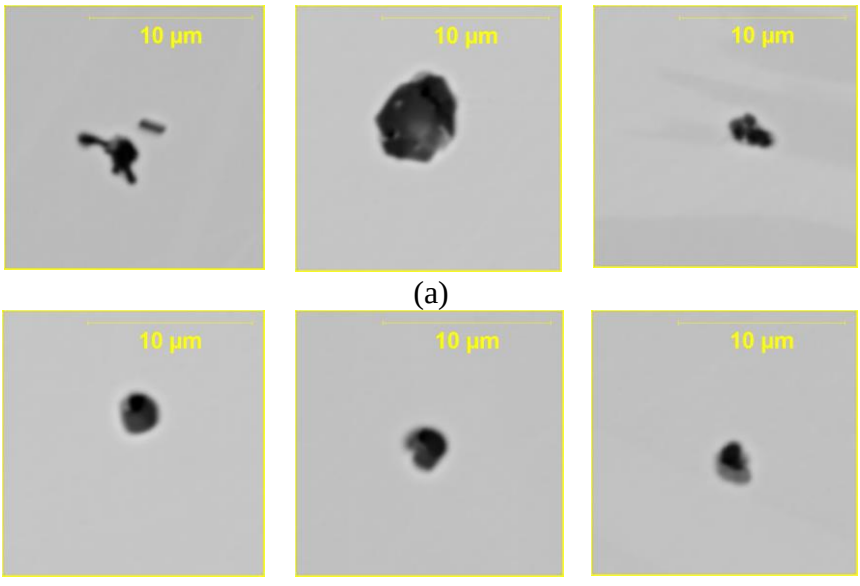

Figure 6. 5 Typical morphology of (a) (Ca,Mn)S-Nitride and (b) (Ca,Mn)S-Oxide inclusions.

6.5 Conclusion

The addition of Ca into the medium Mn steel influences the chemistry of inclusions present in the steel. The observation related to this type of inclusions is listed below.

1. CAS-Other inclusion class consists of (Ca,Mn)S, (Ca,Mn)S-Nitride, and (Ca,Mn)S-Oxide inclusions.
2. After the addition of Ca, (Ca,Mn)S-Oxide inclusions are the primary inclusions in the CAS-Other class. However, the number of (Ca,Mn)S-Nitride inclusions increases with time and injection of N_2 gas.
3. Formation of (Ca,Mn)S-Nitride results from co-precipitation of AlN, MnS, and CaS.

Chapter 7

Concluding Remarks

This thesis focused on understanding the evolution of inclusions during the refining process of medium manganese steels (the present study has Mn = 5%) and high manganese steels (Mn = 20%). Numerous laboratory-scale experiments were performed to investigate the effects of the alloying elements, such as manganese, aluminum, and nitrogen, on the morphology, chemistry, size, and number density of the observed inclusions using two and three-dimensional inclusion analysis techniques. This work proposed the formation mechanism of the inclusions by considering thermodynamics and heterogeneous nucleation.

7.1. Key Findings and Contributions

7.1.1 General Overview

Chapter 1 and 2 presented background and literature review for the current study, with a focus on the inclusion analysis methods and the characteristics of inclusions in the medium manganese steels (3% < Mn < 10%) and high manganese steels (10% < Mn < 30%). Further, the relationship between the characteristics of inclusions and the mechanical properties of steels was presented.

Chapter 3 presented a systematic study on establishing inclusion classification rules for an automated inclusions analysis (SEM equipped with ASPEX system) for medium manganese steels and high manganese steels. The new inclusion classification rules can successfully differentiate the nitride inclusions from the oxide and sulfide inclusions. The established inclusion classification rules were applied to study the effect of alloying elements, such as Mn, Al, and N, on the characteristics of inclusions which were described in Chapters 3, 4, and 5, respectively.

Chapter 3 also contributed to understanding the impact of manganese content on the formation of inclusions in the experimental steels. The investigated manganese contents were 2, 5, and 20%. It was found that a higher manganese content led to the formation of a higher number of inclusions and didn't impact the chemistry of inclusions. The observed inclusions were classified into three major classes, i.e., Al_2O_3, MnS, and AlN. These major classes were further categorized into subclasses which contain their pure phases and the co-precipitates of different phases. To the best of the authors' knowledge, both inclusion classification rules and a comparison of characteristics of inclusions have not been reported previously.

The co-precipitation of AlN and MnS inclusions in the investigated steels was discussed by introducing two co-precipitation scenarios in Chapter 3. Scenario 1 was for heterogeneous nucleation of AlN on MnS inclusions, and Scenario 2 was for AlN inclusions as a nucleation site for MnS.

Chapter 4 contributed to the limited available data on the effect of varied Al content on the formation of inclusions in medium manganese steels. The investigated content of Al was 0.5, 1, 3, and 5%. This chapter reported that increasing Al content led to an increase in the number of inclusions. It also addressed the co-precipitation of inclusions by calculating the precipitation ratio (PR) between AlN and Al_2O_3, Al_2O_3 and MnS, and AlN and MnS inclusions.

As reported in Chapter 2, there is a lack of work studying the effect of N content on the characteristics of inclusions in the medium manganese steels. This was addressed in Chapter 5 by systematically studying the influence of N addition in the melt. Nitrogen was introduced by two different methods, i.e., purging N_2 gas in the furnace chamber and injecting N_2 gas into the steel melt. The N content was varied from low (2 ppm) to high (54 ppm) N content. Samples with different cooling rates and various N contents were compared for the difference in fractions of AlN subclasses. Based on experimental results, Chapter 5 reported the formation mechanism of AlN-containing inclusions. Further, the morphology of AlN-containing inclusions was observed in all the steel samples. It was found that the morphology of AlN inclusions in samples containing more than 50 ppm of N was mostly plate-like.

Chapter 6 explored the possibility of modification of AlN-containing inclusions by the addition of Ca into medium manganese steel. It was found that Ca treatment might not be an effective method for modification of AlN-containing inclusions, as Ca cannot directly react with AlN. Calcium could react with MnS in AlN-MnS inclusions and form (Ca,Mn)S-AlN, as MnS and CaS both can form a (Ca,Mn)S solid solution. The lattice misfit between these inclusions was calculated to study the feasibility of co-precipitation between CaS, MnS, and AlN inclusions. The formation of complex (Cas,Mn)S-AlN inclusions has not been reported in the literature and their influence on the properties of steel is unknown and needs to be investigated.

7.1.2 Specific Findings

The research objectives mentioned in Chapter 1 have been achieved, and the key findings of the present study are listed below.

1. In Chapters 3, 4, and 5, it was found that the investigated steels contain $Al_2O_{3(pure)}$, Al_2O_3-MnS, $AlN_{(pure)}$, AlN-MnS, AlON, AlON-MnS, and MnS inclusions.
2. Results from Chapter 3 demonstrated that the increase of Mn content from 2 to 20% increases the total number of inclusions by 8 times. Manganese content mostly influences the number of AlN and MnS formed in the steel. The increase in the Mn

content directly influences the N solubility in the steel, which is also confirmed by the rise in the N content in the steel composition.

3. Chapter 4 presented that an increase in Al content from 0.5 to 6% also increases the total number of inclusions by 2.5 times, especially AlN inclusions.
4. Results from Chapters 3 and 4 showed that the N content in the steel is approximately 10 ppm, and the critical N content to form stable AlN in the liquid steel is not achieved. So, AlN inclusions are formed as the solidification product or during cooling of the liquid steel.
5. Results from Chapters 3 and 4 demonstrated that AlN and MnS could heterogeneously nucleate on each other, resulting in the formation of AlN-MnS co-precipitates. The co-precipitation could occur according to two scenarios, i.e., 1) heterogeneous nucleation of AlN on MnS inclusions and 2) AlN acting as a nucleation site for MnS. This co-precipitation is possible due to the low lattice mismatch between AlN and MnS inclusions. Chapter 4 also showed that Al_2O_3 inclusions could be the nucleation site for both AlN and MnS inclusions. It was found that for the low N-containing steel, MnS inclusions prefer to nucleate on AlN inclusion rather than Al_2O_3 inclusion.
6. Chapter 5 found that the N content of steel increases faster by injecting N_2 into the steel melt as compared to purging N_2 gas in the furnace chamber. The increase in the N content increases the total number of inclusions from ~13 to ~64 mm^{-2} by purging N_2 gas while the total number of inclusions increases from 21 to 108 mm^{-2} when N_2 gas injection is used. As expected, AlN-containing inclusions had a significant increase.
7. Chapter 5 discussed that when the N content in the steel is low (2-10 ppm), AlN inclusions are solidification products. Then AlN co-precipitates with MnS inclusions and forms AlN-MnS inclusions, which are the dominant inclusion type. As the N content in the steel increased to medium content (23-47ppm), the AlN inclusions could be formed in the liquid steel during cooling of steel from 1873 K. However, when the N content is high (>50 ppm), the primary inclusions change to $AlN_{(pure)}$, as it is stable in the liquid steel at 1873 K.
8. Chapter 5 compared the steel samples cooled at different cooling rates, air-cooled pin samples (20-30 K/sec), and bulk samples which were slow-cooled in the furnace (0.167 K/sec). It was found that AlN-MnS inclusions are always formed in slow-cooled steel regardless of the N content in the steel. This phenomenon was related to the formation temperature of AlN (T_{AlN}) and MnS (T_{MnS}) and the capability of AlN and MnS to nucleate on each other. Thus, the co-precipitation of inclusions happens when the inclusions (AlN and MnS) form during the solidification process. However, AlN inclusions that formed in the liquid steel do not participate in the co-precipitation. It was also observed that N content does not influence the amount of AlN-MnS inclusion since the slow cooling rate provides enough time for the formation of MnS during solidification and nucleation of MnS on AlN inclusion.

9. Chapter 5 described that AlN inclusions exhibit different morphologies, such as plate-like, needle, agglomerate, angular, and irregular. However, it is difficult to correlate the effect of N content in the steel to the morphology of AlN inclusion. Moreover, the three-dimensional observations revealed that the inclusion analysis performed on a cross-section (two-dimension) might not provide the correct morphology of AlN inclusions. For instance, it was observed that plate-like AlN inclusions, which are positioned at different orientations, could appear as angular on a cross-section.
10. In Chapter 6, the calculated misfits between CaS and MnS and between AlN and MnS are less than 10%, whereas the misfits between CaS and AlN, and between CaS and Al_2O_3 are more than 14%. It was found that CaS and AlN cannot co-precipitate; however, CaS could interact with AlN-MnS inclusions resulting in the formation of (Ca,Mn)S-Nitride inclusions.

The medium manganese steels and high manganese steels are bound to have high N content because the presence of Mn increases the solubility of N in the steel. Moreover, due to high Al concentrations in these types of steels, the formation of AlN-contained inclusions cannot be avoided. AlN inclusions are detrimental to the steel performance (e.g., poor hot ductility); therefore, their formation should be controlled by optimizing the Al and Mn content of steel, and by keeping the N content as low as possible during steel refining operations. This understanding is crucial for high manganese steels and medium manganese steels which are a relatively new type of AHSS. As these types of steel are under development, a lot of information is needed to improve their production process. The present study is expected to guide steelmakers to design workable processes.

7.2. Future Works

Besides Mn and Al, Si is another main alloying element for medium manganese steel and high manganese steel. The Si content of steel and N solubility have an inverse relationship. A decrease in Si content can lead to an increase in the formation of nitride inclusions. Therefore, a complete understanding of the effect of the alloying elements on inclusion formation can be achieved by including the effect of Si content.

In Chapter 5, the effect of N content on the morphology of $AlN_{(pure)}$ inclusions was studied. A 3D observation with the application of the electrolytic etched technique was conducted for a few samples. It was found that some plate-like AlN inclusions were oriented at a different angle. This orientation could make plate-like inclusions observed as angular inclusions in the 2D surface. Therefore, a more detailed 3D inclusion analysis is recommended to understand the morphology of AlN inclusions better.

Moreover, the modification of inclusions can be further explored. In the present study, Ca was added before the injection of N_2 gas. However, this addition still cannot give the

optimum inclusion modification result. The sequence can be changed by first injecting N_2 gas until reaching a specific content of N and then continuing with the addition of Ca. In this way, the modification of inclusions is not disturbed by turbulence from the gas injection. Besides Ca addition, rare earth (RE) elements can also be added to modify inclusions. Since RE elements are denser than Ca, they can have a longer residence time in the liquid steel to react or collide with more inclusions.

The classification of inclusions in the present study does not include spinel inclusions. In the actual steelmaking process, there could be other elements as alloying elements or impurities from the refractory lining, such as Mg, promoting the formation of $MgAl_2O_4$ spinel inclusions. It would be worth studying the possibility of co-precipitation of nitride inclusions with spinel inclusions.

References

1 S.E. Kang, J.R. Banerjee, and B. Mintz: *Mater. Sci. Technol.*, 2012, vol. 28, pp. 589–96.

2 B. Steenken, J.L.L. Rezende, and D. Senk: *Mater. Sci. Technol.*, 2017, vol. 33, pp. 567–73.

3 H. Liu, J. Liu, B. Wu, Y. Shen, Y. He, H. Ding, and X. Su: *Mater. Sci. Eng. A*, 2017, vol. 708, pp. 360–74.

4 Y.-N. Wang, J. Yang, R.-Z. Wang, X.-L. Xin, and L.-Y. Xu: *Metall. Mater. Trans. B*, 2016, vol. 47, pp. 1697–1712.

5 G.A. Osinkolu, M. Tacikowski, and A. Kobylanski: *Mater. Sci. Technol.*, 1985, vol. 1, pp. 520–5.

6 A.M. Schulte, S.N. Lekakh, D.C. Van Aken, and V.L. Richards: *Trans. Am. Foundry Soc.*, 2010, vol. 118, pp. 451–64.

7 R. Vaz Penna, L.N. Bartlett, and T. Constance: *Int. J. Met.*, 2019, vol. 13, pp. 286–99.

8 X.L. Xin, J. Yang, Y.N. Wang, R.Z. Wang, W.L. Wang, H.G. Zheng, and H.T. Hu: *Ironmak. Steelmak.*, 2016, vol. 43, pp. 234–42.

9 Z. Yu and C. Liu: *Metall. Mater. Trans. B Process Metall. Mater. Process. Sci.*, 2019, vol. 50, pp. 772–81.

10 Y.N. Wang, J. Yang, X.L. Xin, R.Z. Wang, and L.Y. Xu: *Metall. Mater. Trans. B Process Metall. Mater. Process. Sci.*, 2016, vol. 47, pp. 1378–89.

11 Y.-K. Lee and J. Han: *Mater. Sci. Technol.*, 2015, vol. 31, pp. 843–56.

12 H. Aydin, E. Essadiqi, I.H. Jung, and S. Yue: *Mater. Sci. Eng. A*, 2013, vol. 564, pp. 501–8.

13 B. Hu, H. Luo, F. Yang, and H. Dong: *J. Mater. Sci. Technol.*, 2017, vol. 33, pp. 1457–64.

14 L. Chen, Y. Zhao, and X. Qin: *Acta Metall. Sin. (English Lett.*, 2013, vol. 26, pp. 1–15.

15 M.-K. Paek, J.-M. Jang, K.-H. Do, and J.-J. Pak: *Met. Mater. Int.*, 2013, vol. 19, pp. 1077–81.

16 Biofuels for Steelmaking, https://www.nrcan.gc.ca/energy/efficiency/industry/processes/energy-systems/metallurgical-fuels/5619, (accessed 12 May 2020).

17 E. Pretorius, H. Oltmann, and J. Jones: *EAF Fundamentals*, New York, PA, 2010.

18 Overview of the steelmaking process, https://www.worldsteel.org/en/dam/jcr:177c8e5c-e02a-4e08-9dc6-cce7372b41c2/Overview%2520of%2520the%2520Steelmaking%2520Process_poster.pdf, (accessed 3 February 2021).

19 L. Holappa: in *Treatise on Process Metallurgy - Industrial Process*, S. Seetharaman, A. Mclean, R. Guthrie, and S. Sridhar, eds., Elsevier, United Kingdom, 2014, pp. 301–45.

20 L.F. Zhang and B.G. Thomas: in *XXIV National Steelmaking Symposium*, Morelia, 2003, pp. 26–8.

21 E.T. Turkdogan: *Fundamentals of Steelmaking*, The Institute of Materials, London, 1996.

22 A. Ghosh: *Secondary Steelmaking*, CRC Press, United States of America, 2001.

23 M.S. Millman: *Ironmak. Steelmak.*, 1999, vol. 26, pp. 169–75.

24 T. Kato: *Trans. Iron Steel Inst. Japan*, 1986, vol. 26, pp. 851–7.

25 B. Deo and R. Boom: *Fundamentals of Steelmaking Metallurgy*, Prentice Hall International, United Kingdom, 1993.

26 M.G. Dumitru, A. Ioana, N. Constantin, F. Ciobanu, and M. Pollifroni: *IOP Conf. Ser. Mater. Sci. Eng.*, DOI:10.1088/1757-899X/294/1/012018.

27 J. Pérez: McMaster University, 2012.

28 I.O. Otunniyi, Z. V. Theko, B.L.E. Mokoena, and B. Maramba: *IOP Conf. Ser. Mater. Sci. Eng.*, 2019, vol. 655, pp. 1–10.

29 L. Holappa and S. Louhenkilpi: in *Proceedings of INFACON XIII - 13th International Ferroalloys Congress: Efficient Technologies in Ferroalloy Industry*, Almaty, Kazakhstan, 2013, pp. 1083–90.

30 P. Alvarez, F. Muñoz, D. Celentano, A. Artigas, F.M. Castro Cerda, J.P. Ponthot, and A. Monsalve: *Metals (Basel).*, 2020, vol. 10, pp. 1–13.

31 S. Lee, K. Lee, and B.C. De Cooman: *Metall. Mater. Trans. A Phys. Metall. Mater. Sci.*, 2015, vol. 46, pp. 2356–63.

32 M. Sabzi and M. Farzam: *Mater. Res. Express*, DOI:10.1088/2053-1591/ab3ee3.

33 a. a. Alekseenko, E. V. Baibekova, S.N. Kuznetsov, B.Y. Baldaev, a. V. Ziborov, D. a. Ponomarenko, and a. G. Ponomarenko: *Russ. Metall.*, 2007, vol. 2007, pp. 634–7.

34 F. Tehovnik, J. Burja, B. Arh, and M. Knap: *Metalurgija*, 2015, vol. 54, pp. 371–4.

35 L.F. Zhang and S. Taniguchi: *Int. Mater. Rev.*, 2000, vol. 45, pp. 59–82.

36 B.H. Reis, W.V. Bielefeldt, and A.C.F. Vilela: *ISIJ Int.*, 2014, vol. 54, pp. 1584–91.

37 M. Wang, Y. Bao, H. Cui, H. Wu, and W. Wu: *ISIJ Int.*, 2010, vol. 50, pp. 1606–11.

38 D.A. Jerebtsov and G.G. Mikhailov: *Ceram. Int.*, 2001, vol. 27, pp. 25–8.

39 G.J.W. Kor and P.C. Glaws: in *The Making, Shaping and Treating of Steel*, R.J. Fruehan, ed., The AISE Steel Foundation, Pittsburgh, PA, 1998, pp. 661–713.

40 G. Chen and S. He: *Vacuum*, 2018, vol. 153, pp. 132–8.

41 W. Xiao, M. Wang, and Y. Bao: *Metals (Basel).*, DOI:10.3390/met9080812.

42 Z. Zulhan and C. Schrade: *SEAISI Conf. Exhib.*, 2014, pp. 26–9.

43 Z. Zulhan and C. Schrade: in *SEAISI Conference and Exhibition*, Kuala Lumpur, 2014.

44 F.N.H. Schrama, E.M. Beunder, B. Van den Berg, Y. Yang, and R. Boom: *Ironmak. Steelmak.*, 2017, vol. 44, pp. 333–43.

45 S. Keeler and M. Kimchi, eds.: *Advance High-Strength Steels Application Guidelines Version 5.0*, 2014.

46 E. Billur: *Hot Stamping of Ultra High-Strength Steels*, 2019.

47 E. Billur and T. Altan: *Stamp. J.*, 2013, vol. Nov/Dec, pp. 16–7.

48 D. Bhattacharya: *Tecnol. em Metal. Mater. e Mineração*, 2014, vol. 11, pp. 371–83.

49 M. Chiaberge, ed.: *NEW TRENDS AND DEVELOPMENTS IN AUTOMOTIVE*, InTech, Rijeka, Croatia, 2011.

50 J. Zhao, Y. Xi, W. Shi, and L. Li: *J. Iron Steel Res. Int.*, 2012, vol. 19, pp. 57–62.

51 W. Bleck: *Steel Res. Int.*, 2018, vol. 89, p. 1.

52 A. Haldar, S. Suwas, and D. Bhattacharjee, eds.: *Proceedings of the International Conference on Microstructure and Texture in Steels and Other Materials*, vol. 1, Springer, Jamshedpur, 2015.

53 B.C. De Cooman, L. Chen, H.S. Kim, Y. Estrin, S.K. Kim, and H. Voswinckel: in *Microstructure and Texture in Steels*, 2009, pp. 165–83.

54 D.Z. Li, Y.H. Wei, B.S. Xu, L.F. Hou, and P.D. Han: *Ironmak. Steelmak.*, 2011, vol. 38, pp. 540–5.

55 O. Grässel, L. Krüger, G. Frommeyer, and L.W. Meyer: *Int. J. Plast.*, 2000, vol. 16, pp. 1391–409.

56 R.T. Van Tol, L. Zhao, L. Bracke, P. Kömmelt, and J. Sietsma: *Metall. Mater. Trans. A Phys. Metall. Mater. Sci.*, 2013, vol. 44, pp. 4654–60.

57 L. Chen, S. Lee, and B.C. De Cooman: *ISIJ Int.*, 2012, vol. 52, pp. 1670–7.

58 O. Bouaziz, S. Allain, C.P. Scott, P. Cugy, and D. Barbier: *Curr. Opin. Solid State Mater. Sci.*, 2011, vol. 15, pp. 141–68.

59 L. a Dobrzański and W. Borek: *J. Achiev. Mater. Manuf. Eng.*, 2012, vol. 55, pp. 230–8.

60 C. Busch, A. Hatscher, M. Otto, S. Huinink, M. Vucetic, C. Bonk, A. Bouguecha, and B.A. Behrens: *Procedia Eng.*, 2014, vol. 81, pp. 939–44.

61 S. Allain, J.P. Chateau, and O. Bouaziz: *Mater. Sci. Eng. A*, 2004, vol. 387–389, pp. 143–7.

62 Y.N. Dastur and W.C. Leslie: *Metall. Trans. A*, 1981, vol. 12, pp. 749–59.

63 E. Bayraktar, F.A. Khalid, and C. Levaillant: *J. Mater. Process. Technol.*, 2004, vol. 147, pp. 145–54.

64 B.X. Huang, X.D. Wang, Y.H. Rong, L. Wang, and L. Jin: *Mater. Sci. Eng. A*, 2006, vol. 438–440, pp. 306–11.

65 K. Schwerdtfeger and K.H. Spitzer: *ISIJ Int.*, 2009, vol. 49, pp. 512–20.

66 H. Dong, X. Sun, W. Cao, Z. Liu, M. Wang, and Y. Weng: in *Advanced Steels*, Y. Weng, H. Dong, and Y. Gan, eds., Metallurgical Industry Press, 2011, pp. 35–57.

67 B. Sun, F. Fazeli, C. Scott, N. Brodusch, R. Gauvin, and S. Yue: *Acta Mater.*, 2018, vol. 148, pp. 249–62.

68 Z.H. Cai, B. Cai, H. Ding, Y. Chen, and R.D.K. Misra: *Mater. Sci. Eng. A*, 2016, vol. 676, pp. 263–70.

69 P.A. Thornton: *J. Mater. Sci.*, 1971, vol. 6, pp. 347–56.

70 J. Maciejewski: *J. Fail. Anal. Prev.*, 2015, vol. 15, pp. 169–78.

71 N. Ånmark, A. Karasev, and P. Jönsson: *Materials (Basel).*, 2015, vol. 8, pp. 751–83.

72 Y. Tomita: *Mater. Charact.*, 1995, vol. 34, pp. 121–8.

73 G.M. Faulring and S. Ramalingam: *Metall. Trans. A*, 1979, vol. 10, pp. 1781–8.

74 M. Wang, W. Xiao, P. Gan, C. Gu, and Y.P. Bao: *Metals (Basel).*, 2020, vol. 10, pp. 1–15.

75 G.D. Funnell and R.J. Davies: *Met. Technol.*, 1978, vol. 5, pp. 150–3.

76 M. Lückl, T. Wojcik, E. Povoden-Karadeniz, S. Zamberger, and E. Kozeschnik: *Steel Res. Int.*, 2018, vol. 89, pp. 1–9.

77 S.E. Kang, A. Tuling, J.R. Banerjee, W.D. Gunawardana, and B. Mintz: *Mater. Sci. Technol.*, 2011, vol. 27, pp. 95–100.

78 R. Kiessling: *Non-Metallic Inclusions in Steel: The Origin and Behaviour of Inclusions and Their Influence on the Properties of Steels, Part 3*, Iron and Steel Institute, London, 1968.

79 a Ray, S.. Paul, and S. Jha: *J. Mater. Eng. Perform.*, 1995, vol. 4, pp. 679–88.

80 C. Zhuang, J. Liu, Z. Mi, H. Jiang, D. Tang, and G. Wang: *Steel Res. Int.*, 2014, vol. 85, pp. 1432–9.

81 H. Liu, J. Liu, S. Michelic, F. Wei, C. Zhuang, Z. Han, and S. Li: *Ironmak. Steelmak.*, 2016, vol. 43, pp. 171–9.

82 H. Liu, J. Liu, S.K. Michelic, S. Shen, X. Su, B. Wu, and H. Ding: *Steel Res. Int.*, 2016, vol. 87, pp. 1723–32.

83 G. Gigacher, W. Krieger, P.R. Scheller, and C. Thomser: *Steel Res. Int.*, 2005, vol. 76, pp. 644–9.

84 J.H. Park, D.J. Kim, and D.J. Min: *Metall. Mater. Trans. A*, 2012, vol. 43, pp. 2316–24.

85 L. Kong, Z. Deng, and M. Zhu: *ISIJ Int.*, 2017, vol. 57, pp. 1537–45.

86 S.K. Mandal: in *Steel Metallurgy: Properties, Specifications and Applications*, McGraw-Hill Education, New Delhi, 2015.

87 A.L.V. Da Costa E Silva: *J. Mater. Res. Technol.*, 2018, vol. 7, pp. 283–99.

88 L.W. Helle and W.F. Smith: *J. South African Inst. Min. Metall.*, 1984, vol. 84, pp. 94–102.

89 C. Chen and K. Lin: *China Steel Tech. Rep.*, 2011, vol. 24, pp. 7–13.

90 D.C. Hilty and W. Crafts: *J. Met.*, 1950, vol. 188, pp. 414–24.

91 JSPS: *Steelmaking Data Sourcebook*, Revised., Gordon and Breach Science Publications, 1988.

92 S. He, G. Chen, Y. Guo, B. Shen, and Q. Wang: *Metall. Mater. Trans. B*, 2015, vol. 46, pp. 585–94.

93 Z. Deng and M. Zhu: *ISIJ Int.*, 2014, vol. 54, pp. 1498–506.

94 X.-M. Yang, C.-B. Shi, M. Zhang, G.-M. Chai, and F. Wang: *Metall. Mater. Trans. B*, 2011, vol. 42, pp. 1150–80.

95 H. Itoh, M. Hino, and S. Ban-Ya: *Tetsu-to-Hagane*, 1997, vol. 83, pp. 773–8.

96 J. Do Seo, S.H. Kim, and K.R. Lee: *Steel Res.*, 1998, vol. 69, pp. 49–53.

97 M.K. Paek, K.H. Do, Y.B. Kang, I.H. Jung, and J.J. Pak: *Metall. Mater. Trans. B Process Metall. Mater. Process. Sci.*, 2016, vol. 47, pp. 2837–47.

98 D. Senk, K. Christmann, S. Geimer, and D. Rzehak: *Steel Res. Int.*, 2016, vol. 87, pp. 107–11.

99 J.-M. Jang, M.-K. Paek, and J.-J. Pak: *ISIJ Int.*, 2017, vol. 57, pp. 1821–30.

100 M.-K. Paek, J.-M. Jang, H.-J. Kang, and J.-J. Pak: *ISIJ Int.*, 2013, vol. 53, pp. 535–7.

101 G.K. Sigworth and Elliot J. F.: *Met. Sci.*, 1974, vol. 8, pp. 298–310.

102 M. Paek, J. Jang, M. Jiang, and J. Pak: *ISIJ Int.*, 2013, vol. 53, pp. 973–8.

103 C. Bin Shi, X.C. Chen, and H.J. Guo: *Int. J. Miner. Metall. Mater.*, 2012, vol. 19, pp. 295–302.

104 R. Singh: in *Applied Welding Engineering : Processes, Codes, and Standards*, 2nd edn., Butterworth-Heinemann, Amsterdam, 2016, pp. 7–12.

105 Z. Szklarska- śmialowska and E. Lunarska: *Mater. Corros.*, 1981, vol. 32, pp. 478–85.

106 G.H. Xiao, H. Dong, M.Q. Wang, and W.J. Hui: *J. Iron Steel Res. Int.*, 2011, vol. 18, pp. 58–64.

107 Y. Tanaka, F. Pahlevani, S.C. Moon, R. Dippenaar, and V. Sahajwalla: *Sci. Rep.*, 2019, vol. 9, pp. 1–12.

108 Y. Qi, J. Li, C. Shi, H. Wang, and D. Zheng: *Metall. Res. Technol.*, 2019, vol. 116, pp. 1–12.

109 R. Vaz Penna, L.N. Bartlett, and R. O'Malley: *Int. J. Met.*, 2020, vol. 14, pp. 342–55.

110 B.L. Bramfitt: *Metall. Trans.*, 1970, vol. 1, pp. 1987–95.

111 D. Turnbull and B. Vonnegut: *Ind. Eng. Chem.*, 1952, vol. 44, pp. 1292–8.

112 G.L. Sun, B. Song, L.Z. Yang, S.F. Tao, and Y. Yang: *Int. J. Miner. Metall. Mater.*, 2014, vol. 21, pp. 654–9.

113 H. Ohta and H. Suito: *ISIJ Int.*, 2006, vol. 46, pp. 480–9.

114 A. Tuling and B. Mintz: *Mater. Sci. Technol.*, 2016, vol. 32, pp. 568–75.

115 F. Wang and Z. Fan: *Metall. Mater. Trans. A Phys. Metall. Mater. Sci.*, 2019, vol. 50, pp. 2519–26.

116 R. Dekkers: in *Industrial Minerals: Resources, Characteristics, and Applications*, P. Degryse and J. Elsen, eds., Leuven University Press, 2003, pp. 109–20.

117 Y. Tabatabaei, K.S. Coley, G.A. Irons, and S. Sun: *Metall. Mater. Trans. B Process Metall. Mater. Process. Sci.*, 2018, vol. 49, pp. 2022–37.

118 L.E.K. Holappa and H.Y.S. Ylonen: in *Fifth International Iron and Steel Congress*, 1986, pp. 277–83.

119 K. Larsen and R.J. Fruehan: *Trans. ISS*, 1990, vol. 17, pp. 45–52.

120 N. Verma, P.C. Pistorius, R.J. Fruehan, M. Potter, M. Lind, and S.R. Story: *Metall. Mater. Trans. B*, 2011, vol. 42, pp. 720–9.

121 N. Verma, P.C. Pistorius, R.J. Fruehan, M. Potter, M. Lind, and S. Story: *Metall. Mater. Trans. B Process Metall. Mater. Process. Sci.*, 2011, vol. 42, pp. 711–9.

122 Y. Higuchi, M. Numata, S. Fukagawa, and K. Shinme: *ISIJ Int.*, 1996, vol. 36, pp. S151–4.

123 D. Lu: McMaster University, 1992.

124 Y. Ito, M. Suda, Y. Kato, H. Nakato, and K. Sorimachi: *ISIJ Int.*, 1996, vol. 36, pp. S148–50.

125 Z.. Han, L. Liu, M. Lind, and L. Holappa: *Acta Metall. Sin. (English Lett.*, 2006, vol. 19, pp. 1–8.

126 D.Z. Lu and G.A. Irons: *Ironmak. Steelmak.*, 1994, vol. 21, pp. 362–71.

127 J.M. a. Geldenhuis and P.C. Pistorius: *Ironmak. Steelmak.*, 2000, vol. 27, pp. 442–9.

128 S.K. Choudhary and A. Ghosh: *ISIJ Int.*, 2008, vol. 48, pp. 1552–9.

129 D. Zhao, H. Li, C. Bao, and J. Yang: *ISIJ Int.*, 2015, vol. 55, pp. 2115–24.

130 M. Jiang, X.H. Wang, and W.J. Wang: *Steel Res. Int.*, 2010, vol. 81, pp. 759–65.

131 M. Jiang, X. Wang, B. Chen, and W. Wang: *ISIJ Int.*, 2010, vol. 50, pp. 95–104.

132 B.S. Van Gosen, P.L. Verplanck, R.R. Seal II, K.R. Long, and J. Gambogi: in *Critical*

Mineral Resources of the United States - Economic and Environmental Geology andProspects for Future Supply: U.S. Geological SUrvey Professional Paper 1802, K.J. Schulz, D.J. H., R.R. Seal II, and D.C. Bradley, eds., USGS, Reston, Virginia, 2017, pp. 1–31.

133 P.E. Waudby: *Int. Mater. Rev.*, 1978, vol. 23, pp. 74–98.

134 M. Opiela: *J. Achiev. Mater. Manuf. Eng.*, 2011, vol. 47, pp. 149–56.

135 M. Opiela and A. Grajcar: *Arch. Foundry Eng.*, 2012, vol. 12, pp. 129–34.

136 M.M. Song, B. Song, W.B. Xin, G.L. Sun, G.Y. Song, and C.L. Hu: *Ironmak. Steelmak.*, 2015, vol. 42, pp. 594–9.

137 *ASM Handbook Volume 1 - Properties and Selection: Irons Steels and High Performance Alloys*, 10th edn., ASM International, 1993.

138 A. Grajcar, U. Galisz, and L. Bulkowski: *Arch. Mater. Sci. Eng.*, 2011, vol. 50, pp. 21–30.

139 A. Grajcar, U. Galisz, L. Bulkowski, M. Opiela, and P. Skrzypczyk: *J. Achiev. Mater. Manuf. Eng.*, 2012, vol. 55, pp. 245–55.

140 A. Walters and P. Lusty: *Br. Geol. Surv.*, 2011, p. 54.

141 N.E. Luiz and Á.R. Machado: *Proc. Inst. Mech. Eng. Part B J. Eng. Manuf.*, 2008, vol. 222, pp. 347–60.

142 R.D. Brown: *U.S. Geol. Surv. Miner. Yearb.*, 2000, pp. 1–8.

143 R. Kiessling and N. Lange: *Non-Metallic Inclusion in Steel: Inclusions Belonging to the Systems MgO-SiO2-Al2O3, CaO-SiO2-Al2O3 and Related Oxide Systems, Sulphide Inclusion, Part 2*, Iron and Steel Institute, London, 1966.

144 R.H. Aborn: *The Role of Selenium and Tellurium in Ferrous Metals*, Institutet fur Metallforskning, Stockholm, 1969.

145 V. Thapliyal, A. Kumar, D. Robertson, and J. Smith: *ISIJ Int.*, 2015, vol. 55, pp. 190–9.

146 T. Zhang, Y. Min, C. Liu, and M. Jiang: *ISIJ Int.*, 2015, vol. 55, pp. 1541–8.

147 P. Kaushik, H. Pielet, and H. Yin: *Ironmak. Steelmak.*, 2009, vol. 36, pp. 561–71.

148 P. Kaushik, H. Pielet, and H. Yin: *Ironmak. Steelmak.*, 2009, vol. 6, pp. 82–99.

149 L.F. Zhang: *J. Iron Steel Res. Int.*, 2006, vol. 13, pp. 1–8.

150 M. Harris, O. Adaba, S. Lekakh, R. O'Malley, and L. Von Richards: *AISTech - Iron Steel Technol. Conf. Proc.*, 2015, vol. 3, pp. 3315–25.

151 R. Dekkers, N. Jokanovic, A. Rombout, B. Blanpain, and P. Wollants: *Steel Res. Int.*, 2005, vol. 76, pp. 475–80.

152 H.F. Jacobi: *Steel Res. Int.*, 2005, vol. 76, pp. 595–602.

153 R. Inoue, S. Ueda, T. Ariyama, and H. Suito: *ISIJ Int.*, 2011, vol. 51, pp. 2050–5.

154 J.L. Weeks, M.A. Blount, A. Beasley, R. Zoraghi, M.K. Thomas, K.R. Sekhar, J.D. Corbin, and S.H. Francis: in *Phosphodiesterase Methods and Protocols. Methods In Molecular Biology™*, C. Lugnier, ed., vol. 307, Humana Press, 2005, pp. 239–62.

155 D. Janis, R. Inoue, A. Karasev, and P.G. Jönsson: *Adv. Mater. Sci. Eng.*, 2014, vol. 2014, pp. 1–7.

156 D. Janis, A. Karasev, and P.G. Jönsson: *ISIJ Int.*, 2015, vol. 55, pp. 2173–81.

157 M.M. Pande, M. Guo, R. Dumarey, S. Devisscher, and B. Blanpain: *ISIJ Int.*, 2011, vol. 51, pp. 1778–87.

158 H. Falk and P. Wintjens: *Spectrochim. Acta - Part B At. Spectrosc.*, 1998, vol. 53, pp. 49–62.

159 K. Mizukami, M. Sugiyama, W. Ohashi, K. Mizuno, and M. Tsuji: *Nippon Steel Tech. Rep.*, 2011, pp. 63–71.

160 H. Jacobi and K. Wünnenberg: *Ironmak. Steelmak.*, 2003, vol. 30, pp. 130–41.

161 B.G. Bartosiaki, J.A.M. Pereira, W.V. Bielefeldt, and A.C.F. Vilela: *J. Mater. Res. Technol.*, 2015, vol. 4, pp. 235–40.

162 R. Dekkers, B. Blanpain, P. Wollants, F. Haers, B. Grommers, and C. Vercruyssen: in *ISSTech 2003, Indianapolis, Indiana, USA, 27-30 April 2003*, 2003, pp. 197–209.

163 F. Schamber: *ASPEX Corp.*, 2011, pp. 1–7.

164 H.P. Lentz, M.S. Potter, and G.S. Casuccio: *AISTech - Iron Steel Technol. Conf. Proc.*, 2017, vol. 3, pp. 2803–15.

165 S. Abraham, J. Raines, and R. Bodnar: *AISTech - Iron Steel Technol. Conf. Proc.*, 2013, vol. 1, pp. 1069–84.

166 M. Nuspl, W. Wegscheider, J. Angeli, W. Posch, and M. Mayr: *Anal. Bioanal. Chem.*, 2004, vol. 379, pp. 640–5.

167 S.R. Story, T.J. Piccone, R.J. Fruehan, and M. Potter: *Iron Steel Technol.*, 2004, vol. 1, pp. 163–9.

168 V. Singh, S. Lekakh, E. Martinez, and K. Peaslee: in *MS&T 2009 Proceedings*, Columbus, Ohio, 2009, pp. 1019–30.

169 S. Yang, Q. Wang, L.F. Zhang, J. Li, and K. Peaslee: *Metall. Mater. Trans. B*, 2012, vol. 43, pp. 731–50.

170 L. Kong, Z. Deng, and M. Zhu: *Metall. Mater. Trans. B Process Metall. Mater. Process. Sci.*, 2018, vol. 49, pp. 1444–52.

171 M. Alba, M. Nabeel, and N. Dogan: *Ironmak. Steelmak.*, 2020, pp. 1–8.

172 S. Abraham, R. Bodnar, and J. Raines: .

173 W.V. Bielefeldt and A.C.F. Vilela: *Rev. Matéria*, 2010, vol. 15, pp. 275–82.

174 L. Holappa and O. Wijk: in *Treatise on Process Metallurgy - Industrial Process*, United Kingdom, 2014, pp. 347–72.

175 R. Piao, H.G. Lee, and Y.B. Kang: *ISIJ Int.*, 2013, vol. 53, pp. 2132–41.

176 G. Sun and S. Tao: *Metall. Mater. Trans. B Process Metall. Mater. Process. Sci.*, 2018, vol. 49, pp. 519–23.

177 K. Realo, A. Maaroos, A. Haav, and I. Jaek: *J. Cryst. Growth*, 1982, vol. 56, pp. 639–41.

178 M. Zhang and P.M. Kelly: *Acta Mater.*, 2005, vol. 53, pp. 1073–84.